2017

Kinetic-Control of Block Copolymer Micelles for Tunable Nanomaterials Towards Energy Devices

Hasala Nadeesini Lokupitiya
University of South Carolina

KINETIC-CONTROL OF BLOCK COPOLYMER MICELLES FOR TUNABLE NANOMATERIALS TOWARDS ENERGY DEVICES

by

Hasala Nadeesini Lokupitiya

Bachelor of Science
University of Colombo, 2011

Submitted in Partial Fulfillment of the Requirements

For the Degree of Doctor of Philosophy in

Chemistry

College of Arts and Sciences

University of South Carolina

2017

Accepted by:

Morgan Stefik, Major Professor

Chuanbing Tang, Committee Member

Andrew B. Greytak, Committee Member

Kevin Huang, Committee Member

Cheryl L. Addy, Vice Provost and Dean of the Graduate School

DEDICATION

To my mother,

for her strong soul, which gave me strength to survive in the hardest situations in my life,

To my father,

who protects me and supports me throughout my life journey

To my loving husband Mitra,

for his unconditional love and caring, immense support and encouragements, without you none of my accomplishments would have been possible

To our precious loving son Nyle,

who makes our life unimaginably happy and content

To Cooper,

our loving collie who sits next to me every day when I study

ACKNOWLEDGEMENTS

I want to thank my loving husband for his immense support, encouragements and love. I thank my mother, father, family members and my friends for their love and support. Without each of you, I wouldn't have achieved any of my accomplishments in my life. I thank my advisor, Dr. Morgan Stefik, for his guidance and funding support that made this work possible. I thank my graduate committee members Dr. Chuanbing Tang, Dr. Andrew B. Greytak, Dr. Xiao-Dong Zhou and Dr. Kevin Huang for providing me advice, encouragement, and valuable suggestions on my research during this journey. I want to thank my collaborators, Dr. Dina Fattakhova-Rohlfing and Dr. Kristina Peters at Ludwig-Maximilians-Universität München and Dr. Stefan Guldin and Barry Reid from University College London for their nice collaborations. It was great pleasure to work with them.

I also want to thank Dr. Brian Benicewicz for his support during my PhD and for his great teaching style which I learnt basics of polymer chemistry. I truly thank and admire Dr. John Lavigne for giving me the opportunity to work in his lab as a volunteer researcher as well as a Copenhaver Scholar before started my Ph.D. at USC.

I am sincerely grateful for the loving and caring people I met during the time I spent at USC. Among them, I would like to thank Jennifer Markel, Dr. Bryson, Dr. Caryn Outten, Dr. Linda Shimizu, Julia Pribyl, Sanz Hosseinzade, Swanandi Pote, Sam Burgess and Nanette Goodwin.

Also, I thank Dr. Randima Galhenage, Anushika Jayasinghe and Muditha Dias for being great friends who I can count on at any time. Also, I would like to thank Stefik group members who helped me during my Ph.D. journey.

ABSTRACT

Nano-scale inorganic porous materials are crucial for numerous applications ranging from electronics to energy conversion. The ability to control the morphology and the key architectural parameters of nanomaterials largely determines the transport characteristics and performance of such devices. But, there is very little understanding and development to tune these key architectural parameters such as inorganic wall-thickness and pore diameter. Even though there are numerous examples available on the fabrication of porous nanomaterials via block copolymer co-assembly, there is limited understanding on independent control over key architectural parameters. Because of that the major focus of this thesis is to explore and develop tunable nanomaterials with block copolymer micelles that could use to fabricate nano-optimize energy storage devices with high energy and fast rate capabilities.

Towards this end, tunability of the key architectural parameters was studied and processing guidelines and solution conditions that enable nanostructures with tunable wall-thickness and pore diameters are presented. First, a new block copolymer poly (ethylene oxide-*b*-hexyl acrylate) (PEO-*b*-PHA) structure directing agent (SDA) was synthesized and used to demonstrate the tunability of the inorganic wall-thickness. Specifically, the use of a polymer with a high Flory-Huggins effective interaction parameter, χ, and appropriate solution conditions lead to the kinetic entrapment of micelles to produce persistent micelles which were used as templates to fabricate tunable isomorphic architectures. The use of

different inorganic loadings with persistent micelles resulted in different wall-thicknesses with constant pore size. The processing guidelines for persistent micellar templating (PMT) were elaborated using mesoporous Nb_2O_5 that was thermally stable at 600 ^oC giving access to crystalline materials. Overall, this method provides a simple and a predictable path to produce porous nanomaterials with tunable wall thickness.

Second, these kinetically entrapped block copolymer micelles resulted from a single block copolymer were re-arranged into different micelle sizes to achieve a range of pore dimeters. This target is particularly challenging since the rate of single-chain exchange and micelle fusion/fission reactions are hindered by the large thermodynamic barrier for rearrangement in these kinetically trapped micelle systems. The rate of the chain exchange reactions in block copolymer micelles will increase due to the production of solution-air interface as reported in literature. Here, we used ultrasonic cavitation for rapid interface production that accelerates micelle growth by an order of magnitude over agitation via vortexing. This extremely simple but powerful modification can be used as an unique handle to tune the pore diameter of nanomaterials by achieve a range of micelle sizes from a single block copolymer.

Third, the PMT derived macroporous isomorphic architectures of Nb_2O_5 were used to show the potential application in understanding the operative mechanism of energy storage at different length scale. This sort of model systems could use to systematically investigate the optimal length scale of ion and electron diffusion to produce nano-optimize porous electrode systems. In this study *T*-Nb_2O_5 was selected as the electrode material due to its well-known pseudocapacitive behavior which has ability to combine both high energy densities and high-power densities into one materials. The overall goal of this thesis is to

contribute towards the assembling the nano-porous electrodes into most effective architecture to achieve next generation high energy and power density devices. Therefore, this work demonstrated that the careful tuning of the block copolymer micelles in solution paves a simple and versatile path to obtain tunable nanomaterials which could be highly useful in nanotechnologies such as advanced energy conversion and storage devices.

Table of Contents

LIST OF TABLES

LIST OF FIGURES

List of Symbols

χ	Flory-Huggins effective interaction parameter
T_g	Glass transition temperature
N	Solvophobic block length
$Đ$	Molar mass dispersity
R_c	Block copolymer micelles have the core radius

List of Abbreviations

AICE ..... Agitation-induced Chain Exchange

ATRP ..... Atom Transfer Radical Polymerization

BCC..... Body Centered Cubic

BCP ..... Block Copolymers

DLS ..... Dynamic Light Scattering

DMF ..... *N*,*N*-Dimethylformamide

EES ..... Electrochemical energy storage

EP ..... Ellipsometric Porosimetry

FE-SEM ..... Field Emission Scanning Electron Microscope

FWHM ..... Full Width Half Max

GISAXS ..... Grazing Incidence Small Angle X-ray Scattering

GIWAXS..... Grazing Incidence Wide Angle X-ray Scattering

GPC..... Gel Permeation Chromatography

LIBs..... Lithium-ion batteries

MFT ..... Mean Field Theory

ODT ..... Order to Disorder Transition

PHA..... Poly(hexyl acrylate)

PMT ..... Persistent Micelle Templates

SAXS ..... Small Angle X-ray Scattering

SCs ..... Supercapacitors

SDA..... Structure Directing Agent

TEOS..... Tetraethyl Orthosilicate

THF ..... Tetrahydrofuran

WAXS..... Wide Angle X-ray Scattering

CHAPTER 1

OBJECTIVES AND INTRODUCTION

1.1 Research Objectives

Currently the major source of the world's energy production (~37 %) is relied on fossil fuel which is a rapidly draining source from the earth's crust. Apart from its limited accessibility, the usage of fossil fuels causes climate change forcing humanity to find alternative energy sources. The energy from renewable sources, such as solar and wind power has gained much attention but, introduced a major problem: how do we store the harvested energy until it is to be used? Electrochemical energy storage (EES) devices such as lithium-ion batteries (LIBs) and supercapacitors (SCs) are the key way to store the harvested energy. At the same time, they play a tremendous role in consumer electronics and electrically driven transportation, such as hybrid and plug in vehicles. There is a lot of ongoing research and discussion to improve the energy and the power densities of LIBs and SCs, for use of them efficiently in the above mentioned demands.[1-7] SCs inherent high power densities, much faster response time and longer life cycle than batteries, but have limited application due to lower energy densities. On the other hand, LIBs have high energy densities, but suffer from low power densities, taking hours to charge or discharge a device. A novel type of electrochemical energy storing mechanism known as pseudocapacitance possessed by transition metal oxides at nanometer scale, has gained more attraction in the EES field due to its ability to combine both high energy and high power densities into one material.

Assembling the electrodes into the most effective architecture determines the overall performance of a device. It was shown that assembling pseudocapacitive materials into nano-porous electrodes enhances the pseudocapacitive behavior due to the short paths for ionic and electronic diffusion inside the solid electrode.[8,9] Nano-structuring of inorganic

materials can be achieved with the use of block copolymers as structure directing agent (SDA) coupled with evaporation induced co-assembly. Careful selection and fabrication of block copolymers enable the formation of tunable nanomaterials that could enhance the performance of both energy storage and conversion. In this thesis, the major focus is to independently control the key architectural parameters (wall thickness and pore diameter) of the nano-porous materials derived from block copolymer co-assembly. Therefore, tunable isomorphic architectures of Nb_2O_5 were fabricated which a well-known pseudocapacitive material. These architectures were used as model systems to study the charge storage mechanism with the hope of fabrication of next generation nano-optimize devices.

This thesis is composed with three main sections where (1) synthesis and characterization of a novel block copolymer, poly(ethylene oxide-*b*-hexyl acrylate) PEO-*b*-PHA for the first time in the literature, (2) tunability of key architectural parameters (wall thickness and pore diameter) through persistent micelle templating (PMT) and ultrasonic cavitation and (3) model studies to understand the charge storage mechanism of Nb_2O_5 at different length scales as a demonstration of the capability of PMT towards nano-optimize energy storage devices.

1.2 PEO-*b*-PHA as a Structure Directing Agent (SDA)

Structure directing agents (SDA) are amphiphilic molecules having a hydrophilic portion that selectively interacts with hydrophilic inorganic species via electrostatic or hydrogen bonding and hydrophobic portion that phase separates with nanoscale periodicity. These two entities are covalently bound together giving the ability to micro-phase separation instead macro-phase separation. Hence, the self-assembling properties of

block copolymers supply a solid platform for structuring materials in the nanometer scale as shown in Figure 1.1.[10] In this work poly(ethylene oxide) block was selected as the hydrophilic block and poly(hexyl acrylate) was selected as the hydrophobic block which are having significant solubility gap that could lead to achieve high Flory-Huggins effective interaction parameter in the block copolymer that enables modulation of the reorganization kinetics based upon the presented solution conditions. During this work the Flory-Huggins effective interaction parameter of PEO-*b*-PHA was estimated as 0.34 at 30^{o}C which is a quite high value with compared to other SDA used for co-assembly. Furthermore, PEO and the PHA blocks have low glass transition temperatures (T_g) which support the structure formation at room temperature.

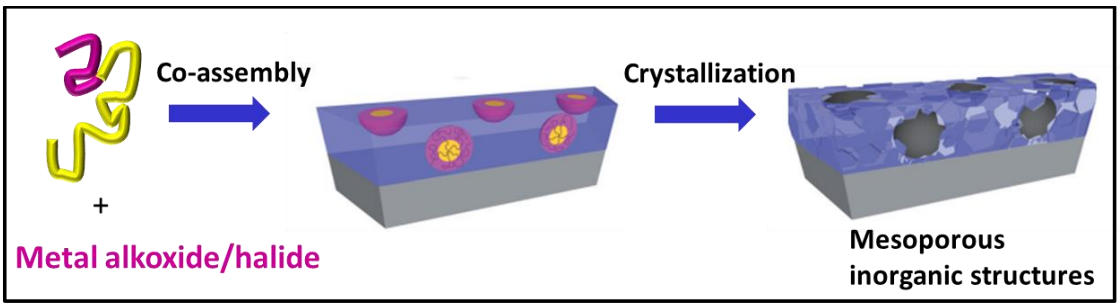

Figure 1.1: Schematic presentation of assembling amorphous matter with block copolymer to produce 3D inorganic architectures

1.3 Persistent Micelle Templating (PMT)

Persistent micelle templating (PMT) is a technique that forms kinetically entrapped block copolymer micelles that do not undergo diameter change while adding inorganic materials, giving the unique ability to decouple the template diameter changes with changes in the material wall-thickness. The size of the equilibrium micelle diameter is majorly determined by the enthalpy of micelle solution interface and the entropy of chain stretching. Micelles could undergo polymer chain exchange in-between micelles to change the micelle

diameter as well as to change in morphology.[11-13] The use of PEO-*b*-PHA which is a high-χ block copolymer as the micelle templating agent provides significant energetic barrier to reorganize the polymer chain itself as well as provide wide solubility window for the tunability purpose. Hence, changing the inorganic:organic (I:O) or material: template (M:T) ratio could allow to independently tune the material wall thickness without changing the pore diameter and the micelle morphology. This unique technique allows to fabricate nano materials with systematically tunable wall thicknesses which could potentially useful to understand ion intercalation into material walls and electron diffusion inside the material walls which will greatly beneficial for designing nano-optimize devices.

The design of PMT requires fulfilment of certain requirements. (1) The $\chi_{solvophobe-solvent}$ barrier must be sufficient to pause the micelle reorganization during the film processing time. (2) Careful selection of proper agitation method is essential to turn on and turn off the reorganization of micelles via surface-limited exchange process that could occur at the air−solvent interface.[14] A strategy preserve the persistent micelles would be to use mild stirring instead of aggressive agitation such as vortexing during the persistent micelle window. (3) The preservation of persistent micelle templates requires that the solution conditions remain un-interrupted even after the addition of inorganic precursor where the hydrolysis can transform the persistent micelles to become dynamic. (4) The achievement of persistent micelles requires a balance of solution conditions for sufficient χ with respect to the particular solvophobic block size because the length of the solvophobic chain determines the kinetics of micelle dynamics. (5) Finally, PMT requires all species to be remained in the solution during the process, including the polymer, the inorganic nanoparticles, and any stabilizing ligands or acids.

1.4 Pseudocapacitive Materials as High Energy and Power Materials

Pseudocapacitance is a fairly new phenomenon which was first reported in 1970s by Conway and other coworkers.[15] Pseudocapacitive materials store electrochemical energy through faradaic processes that involve surface or near-surface fast redox reactions, but their phenomenological behavior and response to experimental variables shows typical capacitor like behavior. Due to these unique features, pseudocapacitive materials have ability to combine higher energy and high power into one materials making them ideal for transportation and grid storage applications. The most widely known pseudocapacitive materials are RuO_2 and MnO_2. Recently other oxides, as well as nitrides and carbides have been identified as pseudocapacitive materials.[1,16] The high energy density associated with pseudocapacitors is due to these faradaic reactions that have approximately ten times higher energy than that of non-faradaic reactions. There are three possible pseudocapacitive processes that can be observed when a redox active material contacts with an electrolyte as shown in Figure 1.1. The (a) underpotential deposition occurs when metal ions form an adsorbed monolayer on a different metal's surface above their redox potential, e.g lead can be deposited on gold surface which is well above lead's redox potential.[1,17] (b) Electrochemically adsorbed ions onto the surface of the electrode undergo redox reactions causing redox pseudocapacitance. During this process, the valency state of the metal ions changes due to faradaic charge transfer. (c) Intercalation pseudocapacitance results when ions intercalate into a redox active material through the tunnels or layers inside the material accompanied by faradaic charge transfer reactions no or very less change in crystallographic phase of the transition metal oxide.

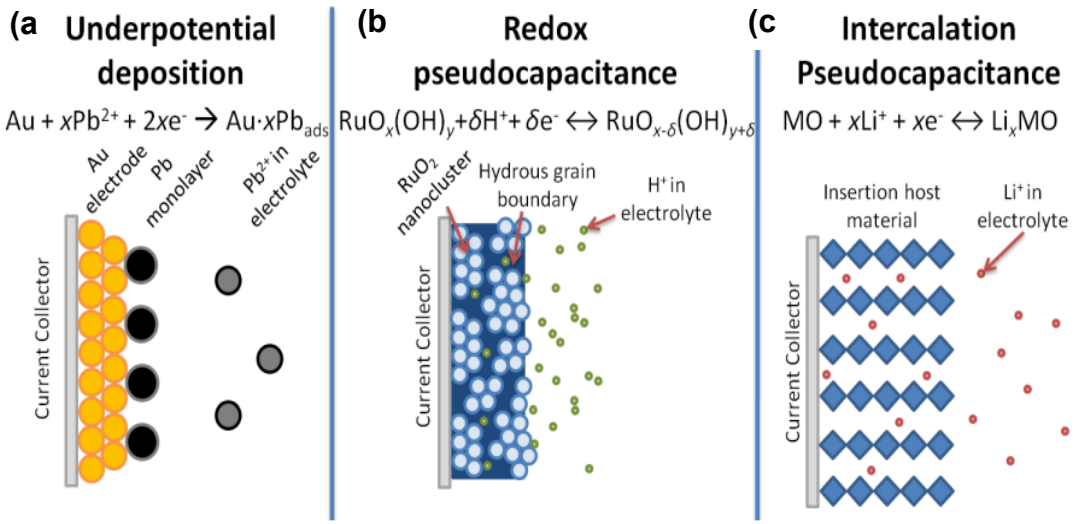

Figure 1.2: Different types of pseudocapacitance mechanisms: **(a)** Underpotential deposition **(b)** Redox pseudocapacitance **(c)** Intercalation pseudocapacitance.[1]

The pseudocapacitive materials show unique features in electrochemical experiments such as (1) in cyclic voltammetry and (2) in galvanostatic cycling. Since redox pseudocapacitance and underpotential deposition are surface dependent processes and they follow simple surface adsorption, the current and sweep rate has a linear relationship in cyclic voltammetry ($I = Cv$). Also, peaks are broad showing capacitive like behavior and have small anodic peak to cathodic peak voltage separation indicating rapid charge storage with no phase change. In constant current experiment, this same phenomenon is indicated by the small voltage hysteresis between the charging and discharging steps. Moreover, the linear response of the potential *vs*. capacity in constant current experiment is also an indication of pseudocapacitance.[1,18]

1.5 Nb_2O_5 as a Pseudocapacitive Material

In 1980's Bard *et al*. demonstrated Li^+ and proton insertion behavior in Nb_2O_5 which led to further research of Nb_2O_5 in the field of LIBs and electrochromic windows.[19]

The amount of lithium insertion in $Li_xNb_2O_5$ varies between x = 1.6 to 2, for a maximum capacity of 726 C g^{-1} or ~ 200 mA h g^{-1}. [5,8] Studies by Dunn *et al.* have shown the high power and high energy capability behavior of orthorhombic niobia (*T*-Nb_2O_5), with nearly 333 F g^{-1} being stored reversibly within 1 min.[16] Furthermore, *T*-Nb_2O_5 exhibits the features representative for pseudocapacitive charge storage behaviour such as broad redox peaks below 2 V in cyclic voltammetry experiment and linear response in constant current experiment. Moreover, very small structural transformation was observed in *T*-Nb_2O_5 upon Li^+ intercalation along the (180) plane in *T*-Nb_2O_5 which was only 3%. Furthermore, *T*-Nb_2O_5 has been categorized as an intrinsic pseudocapacitive material since it shows characteristic of capacitive charge storage for a wide range of particle sizes and morphologies.[1,16,20]

1.6 References

(1) Augustyn, V.; Simon, P.; Dunn, B. *Energy Environ. Sci.* **2014**, *7*, 1597.

(2) Simon, P.; Gogotsi, Y. *Nat Mater* **2008**, *7*, 845.

(3) Zhu, X.; Zhu, Y.; Murali, S.; Stoller, M. D.; Ruoff, R. S. *ACS Nano* **2011**, *5*, 3333.

(4) Lee, J. E.; Yu, S.-H.; Lee, D. J.; Lee, D.-C.; Han, S. I.; Sung, Y.-E.; Hyeon, T. *Energy Environ. Sci.* **2012**, *5*, 9528.

(5) Yuan, F.-W.; Yang, H.-J.; Tuan, H.-Y. *ACS Nano* **2012**, *6*, 9932.

(6) Yang, Y.; Fan, X.; Casillas, G.; Peng, Z.; Ruan, G.; Wang, G.; Yacaman, M. J.; Tour, J. M. *ACS Nano* **2014**, *8*, 3939.

(7) Lim, E.; Kim, H.; Jo, C.; Chun, J.; Ku, K.; Kim, S.; Lee, H. I.; Nam, I.-S.; Yoon, S.; Kang, K.; Lee, J. *ACS Nano* **2014**, *8*, 8968.

(8) Rauda, I. E.; Augustyn, V.; Dunn, B.; Tolbert, S. H. *Acc. Chem. Res.* **2013**, *46*, 1113.

(9) Brezesinski, T.; Wang, J.; Tolbert, S.; Dunn, B. *J Sol-Gel Sci. Technol.* **2011**, *57*, 330.

(10) Orilall, M. C.; Wiesner, U. *Chem. Soc. Rev.* **2011**, *40*, 520.

(11) Halperin, A.; Alexander, S. *Macromolecules* **1989**, *22*, 2403.

(12) Garcia, B. C.; Kamperman, M.; Ulrich, R.; Jain, A.; Gruner, S. M.; Wiesner, U. *Chem. Mater.* **2009**, *21*, 5397.

(13) Alberius, P. C. A.; Frindell, K. L.; Hayward, R. C.; Kramer, E. J.; Stucky, G. D.; Chmelka, B. F. *Chem. Mater.* **2002**, *14*, 3284.

(14) Murphy, R. P.; Kelley, E. G.; Rogers, S. A.; Sullivan, M. O.; Epps, T. H. *ACS Macro Letters* **2014**, *3*, 1106.

(15) Conway, B. E. *Electrochemical supercapacitors: scientific fundamentals and technological applications*; Springer Science & Business Media, 2013.

(16) Augustyn, V.; Come, J.; Lowe, M. A.; Kim, J. W.; Taberna, P.-L.; Tolbert, S. H.; Abruña, H. D.; Simon, P.; Dunn, B. *Nat Mater* **2013**, *12*, 518.

(17) Herrero, E.; Buller, L. J.; Abruña, H. D. *Chem. Rev.* **2001**, *101*, 1897.

(18) Simon, P.; Gogotsi, Y.; Dunn, B. *Science* **2014**, *343*, 1210.

(19) Reichman, B.; Bard, A. J. *J. Electrochem. Soc.* **1980**, *127*, 241.

(20) Kim, J. W.; Augustyn, V.; Dunn, B. *Adv. Energy Mater.* **2012**, *2*, 141.

CHAPTER 2

MESOPOROUS TO MACROPOROUS OXIDES WITH TUNABLE ISOMORPHIC ARCHITECTURES: SOLUTION CRITERIA FOR PERSISTENT MICELLE TEMPLATES[1]

[1] Hasala N. Lokupitiya, Alexis Jones, Barry Reid, Stefan Guldin, Morgan Stefik. *Chem. Matter.*, 2016, 28, 1653-1667. Reproduced with permission from American Chemical Society.

2.1 Abstract

Porous and nanoscale architectures of inorganic materials have become crucial for a range of energy and catalysis applications, where the ability to control the morphology largely determines the transport characteristics and device performance. Despite the availability of a range of block copolymer self-assembly methods, the conditions for tuning the key architectural features such as the inorganic wall-thickness have remained elusive. Towards this end we have developed solution processing guidelines that enable isomorphic nanostructures with tunable wall-thickness. A new poly(ethylene oxide-*b*-hexyl acrylate) (PEO-*b*-PHA) structure directing agent (SDA) was used to demonstrate the key solution design criteria. Specifically, the use of a polymer with a high Flory-Huggins effective interaction parameter, χ, and appropriate solution conditions leads to the kinetic entrapment of persistent micelle templates (PMT) for tunable isomorphic architectures. Solubility parameters are used to predict conditions for maintaining persistent micelle sizes despite changing equilibrium conditions. Here the use of different inorganic loadings controls the inorganic wall-thickness with constant pore size. This versatile method enabled a record 55 nm oxide wall-thickness from micelle coassembly as well as the seamless transition from mesoporous materials to macroporous materials by varying the polymer molar mass and solution conditions. The processing guidelines are generalizable and were elaborated with three inorganic systems, including Nb_2O_5, WO_3, and SiO_2 that were thermally stable to 600 ^oC for access to crystalline materials.

2.2 Introduction

Crystalline transition metal oxides with nanoscale porous structures are in high demand for energy and catalytic applications that take advantage of their high surface area

and interconnected structures. For example, electrochemical devices such as dye sensitized solar cells, mesoscopic perovskite solar cells, batteries, supercapacitors, fuel cells, and photoelectrochemical devices for solar fuels all take advantage of access to crystalline metal oxides with interconnected mesopores. [1-25] The improvement of such devices relies upon judicious optimization of the nanoscale morphology to match the transport limitations of the inorganic materials. Furthermore, many device designs rely on subsequent material deposition[6,26-29] by atomic layer deposition or electrodeposition, for example, and will benefit from architectures that are continuously variable beyond the typical 10-30 nm feature sizes from block copolymers up towards larger 100 nm feature sizes more commonly found from colloidal template techniques. [30-33] Please note the use of IUPAC pore-size naming convention for 2-50 nm mesopores and >50 nm macropores. [34,35] The extension of block copolymer coassembly continuously from the mesoporous regime into the macroporous regime opens up new opportunities for ideal comparative studies that use a single synthesis method. In particular, the inorganic wall-thickness plays a crucial role on device performance where both ion diffusion into the electrode and electron transport along the electrode depend on morphology. [36] Additionally, the wall-thickness affects the overall mass of active material in a given volume and thus influences the energy density of energy storage devices.

Structure directing agents (SDA) enable the evaporation induced coassembly of nanostructured inorganic materials. The field has continuously evolved over the past two decades where typical SDAs are amphiphilic molecules having a hydrophilic portion and a hydrophobic portion covalently bound together. Generally, the hydrophilic portion

selectively interacts with hydrophilic inorganic species via electrostatic or hydrogen bonding while the hydrophobic portion phase separates with nanoscale periodicity.

Surfactant molecules were the first used SDAs[37] where the nominal pore diameter was initially restricted to 1-5 nm and was later expanded with swelling agents. [38,39] The introduction of amphiphilic block copolymer SDAs with significantly higher molar mass expanded the accessible mesopore sizes to 5-30 nm. [40,41] Here, the resulting structural dimensions are dictated by the polymer chain dimensions and is conceptually distinct from vesicle templating. [42-44] A range of BCP SDAs have been elaborated including poly(ethylene oxide-*b*-propylene oxide-*b*-ethylene oxide) [41,45], poly(isoprene-*b*-ethylene oxide), [40] poly(styrene-*b*-ethylene oxide), [46-49] poly(ethylene oxide-*b*-acrylonitrile), [50,51] poly(methyl methacrylate-*b*-ethylene oxide), [52-54] poly(isobutylene-*b*-ethylene oxide), [55-60] poly(ethylene-*alt*-propylene-*b*-ethylene oxide) [61], poly(isoprene-*b*-styrene-*b*-ethylene oxide), [62-64] for nanostructured silicates and transition metal oxides.

Access to continuously tunable isomorphic architectures is crucial in establishing property-performance relationship for novel nanostructured materials. A predictive self-assembly methodology is needed to provide for such nuanced structural control. The approaches used with the numerous BCP SDAs mentioned above, resulted in either mesoporous materials alone or macroporous materials from vesicles where neither strategy has yet enabled continuous tuning of pore sizes across these regimes. [42-44,52,65] Furthermore adjusting the amount of inorganic material in equilibrating systems results in significant morphology changes with different symmetry and changing connectivity[66] that alone may lead to performance changes. Coassembly with non-dynamic micelles[67] is expected over limited experimental conditions where predictive processing guidelines are needed to

enable widespread development. Systematic investigations into length scale dependent properties would ideally be conducted with an isomorphic approach that has capabilities spanning the gamut from mesopores to macropores.

Herein, we present BCP solution processing guidelines that enable tunable isomorphic architectures with adjustable inorganic wall-thickness. This approach enables concomitant access to extensive pore size regimes that seamlessly span from mesopores to macropores. This concept is demonstrated with a new PEO-*b*-PHA SDA. The use of a polymer with sufficiently high Flory-Huggins interaction parameter is needed to inhibit micelle re-equilibration that would otherwise change the final pore size with different inorganic loadings. Both micelle fusion-fission and unimer expulsion-insertion reactions may be slowed with appropriate solution conditions that inhibit micelle changes. [68-72] The demonstrated broad range of tunable pore sizes fills the gap typically found between block copolymer approaches and colloidal approaches. The resulting materials were stable to high temperatures and enabled the formation of multiple crystalline oxide frameworks.

2.3 Experimental section

Reagents: Anhydrous, inhibitor free THF (>99.9%, Aldrich), Niobium (V) ethoxide (99.9%, Fisher) and Tungsten (VI) chloride (99.9%, Acros) were stored inside a glove box and used as received. Concentrated hydrochloric acid (37 wt% ACS grade, VWR) and Tetraethoxysilane (98%, Alfa Aesar) were used as received. Poly(ethylene glycol) methyl ether (M_n 20, 000 g mol^{-1}, Aldrich) was dried by azeotropic distillation with toluene before use.

PEO-Br Macroinitiator Synthesis: PEO-Br was prepared by an esterification procedure. In a typical experiment, 10 g of PEO-OH was dissolved in 33 mL methanol free methylene

chloride, and 0.054 mL of 2-bromopropionic acid was added with nitrogen flow at RT. Then the mixture was cooled to 0 ^{o}C before the addition of 0.0244 g of 4-(dimethylamino)pyridine and 0.1238 g of N,N′-dicyclohexylcarbodiimide (PEO: 2-bromopropionic acid: 4-(dimethylamino)pyridine: N,N′-dicyclohexylcarbodiimide = 1:1.2:0.4:1.2). The reaction was stirred overnight at room temperature. The precipitated dicyclohexylurea was removed by filtration and then the methylene chloride was removed by vacuum. The product was next dissolved in THF and precipitated three into cold diethyl ether (THF:diethyl ether=1:15). The precipitated product was filtered and washed thoroughly with the same solvent and dried at 40 ^{o}C for 24 h inside a vacuum oven. The quantitative reaction of the hydroxyl group of the poly(ethylene glycol)methyl ether was determined by ^{1}H NMR spectroscopy (S1).

PEO-*b*-PHA Diblock Copolymer Synthesis: The monomer hexyl acrylate was passed through a basic alumina column just prior to use. The poly(hexyl acrylate) block was prepared by atom transfer radical polymerization as follows. First 0.75 g of PEO-Br macroinitiator was dissolved in 0.85 mL of DMF inside a schlenk flask and stirred until it dissolved. Moderate heat of ~40 ^{o}C was used to promote dissolution. Then 4.26 mL of hexyl acrylate and 10.4 µL of HMTETA were added to the above mixture. After 10 min of stirring, the solution was subjected to three freeze-pump-thaw (FPT) cycles. At last step, the flask was kept frozen and 5.4 mg of Cu(I)Br was added under flowing nitrogen. Then the flask was sealed under flowing nitrogen and another FPT cycle was carried out. The flask was subsequently kept at room temperature until the mixture was thawed. Then it was kept in a preheated oil bath at 70 ^{o}C with constant stirring. After 17.5 h the polymerization was stopped by cooling the reaction mixture with ice water before exposing the catalyst to

air. The crude polymerization solution was diluted with THF and the solution was passed through a basic alumina column to remove CuBr. The filtrate was concentrated via vacuum and precipitated two times into cold methanol (-78 ^{o}C). The product was filtered and vacuum dried at 40 ^{o}C for 24 h. The molar mass of PHA was determined by ^{1}H NMR relative to the PEO macroinitiator and gel permeation chromatography (GPC) was used to obtain the molar mass dispersity. (Figure A.2)

Synthesis of Different Mesoporous Metal Oxides Thin Films

Nb_2O_5 Wall Thickness Tuning: PEO-*b*-PHA (22.4 mg) block copolymer was dissolved in 2.0 mL of anhydrous inhibitor free THF with continuous stirring for 1 h. The polymer solution was heated up to 40 ^{o}C at the beginning to completely dissolve the polymer. Then 100 µL of 37% w/w conc: HCl was added very slowly to the polymer solution while stirring. The solution was subsequently vortexed for 5 min at 2000 rpm followed by the desired amount of niobium ethoxide as tabulated in Table 2.3. Sample P3-2.4to3.0-Nb_2O_5 was similarly prepared P3-2.4-Nb_2O_5 but had additional acid was added after adjusting the I:O ratio to 2.4. Subsequently, 26 µl of additional niobium ethoxide was added to increase the I:O ratio to 3.0. The resulting solutions were slowly shaken for 1 h before casting. The solution was dip coated onto plasma cleaned 0.25 mm x 0.8 mm silicon wafer at a 4.4 mms^{-1} constant withdrawal rate inside a 20-25 % humidity chamber at 25 ^{o}C. The humidity chamber used in this study was home-made with adjustable purge gas to regulate humidity. Water saturated air was achieved by passing dry air through a submerged aquarium stone. The purge gas humidity was adjusted by the ratio of dry air to humid air, and monitored by a hygrometer. The resulting thin films were placed on a hot plate at 60 ^{o}C for 2 h and heated to 100 ^{o}C for overnight to promote condensation. The plasma cleaner used in this study

was Fisher model 1020 and the plasma was generated with a mixture of 24.6% O_2 balanced Ar. Finally the samples were calcined in air with 10 ^oC/min ramp and 1 min hold at 600 ^oC followed by natural cooling.

WO_3: PEO-*b*-PHA (50 mg) block copolymer was dissolved in 2.8 mL of anhydrous inhibitor free THF with continuous stirring for 1 h. The polymer solution was heated up to 40 ^oC at the beginning to completely dissolve the polymer. Then 0.125 ml of 37% w/w conc: hydrochloric acid was added very slowly to the polymer solution under continuous stirring. The solution was stirred for 1 h before 0.13 g of WCl_6 was added to the solution. Then the same dipping, aging, and calcining procedures described above were used. SiO_2: PEO-*b*-PHA (100 mg) block copolymer was dissolved in 1.54 mL of anhydrous inhibitor free THF. In a separate vial, 0.252 g of tetraethyl orthosilicate (TEOS), 0.12 g of 0.5 M HCl and 0.847 ml of anhydrous inhibitor free THF were mixed together. These two solutions were continuously stirred for 1 h at 60 ^oC and cooled to room temperature before combining the two solutions. The combined solution was then stirred for 2 h at room temperature before dip coating, aging, and calcining was carried out as described above.

Characterization

FE-SEM: Morphologies of the mesoporous thin films were observed with a Zeiss Ultraplus thermal field emission SEM using an acceleration voltage of 5 keV and an in-lens secondary electron detector. The working distance was kept to 3.00 mm or less during the acquisition of the images. Amorphous samples were plasma cleaned prior to imaging and calcined samples were imaged directly. In both cases Cu strips were used to improve electrical contact to the sample.

GISAXS and GIWAXS: X-ray scattering experiments were conducted using a SAXSLab Ganesha at the South Carolina SAXS Collaborative. A Xenocs GeniX3D microfocus source was used with a Cu target to generate a monochromic beam with a 0.154 nm wavelength. The instrument was calibrated using a silver behenate reference with the first order scattering vector $q^* = 1.076\ nm^{-1}$, where $q = 4\pi\lambda^{-1}\sin\theta$ with a total scattering angle of 2θ. A Pilatus 300 K detector (Dectris) was used to collect the two-dimensional (2D) scattering patterns. Radial integration of 2D WAXS patterns reduced the data to 1D profiles using SAXS GUI software. GISAXS and GIWAXS experiments were conducted with an incident angle near 0.22°, and the samples were rotated relative to the incident beam as shown in Figure A.6 The sample-to-detector distance of 1050 mm was used for GISAXS whereas 104.5 mm was used for GIWAXS. The in-plane q_y data were processed using Matlab scripts and equation 4.

χ Measurements Using Temperature Controlled Stage: The bulk morphologies of the polymers were obtained at different temperatures using a Linkam Scientific Instruments HFS350X-GI hot stage. For each experiment, the background scattering from the particular pair of mica sheets used to fix the sample was measured before loading polymer. Polymers were dissolved in THF and filtered through 0.2 μm filter and dried prior to use. The melted polymer (40-50 °C) was placed on a mica sheet (thickness of mica ~ 20 μm, 34% X-ray transmission from Molmex Scientific Inc) with a rubber O ring and the next sheet of mica was placed slowly without trapping any air inside the sandwich. The prepared sandwich cell loosely clamped and placed in a vacuum oven for few minutes before sealing and mounting on the Linkam stage. All data acquired for bulk polymer studies were equilibrated for 1 hour and then measured for 1 hour at the desired temperatures with an

incident X-ray flux of ~1.5 M photons per second on the sample. Matrix-assisted laser desorption ionization time-of-flight MALDI-TOF spectroscopy was used to accurately measure the Mn of the commercial PEO homopolymers. Bruker Ultraflex MALDI-TOF/TOF instrument was used to collect the data nitrogen laser source operating at a wavelength of 337 nm and a pulse rate of 3–5 Hz. The matrix used for the experiment was α-cyano-4-hydroxycinnamic acid. The number average molar mass was calculated for each sample used for thermodynamic measurements. Each scattering curve was background subtracted to remove the minimal contributions from the mica sample holders. The data was fitted using Matlab to convolve the Leibler random phase approximation[73] with a Gaussian instrumental point spread function. A common reference lattice volume of 0.118 nm^3 was used to determine the number of lattice sites occupied by each polymer at each temperature based upon temperature dependent density data. Similarly, the volume fractions were calculated at each temperature using the same density data. The instrumental broadening was measured as follows. The beam configuration was adjusted such that the total flux was within the linear intensity regime of the Pilatus detector (~ 1M photons/second) and a direct image of the beam was fitted well with a Gaussian profile. An arbitrary silver behenate sample (TCI America) was measured with the same configuration to determine the peak width associated with the sample alone. The same sample was then measured with other brighter beam configurations used on the polymer samples. The different observed widths of the first silver behenate peak were used to calculate the instrumental broadening factors under particular configurations. The polymer SAXS data were collected with a beam configuration corresponding to Gaussian point

spread function with a full-width half-max (FWHM) 0.0269 nm^{-1}. This minor correction had little effect on the interpreted χ parameters.

Transmission WAXS for Crystallite Size Analysis: Identical thin-film samples were prepared on mica substrates for measurements with a transmission geometry to minimize geometric smearing. The instrumental broadening factor was measured with a WAXS configuration using NIST reference material 640c. The instrumental broadening factor was fit as a Gaussian point spread function with a FWHM 0.0128 nm^{-1} that smeared the NIST instrument-independent FWHM to the FWHM value measured with our WAXS configuration. The same Gaussian point spread function was taken into account to interpret scattering data as a combination of grain-size broadening per the Scherrer formula with the same Gaussian point spread function.

PHA Temperature Dependent Density Measurement: The density of PHA was determined using water displacement with a pycnometer at different temperatures. Initially liquid PHA was placed in a pre-weighed pycnometer and the mass of PHA was recorded. Then the container was filled with deionized, degassed water and the entire setup was equilibrated at the desired temperature. After equilibration, a capillary stopper was promptly added to displace the excess water and yield a reproducible total system volume. The volume of water was calculated using tabulated temperature dependent density values and subtracted from baseline measurements to determine the volume of PHA at each temperature. The temperature dependency of the PHA density was found as $\rho_{PHA} = -0.0008 T + 1.064$, where ρ is the density in g/mL and T is temperature in Celsius. These values were confirmed with a secondary measurement of PHA using Helium pycnometer

(AccuPyc II 1340) at fixed temperature and gave a similar value of 1.065 ± 0.004 g cm^{-3} at 22 °C.

Estimation of Solubility Parameters: The group contribution method was used to calculate the Hildebrand parameter of hexyl acrylate based on the enthalpy of evaporation of each group. The volume fractions of each component in the solution mixture were used to calculate the Hildebrand parameters of the different solvent mixtures by assuming each component occupies a volume corresponding to their pure densities. Here values of 18.6, 47.9, and 26 were used for THF, water, and ethanol, respectively. [74]

Derivation of the Relationship between Wall Thickness to I:O Ratio: The relationship between wall-thickness in the (100) plane and I:O ratio was derived by considering a BCC micelle model that only considered the micelle core size and the ratio of inorganic content to organic content. The volume occupied by the PEO chains within the inorganic was not taken in to account. The density of the amorphous niobia sol was a fit parameter determined using a least-squares optimization. The calculated density for amorphous niobia was 1.88 g/cm^3, which is in agreement with prior work that found amorphous sol to have less than half the density of the parent crystalline solids. [45,75]

GPC: Molecular weights and molar mass dispersities were measured using a Polymer Labs PL-GPC-120 GPC with a 515 HPLC pump, a 2410 refractive index detector, and three Styragel columns. The columns consisted of HR1, HR3 and HR4 which have the corresponding effective molecular weight ranges of 100–5000 g mol^{-1}, 500–30 000 g mol^{-1}, and 5000–500 000 g mol^{-1}, respectively. THF was used as the eluent at a temperature of 30 °C and a flow rate of 1.0 mL min^{-1} with the calibration of polystyrene standards obtained from Polymer Laboratories. GPC samples were prepared by dissolving the sample in THF

at a concentration of 2.0 mg/mL and passing through micro filters with average pore size of 0.2 μm.

Ellipsometry Prosimetry: Ellipsometric Porosimetry (EP) was carried out on a spectroscopic ellipsometer (Semilabs SE-2000) coupled with an Atmospheric Ellipso-Porosimetry module using water as sorbent and nitrogen as carrier gas. The sample was placed in a chamber in which humidity was controlled by two mass flow controllers that regulate the flow of saturated and dry gas. The ellipsometry measurements were carried out at room temperature at an angle of 73 degrees, corresponding to the approximate Brewster angle of the silicon substrate. Data analysis was then carried out with the software of the instrument (Semilabs Spectroscopic Ellipsometry Analyser). A Tauc-Lorentz dispersion law was applied to the data to obtain values of the refractive index at each humidity point, corresponding to the adsorption of water molecules into the pores. [76] The adsorption-desorption isotherm then allowed to derive both absolute porosity[77] and a pore radius distribution[78] via an effective medium approximation and a modified Kelvin formula, respectively.

Contact angle measurements: A VCA Optima (AST Products, Inc) instrument was used to measure the contact angle with a manual controller capable of casting 2 μl of Milli-Q water droplets. Before taking the measurements, the films were dried using a flow of N_2 for 30 seconds. Static contact angles were measured 5 seconds after placing the drops on the surface. Three measurements were taken to find the average contact angle.

2.4 Results and Discussion

Design and Synthesis of PEO-*b*-PHA

The design of PEO-*b*-PHA to target tunable micellar morphologies had several functional requirements: 1) Both the PEO and PHA blocks have low glass transition temperatures (T_g), ($T_{g\ PEO}$ = -60 ^oC, $T_{g\ PHA}$ = -56 ^oC) to facilitate micelle equilibration at room temperature when favorable solution conditions are presented. [79] 2) The large hydrophilic-hydrophobic contrast represented by the high Flory-Huggins interaction parameter drives phase separation of the blocks and enables modulation of the reorganization kinetics based upon the presented solution conditions. [80-83] 3) The polymer is simple to synthesize in diverse laboratory settings by atom transfer radical polymerization (ATRP) using a chain extension from commercial PEO homopolymers. Different size PEO macroinitiators were synthesized by the esterification of commercial poly(ethylene glycol)methyl ether with 2-bromopropionic acid (Figure A.1). These macroinitiators were then chain-extended using ATRP in DMF to improve polymerization kinetics. [84] Please note that PHA exhibits tacticity with two different chemical environments for **c** protons in the backbone (Figures 2.S2.). The obtained ^{1}H NMR, ^{1}H-^{1}H correlation spectroscopy (COSY) and the ^{1}H-^{13}C heteronuclear single quantum coherence (HSQC) for PEO-*b*-PHA are shown in Figures 2.S2-4, respectively. PEO-*b*-PHA BCPs were synthesized with different molar masses from 8-87 kg mol^{-1} and low molar mass dispersities of 1.06-1.29. The obtained dispersity values from GPC and molar masses from ^{1}H NMR are tabulated in Table 2.1. The resulting polymers were liquid or semi-liquid at room temperature thus fulfilling the first functional requirement.

PEO-*b*-PHA behavior and Flory-Huggins effective interaction parameter (χ)

The behavior of pure PEO-*b*-PHA polymers were investigated by small angle X-ray scattering (SAXS). The data in Figure 2.1 showed clear microphase separation for all polymers **P1**-**P4**, ranging from 12-87 kg mol^{-1} The principle scattering peaks ranged from q = 0.08 to 0.42 nm^{-1}, corresponding to 15.4-74.6 nm spacings that scaled monotonically with polymer molar mass (Table 2.1).

Table 2.1 Molecular and morphological characteristics of the different PEO-*b*-PHAs employed.

Name	PEO g mol^{-1}	PHA g mol^{-1}	vol% of PEO	vol% of PHA	Molar mass dispersity $Đ_m$	Bulk morphology at 70 °C	d-spacing nm *
P1	**5,075**	**7,980**	**0.38**	**0.62**	**1.17**	**Hexagonally packed cylinders**	**15.4**
P2	**20,000**	**18,100**	**0.51**	**0.49**	**1.21**	**Lamellar**	**38.8**
P3	**20,000**	**43,500**	**0.300**	**0.70**	**1.16**	**Hexagonally packed cylinders**	**44.3**
P4	**20,000**	**67,300**	**0.22**	**0.78**	**1.29**	**Short-range phase separation**	**74.6**
P5	**1,900**	**9,900**	**0.15**	**0.85**	**1.14**	**Disordered melt**	**10.0**
P6	**5,100**	**2,960**	**0.62**	**0.38**	**1.06**	**Disordered melt**	**12.9**

$*d = \frac{2\pi}{q}$ where *q* is the first observed scattering peak

The low molar mass **P1** formed a well-ordered morphology with numerous higher order reflections at $(q/q^*)^2$ = 1, 3, 4, and 7, consistent with hexagonally packed cylinders. Polymer **P2** similarly showed multiple peaks at $(q/q^*)^2$ = 1, 4, 9, 16, and 25 for a well-ordered lamellar morphology as well as **P3** polymer showed multiple peaks at $(q/q^*)^2$ = 1,

4, 7, 9 for a well-ordered hexagonally packed cylinder morphology. In contrast, the higher molar mass **P4** polymer exhibited a single peak with a broad shoulder that made for equivocal interpretation of the morphology. In the solid state, significant chain entanglement for such polymers (>87 kg mol^{-1}) can inhibit equilibration of more ordered morphologies, particularly with a large χ value. [85,86]

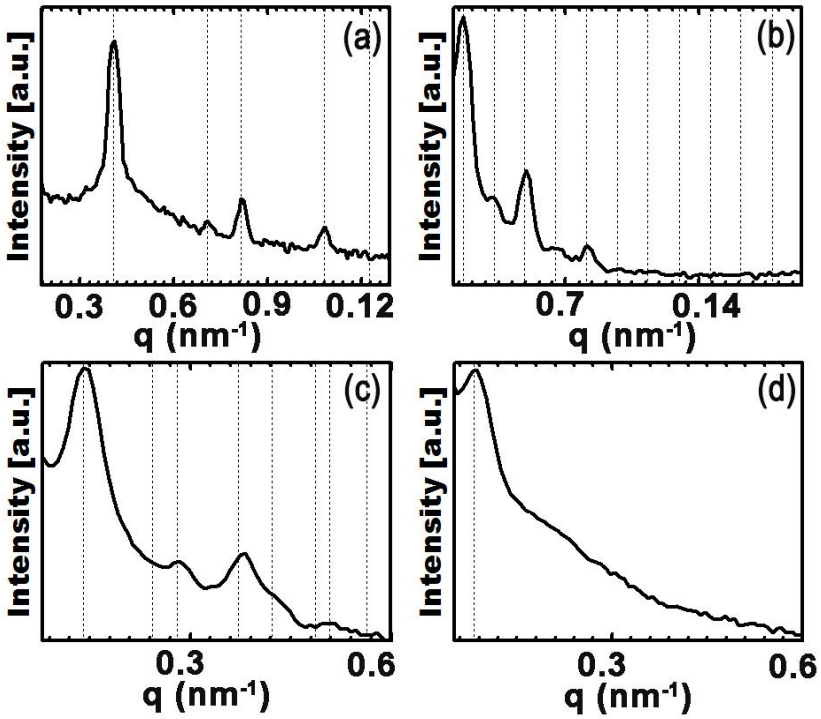

Figure 2.1 SAXS patterns of different PEO-*b*-PHAs in order of increasing total molar mass as measured in situ at 70 °C. (a) **P1** (b) **P2** (c) **P3** (d) **P4**. Dashed lines indicate the first peak followed by the allowed peaks for hexagonal (a, c) or lamellar (b) symmetry.

The thermodynamic properties of block copolymers significantly influence their behavior both in the pure state and in solution. The Flory-Huggins effective interaction parameter χ largely corresponds to the enthalpic interactions of two species although it also includes non-combinatorial entropy. The two species-interaction described by χ may either be between a polymer block and the solvent or between a pair of different polymer blocks. The magnitude of χ scales inversely with temperature where heating can be used to

drive mixing rather than phase separation. [87] The χ value between two polymer blocks can be determined by several methods. [73,87,88]

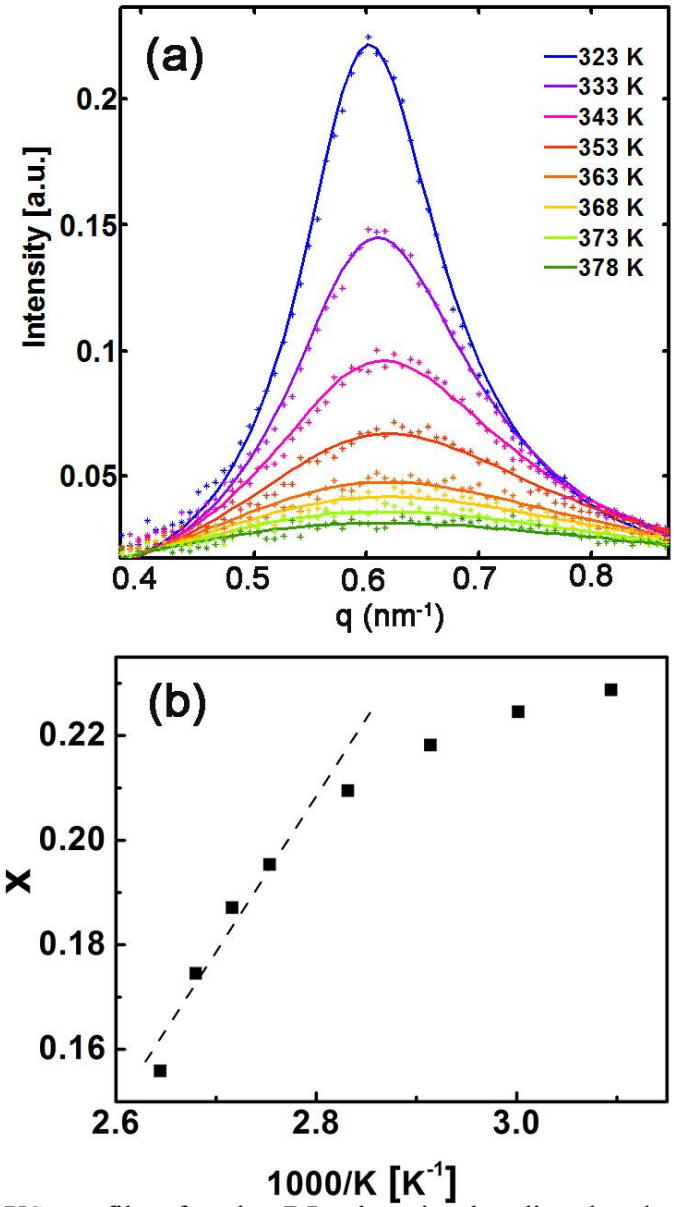

Figure 2.2 The SAXS profiles for the **P5** taken in the disordered melt at different temperatures. The solid lines are the best fits to the experimental data (*) using the random phase approximation at each temperature (a). The temperature dependence of the Flory-Huggins effective interaction parameter χ resulting from best-fits (b).

One method is to measure the order-to-disorder transition (ODT) for a series of block copolymers of the same composition but different molar masses and obtain χ from

the mean field theory (MFT) prediction of the spinodal point. Of the polymers examined here, only **P1** had an experimentally observable order-to-disorder transition temperature of 200 °C. Alternatively, the application of Leibler's random phase approximation (RPA) [73,89-92] gives multiple temperature dependent values of χ for each polymer and is useful to compare polymers of various compositions. The RPA method models the structure factor dependence of disordered melts above the ODT where mean-field theory (MFT) is well suited. A caveat is that fluctuation effects dominate near the ODT so sufficient excess temperature is needed for meaningful data. Both **P5** and **P6** had experimentally useful temperature ranges for the disordered melt above the PEO melting point and below the observed decomposition onset temperature of 240 °C. Here we focus our discussion on the PHA-rich **P5** that was most similar in composition to the polymers employed for coassembly. The SAXS data were collected at different temperatures with a temperature controlled sample stage. The resulting SAXS profiles were fitted using the RPA model to extract the temperature dependent values of χ. The disordered phase scattering intensity S, can be written as a function of scattering vector q as:

$$N/S(q) = F(x,f) - 2\chi N \tag{1}$$

where $x = (q R_g)^2$ and $F(x,f)$ is a combination of Debye functions which can be written as,

$$F(x,f) = \frac{g(1,x)}{g(f,x)g(1-f,x) - \frac{1}{4}[g(1,x) - g(f,x) - g(1-f,x)]^2} \tag{2}$$

Here R_g is the radius of gyration of the BCP chains in the unperturbed state and N is the number of lattice sites occupied using a common reference lattice volume of 0.118 nm^3. [73,93] The background scattering from the mica windows was subtracted before fitting. The experimental scattering profiles were fitted using a least-squares optimization for Leibler's RPA model combined with the measured instrumental broadening factor (Figure 2.2a). The best-fits extracted the R_g and χ at each temperature. The temperature dependence of χ was found to be $\chi = 274.5/T - 0.5636$ for **P5** (Figure 2.2b). A similar molar mass polymer that was PEO-rich **P6** polymer yielded lower χ values (Figure A.5). This non-ideality may be due to the very asymmetric geometry of PHA relative to PEO. [94] Thus $\chi_{PEO\text{-}PHA} = 0.34$ was calculated at 30 ^oC from **P5** for comparison to $\chi_{PEO\text{-}PPO} = 0.085$ and $\chi_{PI\text{-}PEO} = 0.33$ at the same temperature. [92,95] Notably PEO-*b*-PHA has a 4 times larger χ value than PEO-*b*-PPOs and a slightly larger χ than PI-*b*-PEOs. Thus PEO-*b*-PHA serves as a suitable high χ polymer for the kinetic entrapment of micelles.

Guidelines for Selective Tuning of Oxide Wall-Thickness

Solution conditions may be designed to deliberately impede micelle equilibration[96,97] during coassembly to preserve a persistent population or pore-generating species. This feature is key to enable isomorphic studies where changing inorganic quantities implies changing solution conditions that would otherwise impose an altered micelle size. [70,72,97-99] Here we track the inorganic quantity with the inorganic-to-organic ratio (I:O) that compares the mass of the fully condensed oxide material to the mass of BCP, with the assumption of complete conversion of all metal containing precursors. A coassembly strategy relying on frozen or persistent micelles must consider the thermodynamic χ parameter between the solvophobic blocks and the solvent mixture. Here,

the use of Hildebrand solubility parameters is insightful to estimate the thermodynamic barrier for polymer rearrangement based upon simple measurements of the intermolecular interaction strength of each species. [74] The χ_{12} value scales with the square of the difference of the respective Hildebrand solubility parameters (δ) for components 1 (solvophobic block) and 2 (solvent mixture):

$$\chi_{12} = \frac{v}{k_b T}(\delta_1 - \delta_2)^2 \quad (3)$$

Where υ is the average molecular volume, k_b is the Boltzmann's constant and T is the temperature. With a sufficient barrier for polymer rearrangement, changing the I:O ratio (oxide:polymer) changes the spacing between micelles without changing the micelle size markedly. Please note that kinetic entrapment is the key to this technique since any change in the solution solubility parameter will change the equilibrium micelle size. Such persistent micelles enable a unique level of coassembly control with independently tunable inorganic wall thickness while preserving the pore morphology. Such isomorphic yet tunable architectures provide the ideal platform for fundamental measurements of nanoscale phenomena. This approach is significantly different from equilibrating strategies that result in different morphologies with different I:O ratios. [45,66]

The design of conditions for PMTs has several requirements in need of consideration. 1) First and foremost, the $\chi_{\text{solvophobe-solvent}}$ barrier must be sufficient to halt micelle reorganization on the timescale of film processing. This is most directly tunable by changing the composition of the solvent mixture where the resulting solubility parameter is the sum of the product of each component's solubility parameter with its volume fraction. 2) Although the dynamics of high χ BCP aqueous solutions are often immeasurable slow when quiescent, different methods of agitation were recently shown to enable the

reorganization by a surface-limited exchange process at the air−solvent interface. [99] A strategy preserving persistent micelles should therefore use mild stirring in lieu of aggressive agitation such as vortexing. 3) Tuning of wall-thickness with different I:O ratios may require adjustment of the solution composition to account for water consumption by hydrolyzing inorganic species. The preservation of persistent micelle templates requires that the conditions remain non-ergodic after the addition of inorganic precursor. This subtle point is elaborated below where the result of hydrolysis can transition persistent micelles to become dynamic. 4) The length of the solvophobic chain determines the kinetics of micelle dynamics and was shown to have a hypersensitive double-exponential dependence. [96] Thus, achieving persistent micelles requires a balance of solution conditions for sufficient χ with respect to the particular solvophobic block size, *vide infra.* 5) All species must remain in solution throughout the process, including the polymer, the inorganic nanoparticles, and any stabilizing ligands or acids. Most polymers are fairly hydrophobic where solvents such as methanol and water are typical precipitation agents. On the contrary, oxide nanoparticles are often soluble in rather polar solvents. The selection of suitable solvents is often rather limited where much coassembly has been carried out with THF, DMF, [100] anisole, [63] and toluene/butanol [101] mixtures where solvents like ethanol[102] and butanol [103]have also worked with polymers having low χ or low molar mass. 6) Lastly, the components of solvent mixtures generally have different volatilities where evaporation leads to the enrichment of the higher boiling component and will thus change the solubility parameter of the solvent mixture during evaporation. [80,101] The use of PMTs requires that the polymer chains remain under kinetic control throughout the entire process.

The morphology of a representative sample from **P3** is described before elaborating the PMT strategy. A combination of SAXS and SEM was used to characterize each sample. The films prepared from **P3** all exhibited scattering patterns with multiple well-resolved peaks. SAXS patterns from these samples revealed pronounced film texture consistent with a body centered cubic (BCC) morphology where each crystalline grain has either the [110] or [100] zone axis aligned with the film normal and with a random orientation within the sample plane. [104] For example, sample **P3-1.2-Nb_2O_5** when measured in a grazing incidence (GISAXS) geometry exhibited localized $(110)_{[110]}$ and $(101)_{[110]}$ peaks consistent with [110] oriented BCC grains, but also included some additional intensity consistent with $(110)_{[100]}$ peaks with [100] textured BCC grains (Figure 2.3a). The same film was prepared on X-ray transparent mica substrates for incident angle-dependent SAXS measurements using a transmission geometry (Figure 2.3b-e). As was previously calculated[104] for a tilt series of this BCC mixed texture, tilting the sample at low incident angles (here 0-7.5˚) preserved the $(110)_{[110]}$ peaks which then disappeared at higher incident angles (here 20˚+) as a result of the finite thickness of the Ewald sphere (Figure 2.3d). At both 20˚ and 30˚ incident angle, peaks consistent with the $(110)_{[100]}$ from [100] BCC textured grains were clearly observed, strengthening the interpretation of a mixed texture BCC morphology. The scattering patterns were elongated relative to the film normal where the asymmetry was maximum near 0˚ incident angle. The trend in elongation is indicative of film compression along the film normal and is common for coassembled systems. [62,75,104-107] The $(101)_{[110]}$ peak exhibited a d_{101}=33.9 nm^{-1} spacing that corresponded to a mixture of lattice constant orientations including both in-plane (uncompressed) and out-of-plane (compressed) directions. The purely in-plane lattice constant was calculated by fitting an ellipse to the

elongated first ring scatting pattern corresponding to the 110 family of planes at different orientations. The in-plane lattice parameter was calculated from the in-plane position of this ring at q_z=0, and yield a value of a=38.9 nm.

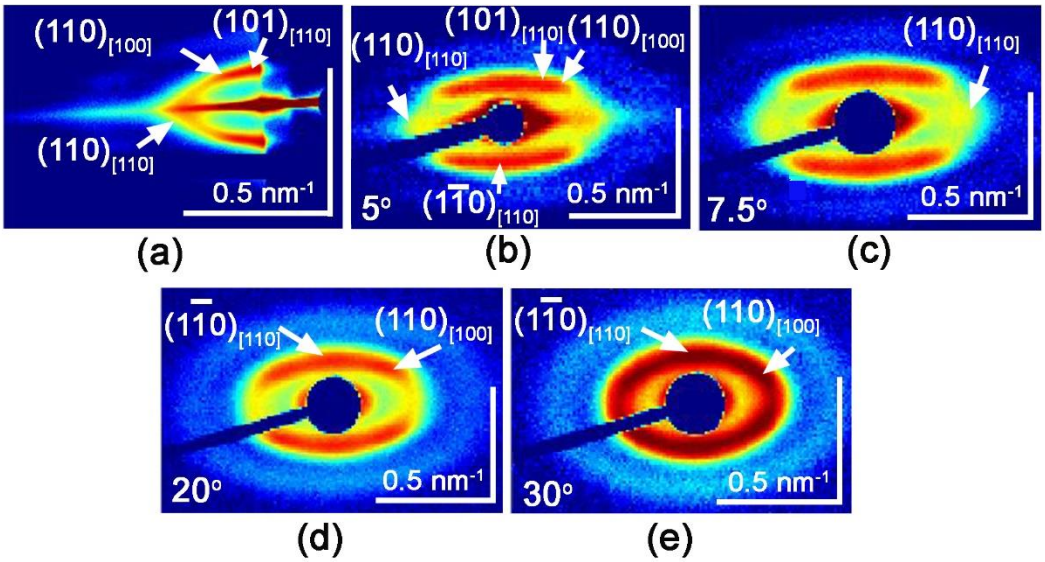

Figure 2.3 2D SAXS patterns of **P3-1.2-Nb_2O_5** at different incident angles from grazing incidence (a, α_i = 0.22° silicon wafer) to transmission from 5-30° (b-e, mica substrates). Reflections consistent with specific planes arising from specific crystalline orientations relative to the substrate are indicated with arrows and are labeled with parenthesis and bracket subscripts, respectively. All color scales correspond to the log of the X-ray intensity.

SEM images of **P3-1.2-Nb_2O_5** after calcination exhibited a characteristic pore size (black) with a periodic niobium oxide (white) structure (Figure 2.4a). The in-plane orientation recorded by SEM is expected to have 2-fold symmetry for the [110] textured grains and 4-fold symmetry for the [100] textured grains. The recorded electron micrographs were consistent with both expected textures, although the local disorder complicated the interpretation. The small grain sizes were indicative of limited long-range order at the surface and led to a range of in-plane lattice parameters from 33.5-35.2 nm.

Table 2.2 Average pore diameter and wall-thickness of calcined Nb_2O_5 thin films by varying the I:O ratio with **P3** and **P4** polymers.

Sample name	Average pore diameter from SEM (nm)*	Pore diameter standard deviation (nm)	Average wall-thickness from SEM (nm)*	In-plane d-spacing from GISAXS (nm)	In-plane lattice parameter from SEM (nm)
BCC micelle morphology					
P3-1.2-Nb_2O_5	24.9±0.6	2.7	10.6±0.5	38.9**	33.5-35.2
P3-2.4-Nb_2O_5	24.6±0.8	3.8	18.2±0.8	40.4**	41.2-45.4
P3-3.0-Nb_2O_5	19.8±0.5	2.7	22.8±2.5	45.4**	39.08-43.5
P3-2.4to3.0-Nb_2O_5	24.6±0.7	3.6	23.8±0.8	44.5**	41.3-51.1
Disordered micelle morphology					
P4-1.2-Nb_2O_5	57.0±2.5	11.3	13.1±0.8	67.9†	-
P4-2.4-Nb_2O_5	54.5±1.5	11.8	36.3±0.9	68.0†	-
P4-3.0-Nb_2O_5	56.2±3.2	14.5	55.7±2.8	No peak was observed	-

* where the average is reported ± the error of the mean

** in-plane lattice parameter a $= \frac{2\pi\sqrt{2}}{q_{[1\bar{1}0]}}$ after fitting an ellipse to the scattering pattern

† where $d = \frac{2\pi}{q}$ from the first scattering peak for disordered micelles

These SEM measurements of the in-plane lattice constant were similar to 38.9 nm in-plane lattice constant determined from GISAXS measurements after elliptical correction. GISAXS measurements on the same sample after calcination are shown in Figure A.7 Thus,

for all subsequent **P3** samples, the same elliptical fitting was used to derive the in-plane lattice constant for comparison to the in-plane SEM measurements (Table 2.1, Figure 2.4).

A series of films were prepared using PEO-*b*-PHA to demonstrate the application of the PMT solution design guidelines and were characterized with GISAXS and SEM. The coassembly solutions all had the same amount of solvent, aqueous hydrochloric acid, and polymer at the start of processing, where the main variable was the amount of inorganic precursor added later (Table 2.3). At this first stage extensive vortexing was used to enable micelle equilibration under thermodynamically challenging solution conditions. [99] The addition of inorganic sol precursors leads to hydrolysis reactions that lower the thermodynamic barrier to reorganizing (Figure 2.5). For PEO-*b*-PHA in THF-water mixtures, the solutions with higher water content after hydrolysis will have higher solubility parameters and different equilibrium micelle sizes. However, the use of kinetically limiting conditions enables the preservation of the micelle size distribution. Thus a significant amount of water (3.6 v%) was used to favor high $\chi_{PHA\text{-}solution}$ conditions for micelles with a

starting solution Hildebrand parameter of 19.65 √MPa (Table 2.3, 2.4). Films were dip coated from these solutions and promptly aged at elevated temperatures to drive the condensation of the inorganic material and inhibit subsequent polymer reorganization. The GISAXS patterns of all films showed the specular reflection peak, Yoneda peak, and the scattering signal from the transmitted beam. The specular reflection is located at the position where the reflected angle is equal to the incident angle forming an intense peak.

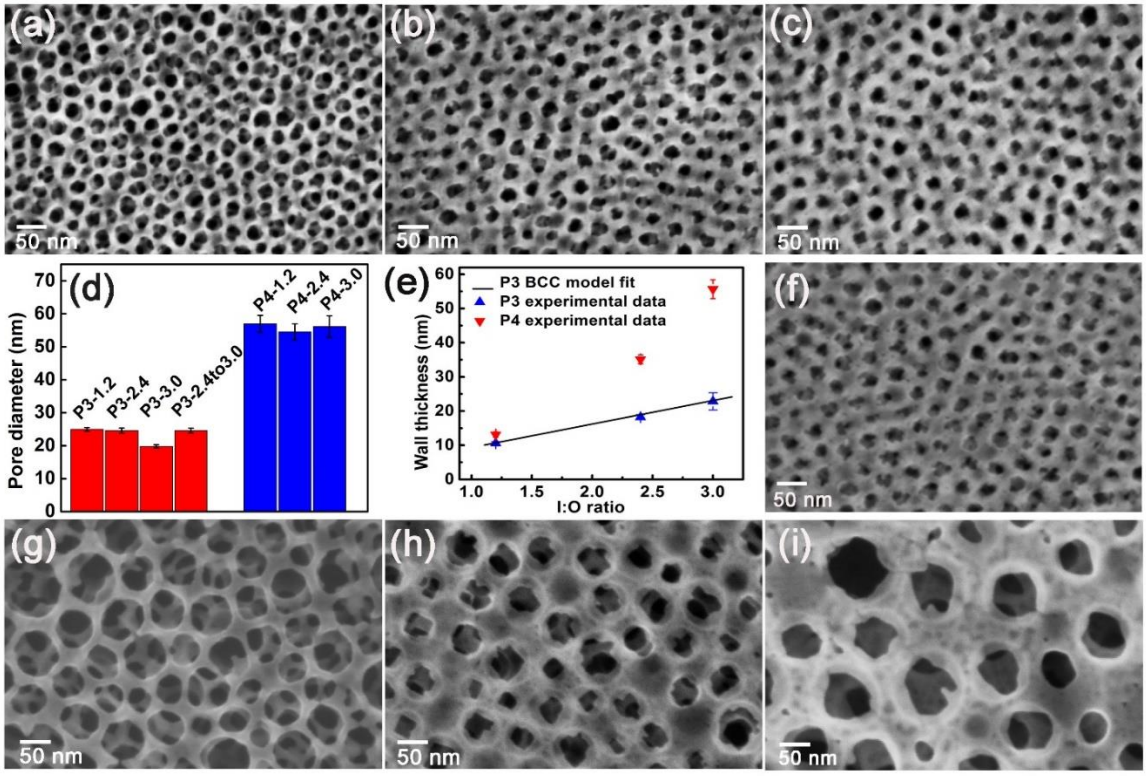

Figure 2.4 SEM images of calcined Nb_2O_5 thin films resulting from polymers **P3** (a-c,f) and **P4** (g-i). From left to right, the films vary by the I:O from 1.2 to 2.4 to 3.0. Film **P3-2.4to3.0-Nb_2O_5** (f) was made by adding additional water before adding further inorganic to reach I:O=3.0 as shown schematically in Figure 2.5c. Average pore diameters are preserved under proper solution conditions for both P3 and P4 samples (d). The tunable wall-thickness was plotted as a function of the I:O ratio used where the data from P3 were fitted well with a simple bcc geometrical model (e).

Sample **P3-2.4-Nb_2O_5** was very similar to the previously described **P3-1.2-Nb_2O_5** sample, with the same lattice parameter determined by GISAXS and an indistinguishable pore size of 24.6±0.8 vs 24.9±0.6 nm, respectively (Figure 2.4a, b and Figure 2.6c). Please note that here we focus on calcined samples and report the average value along with the standard error of the mean to statistically compare pore size populations with several nm of standard deviation. To ease sample comparison, the in-plane scattering vector q_y is plotted for each sample (Figure 2.6d). Both the in-plane scattering angle α_f and the out-of-plane scattering

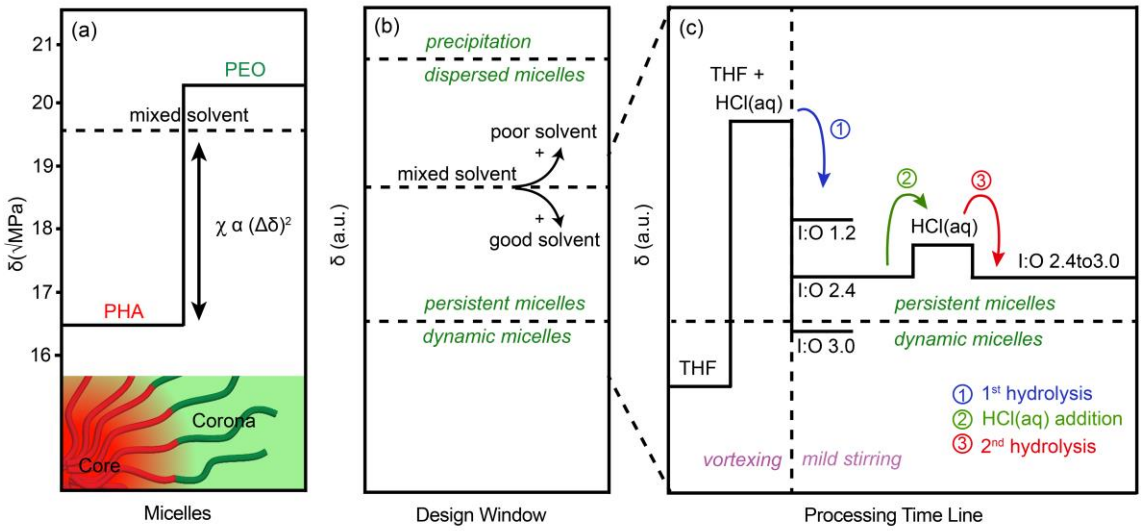

Figure 2.5 Plots of Hildebrand solubility parameters for designing persistent micellar templates. The tunable separation of solubility parameters between the solvophobic block and the solvent (a) estimate the thermodynamic barrier to micelle reorganization. Under vigorous mixing (THF+$HCl_{(aq)}$), the system may equilibrate where as mild stirring conditions result in persistent micelles (b). Coassembly strategies for PMTs must maintain solution conditions for micelles that are dispersed and non-dynamic, or persistent (b). Under vigorous vortexing (THF+$HCl_{(aq)}$), the system progresses towards equilibrium whereas mild stirring conditions preserve persistent micelles (c). The addition of inorganic components shifts the solution conditions through hydrolysis (c) and may be accounted for with rational changes to the solution conditions to preserve persistent micelles.

angle Ψ are used to calculate the q_y component at off-specular conditions where $\alpha_i \neq \alpha_f$ and $2\theta \neq 0$: [108,109]

$$q_y = \frac{2\pi \cos \alpha_f sin\Psi}{\lambda} \quad (4)$$

The in-plane cuts of the scattered intensity as a function of q_y (at constant q_z) were extracted from the 2D detector images by integrating over a stripe of 10 pixels width to improve the signal-to-noise. In contrast to the similar GISAXS patterns (Figure A.7c), these two samples had significantly different oxide wall-thicknesses of 10.6±0.4 and 18.2±0.8 nm for **P3-1.2-Nb_2O_5** and **P3-2.4-Nb_2O_5**, respectively (Figure 2.4e, Table 2.2).

Table 2.3 Synthesis quantities for mesoporous Nb_2O_5 with varying I:O ratios.

Sample name	I/O ratio*	$Nb(OEt)_5$ (mL)	THF (mL)	Polymer (mg)	HCl (mL)	Polymer wt%
1.2-Nb_2O_5	1.2	0.051	2.0	22.4	0.1	1.18
2.4-Nb_2O_5	2.4	0.102	2.0	22.4	0.1	1.09
3.0-Nb_2O_5	3.0	0.128	2.0	22.4	0.1	1.08
2.4to3.0-Nb_2O_5	3.0	0.128	2.0	22.4	0.106	1.07

Here, doubling the I:O ratio led to a nearly doubled oxide wall-thickness while preserving the same pore structure. In contrast, further increasing the inorganic content with sample **P3-3.0-Nb_2O_5** led to a reduced pore size of 19.8±0.5 nm and an increased lattice spacing of 45.4 nm. The statistically significant change in pore size indicates a dynamic micelle population that reorganized in response to the water consumption associated with the hydrolysis of niobium ethoxide (Figure 2.5c). Indeed, the reduced χ parameter upon addition of hydrolyzing inorganic precursors would favor an equilibrium point with reduced micelle size. Assuming complete hydrolysis that exchanges water for ethanol, the resulting solutions should have 2.73 – 1.43 % water and 1.71 – 4.13% ethanol mixed with THF and would have a Hildebrand parameter of 19.53 – 19.34 √MPa (Table 2.4). [74] This range of solubility parameter values for the solvent mixtures were used with the 16.64 √MPa[74] solubility parameter estimated for PHA range of $\chi_{solvophobe\text{-}solvent}$ values from 0.47-0.51 (Table 2.4). These χ values are close to the transition from persistent micelles to dynamic micelles, *vide infra*, and are lower than more extreme χ=3.5[97] systems to facilitate

equilibration assisted by vortexing. The transition from persistent micelles to dynamic micelles (Figure 2.5b) is suppressed using the PMT approach and may be corrected by increasing $\chi_{PHA\text{-}solution}$ with additional water content to preserve non-ergodic conditions (Figure 2.5). However, adding extra water at the start of the experiment changes the starting conditions for micelle equilibration and can lead to the precipitation of the polymer. Thus a 2-step strategy was developed for **P3-2.4to3.0-Nb_2O_5** starting from the conditions of sample **P3-2.4- Nb_2O_5**, followed by the addition of extra water (HCl) to increase the $\chi_{PHA\text{-}solution}$ before the subsequent addition of further niobium ethoxide to raise the I:O ratio to 3.0 (Figure 2.5c). This systematic approach is designed to preserve the original micelle population and is quantitatively documented in terms of solubility parameters in Table 2.4.

Table 2.4 Solution composition and Hildebrand parameters of the **P3** films during the processing steps.

Sample name	Initial water (vol%)	Expected final water (vol%)	δ THF+HCl	δ After hydrolysis
P3-1.2-Nb_2O_5	3.60	2.73	19.65	19.53
P3-2.4-Nb_2O_5	3.60	1.86	19.65	19.41
P3-3.0-Nb_2O_5	3.60	1.43	19.65	19.34
P3-2.4to3.0-Nb_2O_5 *	3.82	1.64	19.65	19.41

*Starting from I:O 2.4 conditions, the solution δ was increased by adding more HCl to allow for a further addition of niobium ethoxide to reach an I:O ratio of 3.0. See Figure 2.5c.

The resulting SEM images exhibit 24.6±0.7 nm pores that are indistinguishable from samples **P3-1.2-Nb_2O_5** and **P3-2.4-Nb_2O_5** and indicate a return of the assembly conditions to kinetic control for PMTs (Figure 2.4a,b,f). SEM measurements of the oxide

wall-thickness indicated an expansion to 23.8±0.8 nm and a correspondingly increased in-plane lattice dimension of 44.5 nm by SAXS (Table 2.2). The PMT approach with **P3** enabled the systematic control of wall-thickness from 10.6±0.5-23.8±0.8 nm while preserving an isomorphic structure with statistically indistinguishable average pore size and the same pore symmetry (Figure 2.4e, Table 2.2). These observed wall-thickness for the highly ordered **P3** samples agreed well with a simple geometrical model of BCC spheres of constant micelle radius with variable matrix volume as a result of the different I:O ratios:

$$t = r\left(\sqrt[3]{\left(\frac{\rho_{org}}{\rho_{inorg}}x + 1\right)\frac{8\pi}{3}} - 2r\right) \quad (5)$$

where t is the wall-thickness, r is the pore radius, ρ_{org} is the PHA density, ρ_{inorg} is the inorganic density and x is the I:O ratio. A natural result of this model is the expansion of the BCC lattice parameter with increasing inorganic content, as was observed by GISAXS (Table 2.2). Samples prepared from the higher molar mass **P4** exhibited similar morphology trends with larger feature sizes. The SEM images for **P4** films are shown in Figure 2.4a-c where the wall-thickness is monotonically controllable from 13.1±0.8 to 36.3±0.9 to 55.7±2.8 nm (Figure 2.4e, Table 2.2). The significant 55.7 nm average wall-thickness for sample **P4-3.0-Nb_2O_5** represents the largest wall-thickness obtained from a micelle coassembly approach. [41,67,80,110] In contrast to **P3**, the micelles of **P4** are significantly larger and have a larger standard deviation due to the significant chain length dependence for the initial equilibration step. [96] The morphologies resulting from **P4** coassembly thus had less long range order than **P3**, which is as expected for a polymer that forms only short-range ordered structures in the pure state after annealing (Figure 2.1d).

The pore sizes for **P4-1.2-Nb_2O_5** and **P4-3.0-Nb_2O_5** were statistically indistinguishable at 57.0±2.5 and 56.1±3.2 nm, respectively. Interestingly, the same I:O=3.0 solution conditions that failed to kinetically trap the smaller molar mass **P3** were able to kinetically trap the larger molar mass **P4** micelles. This demonstrates that the critical value of $\chi_{solvophobe\text{-}solvent}$ is dependent on the molar mass of the solvophobe, as expected. [96]

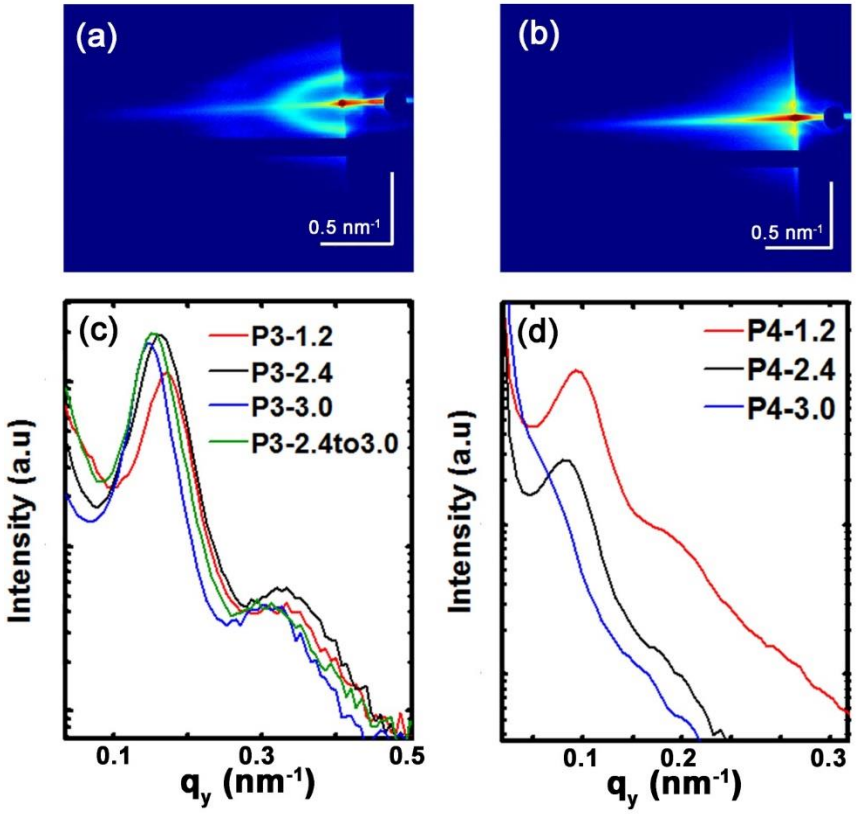

Figure 2.6 2D GISAXS images measured at an incidence angle of $\alpha_i = 0.22^o$ for as-made **P3-1.2-Nb_2O_5** (a) and **P4-1.2-Nb_2O_5** (b). The in-plane cuts of the scattered intensity as a function of *qy* (at constant *qz*) were extracted from the 2D images. 2D image color scales correspond to the log of the X-ray intensity.

GISAXS patterns of most **P4** samples produced several in-plane spots that elongated along q_z (Figure 2.6b,d). Considering the width of the pore size distribution for **P4** samples (Table 2.2), it is not surprising that the SEM images appear to be a disordered

packing of spheres (Figure 2.4g-i). The periodicity of GISAXS peaks from **P4** films were attributed to the random packing of spheres[111] based upon the disorder observed by SEM (Figure 2.4g-i). Such random packing of hard-spheres can have multiple peaks resulting from the radial distribution function where there may not be a simple relationship for the observed scattering peak to the physical dimensions of the system. [111] In particular **P4-3.0-Nb_2O_5** did not exhibit a clear scattering peak, but rather a shoulder near q= ~ 0.08 nm^{-1}, indicating a decrease in long range order (Figure 2.6d). These samples demonstrate the application of a robust conceptual map for tunable nanofabrication with micelles using semi-quantitative guidelines to achieve tunable isomorphic structures from persistent micelle templates. The precise control of pore-size and wall-thickness in the in-plane direction is crucial to a variety of electrochemical devices where transport within the electrolyte and within the oxide both primarily occur normal to the substrate.

Please note that "persistent micelles" do not imply equilibrated micelles at any stage of the processing. Considering the large molar masses and kinetically challenging conditions used here, one should not expect the micelles to fully equilibrate on a laboratory time scale. [99] The effect of the vortexing time and the enthalpic barrier to reorganization (final water content) were studied using **P3** (Figure A.8). As expected, the average micelle diameters monotonically increased with increasing the final water content in the coassemble solutions (Figure A.8 a-c). Comparing different vortexing times, 5 vs 60 min, increasing average micelle sizes were observed with extended agitation, with a more significant effect for samples with higher water content (Figure A.8 d-f). These data evidence slower equilibration kinetics with increasing $\chi_{PHA\text{-}solvent}$ and suggest that much longer agitation times could be used to achieve more-equilibrated and yet larger pore sizes

with a given polymer. The GISAXS data for all the 60 min vortexed samples showed lower q values than the corresponding 5 min vortexed samples, consistent with the formation of larger unit cell lattice parameters (Figure A.9 h).

Crystallization of Oxide Nanostructures

GIWAXS measurements were made on the Nb_2O_5 thin films after calcination to 600 ^oC to demonstrate highly crystalline materials (Figure A.9). The resulting patterns all showed intense isotropic peaks that were consistent with the formation of orthorhombic Nb_2O_5 (PDF #27-1003). Scherrer analysis of **P3-1.2-Nb_2O_5** measured with a transmission geometry on a mica substrate led to an estimated average crystallite size of 7.7 nm that was smaller than the above reported wall-thicknesses. In contrast to Pluronic based coassembly approaches, the large feature sizes accessible with higher molar mass polymers enables larger feature sizes that easily survive the formation of crystallites with high temperature heat treatments.

The calcination of porous films also induced compression along the out-of-plane direction, normal to the substrate. Anisotropic film compression is widely reported and expected for a substrate-supported porous film where the in-plane constraint of substrate dimensions causes significant compression in the out-of-plane direction as the inorganic densifies and crystallizes. [112] In the out-of-plane direction, the pores shrank by 58.2% for **P3-1.2-Nb_2O_5** as evidenced by cross-sectional SEM (Figure A.10). A similar extent of film contraction was reported for sol-gel derived TiO_2 thin films with 47.7% shrinkage. [113] For comparison, the out-of-plane lattice contraction was obtained by GISAXS. The out-of-plane lattice parameter was obtained by fitting an ellipse to the (110) peak to extract the purely out-of-plane component as 9.8 nm. The observed out-of-plane lattice contraction of

74.9% was larger than the contraction of the pores in the same direction, indicating shrinkage of the walls in the out-of-plane direction.

Ellipsometry porosimitry (EP) measurements were performed on **P3-1.2-Nb_2O_5** thin films. Type IV isotherms[114] were observed (Figure 2.7a). A Tauc-Lorentz dispersion law was applied to the data to obtain values of the refractive index at each humidity point, corresponding to the adsorption of water molecules into the pores. [76]

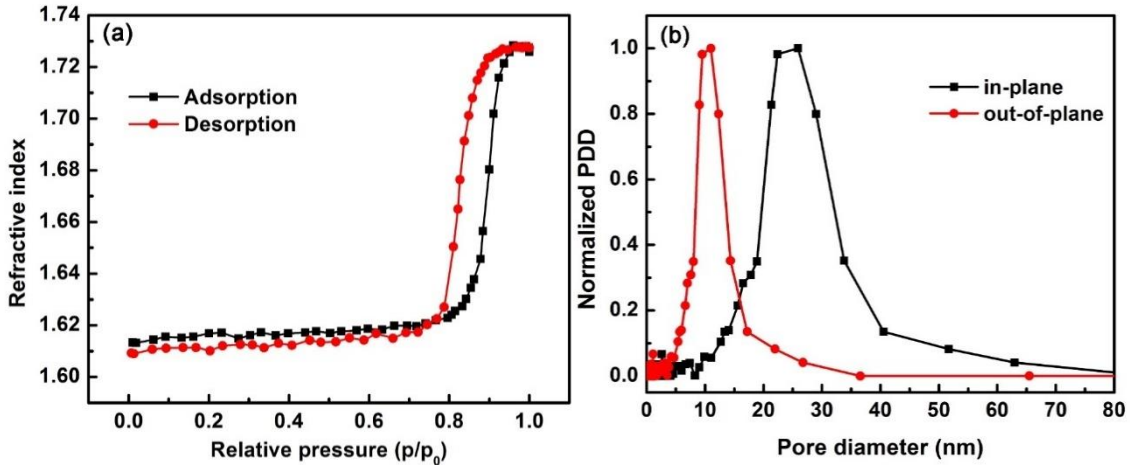

Figure 2.7 Ellipsometric porosimetry of **P3-1.2-Nb_2O_5** sample. Volume adsorbed isotherm (a) as obtained following an Effective Medium Approximation for the refractive index isotherm that corresponds to the adsorption of water molecules into the pores. In-plane and out-of-plane pore diameter distributions (PDD) were obtained from a modified Kelvin model for ellipsoidal mesopores (b). [78]

The volume adsorbed isotherm then relates to the refractive index isotherm following an Effective Medium Approximation. Note that the samples were measured at incremental steps of 0.01 relative humidity to acquire sufficient data points for a well-defined isotherm. The plateau for the adsorption isotherm was reached at a relative pressure of 0.95, indicating that the pores were completely filled. The corresponding pore diameter distribution (PDD) is shown in Figure 2.7b. Based on SEM image analysis, we accounted for the ellipsoidal shape of the pores with an anisotropy ratio of 2.4 between the in-plane

and out-of-plane diameter. A modified Kelvin model that accommodates for the pore anisotropy by a geometric coefficient G was consequently used. [78] Furthermore a contact angle of 43° was taken into account, as experimentally determined for water on a flat sol-gel derived Nb_2O_5 film (Figure A.11). The results for a mean in-plane and out-of-plane pore diameter of 25.5 nm and 10.8 nm, respectively are well in line with data obtained from SEM image analysis, where values of 24.9 nm and 10.6 nm were determined.

Generalization to Diverse Oxides and Pore Size Tuning

The compatibility of micellar templating strategies using PEO-*b*-PHA with diverse oxides was elaborated with WO_3 and SiO_2. The resulting porous WO_3 and SiO_2 films were composed of similar spherical pores as discussed above for numerous Nb_2O_5 samples. SEM images of both the as-made and calcined films of WO_3 and SiO_2 (Figure 2.8) are consistent with disordered spherical micelles, as we previously found for the same **P4** polymer with Nb_2O_5.

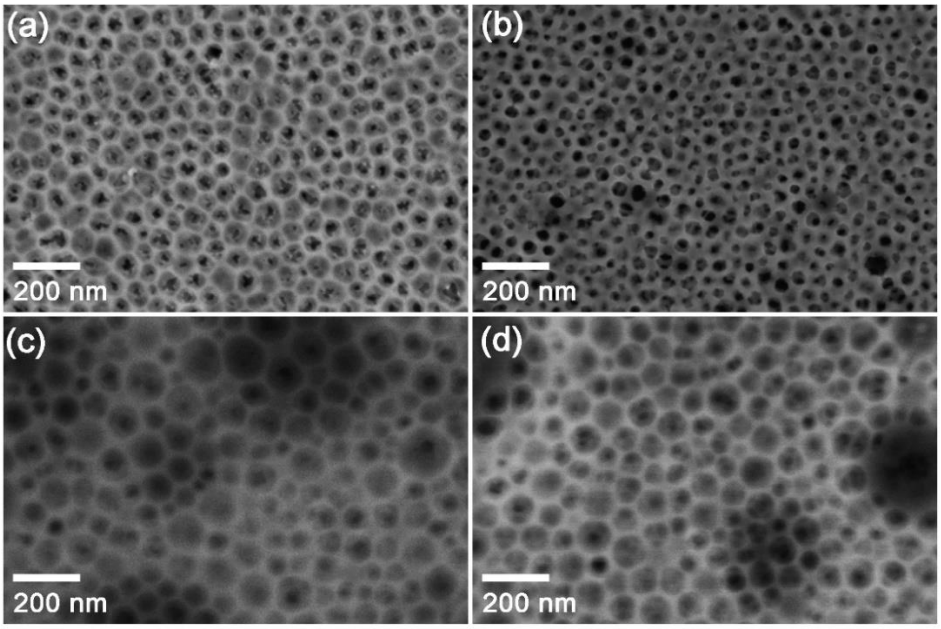

Figure 2.8 SEM images of various inorganic coassembled systems with **P4** polymer: As-made (a) WO_3 and (c) SiO_2, as well as calcined (b) WO_3 and (d) SiO_2.

Table 2.5: Characterization of different mesoporous inorganic systems after calcination.

Inorganic system	Average pore diameter from SEM (nm)*	Pore diameter standard deviation (nm)	Average wall-thickness from SEM (nm)*	GISAXS d-spacing (nm)**
WO_3	35.0±1.4	6.0	26.2±1.1	51.1
SiO_2	75.2±2.9	13.0	16.3±0.6	No peaks

* where the average is reported ± the error of the mean

** $d = \frac{2\pi}{q}$ where the first scattering peak for the disordered micelles

peak at 0.123 nm^{-1} corresponding 51.1 nm periodicity (Figure 2.9a, Table 2.5). In contrast, GISAXS data for SiO_2 did not exhibit clear peaks (Figure 2.9c). As with Nb_2O_5, both WO_3 and SiO_2 survived high temperature calcination to 600 ^oC. The GIWAXS data obtained for WO_3 calcined films showed intense isotropic peaks that were indexed as orthorhombic WO_3 (Figure 2.8b, PDF#89-4479) while SiO_2 remained amorphous at this temperature (Figure 2.9d).

Tunable Pore Size with Solution Conditions and Molar Mass

Continuous access from mesoporous structures to macropores structures is demonstrated with two control parameters: 1) changing the molar mass of the PEO-*b*-PHA block copolymers and 2) by changing the water content during the micelle equilibration stage (Figure 2.5c). The average pore size for a wide variety of samples is shown in Figure 2.10. For example, the several samples prepared with **P4** demonstrate multiple pore sizes as a result of the different water content in the starting solutions (Table 2.6). Here, higher water content increases the $\chi_{solvophobe\text{-}solvent}$ which favors a reduction of total system surface area by expanding the micelles and increasing the aggregation number at the expense of chain stretching.

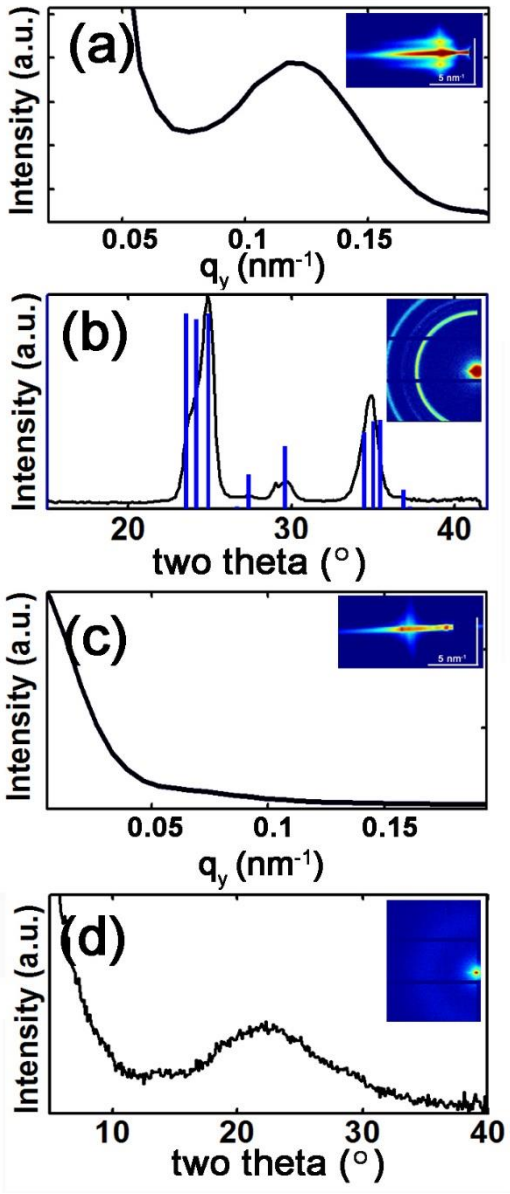

Figure 2.9 GISAXS measurements were used to extract the in-plane scattering intensity as a function of *qy* (at constant *qz*) for (a) WO_3 and (c) SiO_2. (2D images inset). GIWAXS measurements for (b) WO_3 experimental were most consistent with orthorhombic WO_3 PDF # 89-4479 where as the (d) SiO_2 remained amorphous. All 2D image color scales correspond to the log of the X-ray intensity.

Table 2.6: Parameters correlated to the final pore size for micelle scaling relationships

Sample name	N_{PHA}	$\chi_{solvophobe\text{-}solvent}$	Pore diameter (nm)
P2-Nb_2O_5	116.0	0.46	19.5
P3-1.2-Nb_2O_5-5 min vortex	278.8	0.56	24.9
P3-2.4-Nb_2O_5-5 min vortex	278.8	0.63	26.6
P3-3.0-Nb_2O_5-5 min vortex	278.8	0.71	28.9
P3-1.2-Nb_2O_5-60 min vortex	278.8	0.56	25.3
P3-2.4-Nb_2O_5-60 min vortex	278.8	0.63	28.9
P3-3.0-Nb_2O_5-60 min vortex	278.8	0.71	32.1
P4-WO_3	431.4	0.52	35.0
P4-Nb_2O_5	431.4	0.56	57.0
P4-SiO_2	431.4	0.68	75.2

The pore size resulting from polymer micelles was crudely correlated to the assembly conditions using a scaling relationship for equilibrated intermediate micelles. [115,116] Here, the micelle core radius is proportional to $\chi^{9/11} N_{PHA}^{2} N_{PEO}^{-18/11}$ where N_{PHA} is the degree of polymerization of PHA and N_{PEO} is the degree of polymerization of PEO. Here we assume that with persistent micelles, the final pore diameter after calcination scales linearly with the hydrodynamic core diameter. In this study the data obtained were most consistent with an intermediate micelle model that includes the free-energy of the corona and assumes a majority of the hydrophobic block. [116] Despite the use of non-fully equilibrated micelle solutions (Figure A.8), this scaling relationship yielded significant predictive power for correlating changes in both polymer molar mass and in $\chi_{solvophobe\text{-}solvent}$ to the resulting pore size. Notably, the WO_3 sample had smaller pores then predicted by this scaling model which was attributed to the more protic conditions resulting from WCl_6

hydrolysis. More protic conditions could increase the ionic-repulsion of the corona to favor lower aggregation numbers. We also note that P2-Nb_2O_5 deviated slightly from the intermediate model, where such PEO-rich SDAs would likely follow a star-like model. Remarkably, the PMT strategy based upon PEO-*b*-PHA enabled access to pore sizes ranging from 20 to 75 nm that span from mesopores all the way into the macropore regime. This broad range of pore sizes bridges the gap normally found between polymer coassembly and colloidal templating.

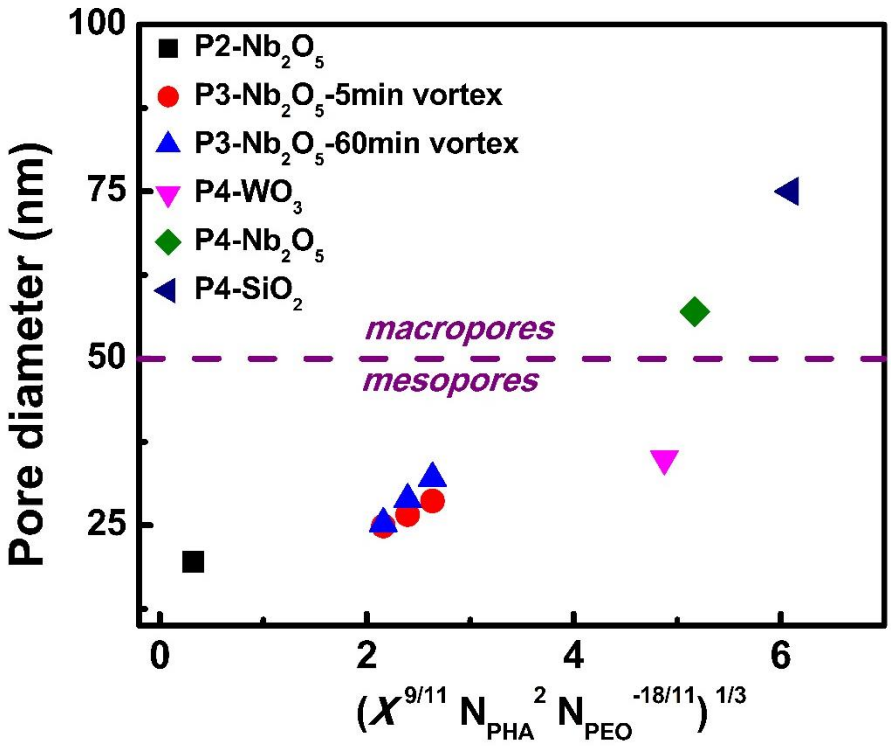

Figure 2.10. A wide range of pore sizes were accessible by changing the polymer block lengths and/or the solution conditions. Pore sizes scaled monotonically with the scaling relationship for intermediate micelles. Here, the core radius and thus the resulting pore diameter should scale linearly with $(\chi^{9/11} N_{PHA}^{2} N_{PEO}^{-18/11})^{1/3}$

2.5 Conclusions

Solution processing guidelines were presented to enable the persistent micellar templating of isomorphic nanostructures. Such architectures are ideal for nanomaterials development with adjustable inorganic wall-thickness and seamless access from mesoporous structures to macropores structures. Under appropriate solutions conditions, a simple adjustment of inorganic-to-organic ratio changes the micelle-to-micelle distance without changing the nominal micelle size. A newly reported PEO-*b*-PHA was used to demonstrate this design concept where the use of a sufficiently high $\chi_{solvophobe\text{-}solution}$ contrast is the key to maintain persistent micelle templates regardless of changing equilibrium conditions.This robust design strategy enabled the achievement of mesopores and macropores with a single design strategy that fills the gap typically found between block copolymer routes and colloidal templating. The resulting materials were high temperature stable and enabled the formation of multiple crystalline transition metal oxide frameworks.

2.6 References

(1) O'Regan, B.; Gratzel, M. *Nature* **1991**, *353*, 737.

(2) Bach, U.; Lupo, D.; Comte, P.; Moser, J. E.; Weissortel, F.; Salbeck, J.; Spreitzer, H.; Gratzel, M. *Nature* **1998**, *395*, 583.

(3) Kojima, A.; Teshima, K.; Shirai, Y.; Miyasaka, T. *J. Am. Chem. Soc.* **2009**, *131*, 6050.

(4) Sudant, G.; Baudrin, E.; Larcher, D.; Tarascon, J.-M. *J. Mater. Chem.* **2005**, *15*, 1263.

(5) Docampo, P.; Guldin, S.; Stefik, M.; Tiwana, P.; Orilall, M. C.; Hüttner, S.; Sai, H.; Wiesner, U.; Steiner, U.; Snaith, H. J. *Adv. Funct. Mater.* **2010**, *20*, 1787.

(6) Rhodes, C. P.; Long, J. W.; Pettigrew, K. A.; Stroud, R. M.; Rolison, D. R. *Nanoscale* **2011**, *3*, 1731.

(7) Bai, H.; Li, X.; Hu, C.; Zhang, X.; Li, J.; Yan, Y.; Xi, G. *Sci. Rep.* **2013**, *3*.

(8) Arthur, T. S.; Bates, D. J.; Cirigliano, N.; Johnson, D. C.; Malati, P.; Mosby, J. M.; Perre, E.; Rawls, M. T.; Prieto, A. L.; Dunn, B. *MRS Bull.* **2011**, *36*, 523.

(9) Ye, Y.; Jo, C.; Jeong, I.; Lee, J. *Nanoscale* **2013**, *5*, 4584.

(10) Batmunkh, M.; Shearer, C. J.; Biggs, M. J.; Shapter, J. G. *J. Mater. Chem. A.* **2015**, *3*, 9020.

(11) Hart, R. W.; White, H. S.; Dunn, B.; Rolison, D. R. *Electrochem. Commun.* **2003**, *5*, 120.

(12) Green, M. A.; Ho-Baillie, A.; Snaith, H. J. *Nat. Photonics* **2014**, *8*, 506.

(13) Mei, A.; Li, X.; Liu, L.; Ku, Z.; Liu, T.; Rong, Y.; Xu, M.; Hu, M.; Chen, J.; Yang, Y.; Grätzel, M.; Han, H. *Science* **2014**, *345*, 295.

(14) Stefik, M.; Heiligtag, F. J.; Niederberger, M.; Grätzel, M. *ACS Nano* **2013**, *7*, 8981.

(15) Bruce, P. G.; Scrosati, B.; Tarascon, J.-M. *Angew. Chem. Int. Ed.* **2008**, *47*, 2930.

(16) Kim, M. G.; Cho, J. *Adv. Funct. Mater.* **2009**, *19*, 1497.

(17) Augustyn, V.; Simon, P.; Dunn, B. *Energy Environ. Sci.* **2014**, *7*, 1597.

(18) Yong Hui, L.; Stefik, M.; Heiniger, L. P.; Peng, G.; Sang Il, S.; Gratzel, M.; Nazeeruddin, M. K. In *Photovoltaic Specialist Conference (PVSC), 2014 IEEE 40th* 2014, p 0943.

(19) Arico, A. S.; Bruce, P.; Scrosati, B.; Tarascon, J.-M.; van Schalkwijk, W. *Nat. Mater.* **2005**, *4*, 366.

(20) Sivula, K.; Le Formal, F.; Grätzel, M. *ChemSusChem* **2011**, *4*, 432.

(21) Lin, Y.; Yuan, G.; Sheehan, S.; Zhou, S.; Wang, D. *Energy Environ. Sci.* **2011**, *4*, 4862.

(22) Hamann, T. W. *Dalton Trans.* **2012**, *41*, 7830.

(23) Wang, Y.; Tang, J.; Peng, Z.; Wang, Y.; Jia, D.; Kong, B.; Elzatahry, A. A.; Zhao, D.; Zheng, G. *Nano Lett.* **2014**, *14*, 3668.

(24) Dunn, H. K.; Feckl, J. M.; Muller, A.; Fattakhova-Rohlfing, D.; Morehead, S. G.; Roos, J.; Peter, L. M.; Scheu, C.; Bein, T. *Phys. Chem. Chem. Phys.* **2014**, *16*, 24610.

(25) Tarascon, J. M.; Armand, M. *Nature* **2001**, *414*, 359.

(26) Rolison, D. R.; Long, J. W.; Lytle, J. C.; Fischer, A. E.; Rhodes, C. P.; McEvoy, T. M.; Bourg, M. E.; Lubers, A. M. *Chem. Soc. Rev.* **2009**, *38*, 226.

(27) Rauda, I. E.; Augustyn, V.; Saldarriaga-Lopez, L. C.; Chen, X.; Schelhas, L. T.; Rubloff, G. W.; Dunn, B.; Tolbert, S. H. *Adv. Funct. Mater.* **2014**, *24*, 6717.

(28) Coustier, F.; Hill, J.; Owens, B. B.; Passerini, S.; Smyrl, W. H. *J. Electrochem. Soc.*

1999, *146*, 1355.

(29) Stefik, M.; Cornuz, M.; Mathews, N.; Hisatomi, T.; Mhaisalkar, S.; Grätzel, M. *Nano Lett.* **2012**, *12*, 5431.

(30) Velev, O. D.; Kaler, E. W. *Adv. Mater.* **2000**, *12*, 531.

(31) Kulinowski, K. M.; Jiang, P.; Vaswani, H.; Colvin, V. L. *Adv. Mater.* **2000**, *12*, 833.

(32) Yi, G.-R.; Moon, J. H.; Yang, S.-M. *Chem. Mater.* **2001**, *13*, 2613.

(33) Phillips, K. R.; England, G. T.; Sunny, S.; Shirman, E.; Shirman, T.; Vogel, N.; Aizenberg, J. *Chem. Soc. Rev.* **2015**.

(34) Rouquerol, J.; Avnir, D.; Fairbridge, C. W.; Everett, D. H.; Haynes, J. M.; Pernicone, N.; Ramsay, J. D. F.; Sing, K. S. W.; Unger, K. K. In *Pure Appl. Chem.* 1994; Vol. 66, p 1739.

(35) Sing, K. S. W. In *Pure and Appl. Chem.* 1985; Vol. 57, p 603.

(36) Okubo, M.; Hosono, E.; Kim, J.; Enomoto, M.; Kojima, N.; Kudo, T.; Zhou, H.; Honma, I. *J. Am. Chem. Soc.* **2007**, *129*, 7444.

(37) Beck, J. S.; Vartuli, J. C.; Roth, W. J.; Leonowicz, M. E.; Kresge, C. T.; Schmitt, K. D.; Chu, C. T. W.; Olson, D. H.; Sheppard, E. W. *J. Am. Chem. Soc.* **1992**, *114*, 10834.

(38) Schmidt-Winkel, P.; Lukens, W. W.; Yang, P.; Margolese, D. I.; Lettow, J. S.; Ying, J. Y.; Stucky, G. D. *Chem. Mater.* **2000**, *12*, 686.

(39) Kimura, T.; Itoh, D.; Shigeno, T.; Kuroda, K. *Bull. Chem. Soc. Jpn.* **2004**, *77*, 585.

(40) Templin, M.; Franck, A.; Du Chesne, A.; Leist, H.; Zhang, Y.; Ulrich, R.; Schädler, V.; Wiesner, U. *Science* **1997**, *278*, 1795.

(41) Zhao, D.; Feng, J.; Huo, Q.; Melosh, N.; Fredrickson, G. H.; Chmelka, B. F.; Stucky, G. D. *Science* **1998**, *279*, 548.

(42) Memesa, M.; Lenz, S.; Emmerling, S. G. J.; Nett, S.; Perlich, J.; Müller-Buschbaum, P.; Gutmann, J. S. *Colloid Polym. Sci.* **2011**, *289*, 943.

(43) Cheng, Y.-J.; Zhou, S.; Wolkenhauer, M.; Bumbu, G.-G.; Lenz, S.; Memesa, M.; Nett, S.; Emmerling, S.; Steffen, W.; Gutmann, J. S. *Eur. J. Inorg. Chem.* **2013**, *2013*, 1127.

(44) Cheng, Y.-J.; Gutmann, J. S. *J. Am. Chem. Soc.* **2006**, *128*, 4658.

(45) Alberius, P. C. A.; Frindell, K. L.; Hayward, R. C.; Kramer, E. J.; Stucky, G. D.; Chmelka, B. F. *Chem. Mater.* **2002**, *14*, 3284.

(46) Deng, Y.; Yu, T.; Wan, Y.; Shi, Y.; Meng, Y.; Gu, D.; Zhang, L.; Huang, Y.; Liu, C.;

Wu, X.; Zhao, D. *J. Am. Chem. Soc.* **2007**, *129*, 1690.

(47) Yu, K.; Hurd, A. J.; Eisenberg, A.; Brinker, C. J. *Langmuir* **2001**, *17*, 7961.

(48) Smarsly, B.; Xomeritakis, G.; Yu, K.; Liu, N.; Fan, H.; Assink, R. A.; Drewien, C. A.; Ruland, W.; Brinker, C. J. *Langmuir* **2003**, *19*, 7295.

(49) Yu, K.; Smarsly, B.; Brinker, C. J. *Adv. Funct. Mater.* **2003**, *13*, 47.

(50) Kruk, M.; Dufour, B.; Celer, E. B.; Kowalewski, T.; Jaroniec, M.; Matyjaszewski, K. *Chem. Mater.* **2006**, *18*, 1417.

(51) Stefik, M.; Lee, J.; Wiesner, U. *Chem. Comm.* **2009**, 2532.

(52) Cheng, Y.-J.; Müller-Buschbaum, P.; Gutmann, J. S. *Small* **2007**, *3*, 1379.

(53) Wei, J.; Li, Y.; Wang, M.; Yue, Q.; Sun, Z.; Wang, C.; Zhao, Y.; Deng, Y.; Zhao, D. *J. Mater. Chem. A* **2013**, *1*, 8819.

(54) Wei, J.; Deng, Y.; Zhang, J.; Sun, Z.; Tu, B.; Zhao, D. *Solid State Sci.* **2011**, *13*, 784.

(55) Groenewolt, M.; Brezesinski, T.; Schlaad, H.; Antonietti, M.; Groh, P. W.; Iván, B. *Adv. Mater.* **2005**, *17*, 1158.

(56) Thomas, A.; Schlaad, H.; Smarsly, B.; Antonietti, M. *Langmuir* **2003**, *19*, 4455.

(57) Brezesinski, T.; Wang, J.; Polleux, J.; Dunn, B.; Tolbert, S. H. *J. Am. Chem. Soc.* **2009**, *131*, 1802.

(58) Wang, Y.; Brezesinski, T.; Antonietti, M.; Smarsly, B. *ACS Nano* **2009**, *3*, 1373.

(59) Brezesinski, T.; Fischer, A.; Iimura, K. i.; Sanchez, C.; Grosso, D.; Antonietti, M.; Smarsly, B. M. *Adv. Funct. Mater.* **2006**, *16*, 1433.

(60) Brezesinski, K.; Haetge, J.; Wang, J.; Mascotto, S.; Reitz, C.; Rein, A.; Tolbert, S. H.; Perlich, J.; Dunn, B.; Brezesinski, T. *Small* **2011**, *7*, 407.

(61) Rauda, I. E.; Buonsanti, R.; Saldarriaga-Lopez, L. C.; Benjauthrit, K.; Schelhas, L. T.; Stefik, M.; Augustyn, V.; Ko, J.; Dunn, B.; Wiesner, U.; Milliron, D. J.; Tolbert, S. H. *ACS Nano* **2012**, *6*, 6386.

(62) Stefik, M.; Wang, S.; Hovden, R.; Sai, H.; Tate, M. W.; Muller, D. A.; Steiner, U.; Gruner, S. M.; Wiesner, U. *J. Mater. Chem.* **2012**, *22*, 1078.

(63) Docampo, P.; Stefik, M.; Guldin, S.; Gunning, R.; Yufa, N. A.; Cai, N.; Wang, P.; Steiner, U.; Wiesner, U.; Snaith, H. J. *Adv. Energy Mater.* **2012**, *2*, 676.

(64) Hoheisel, T. N.; Hur, K.; Wiesner, U. B. *Prog. Polym. Sci.* **2015**, *40*, 3.

(65) Cheng, Y.-J.; Zhi, L.; Steffen, W.; Gutmann, J. S. *Chem. Mater.* **2008**, *20*, 6580.

(66) Garcia, B. C.; Kamperman, M.; Ulrich, R.; Jain, A.; Gruner, S. M.; Wiesner, U. *Chem. Mater.* **2009**, *21*, 5397.

(67) Ortel, E.; Fischer, A.; Chuenchom, L.; Polte, J.; Emmerling, F.; Smarsly, B.; Kraehnert, R. *Small* **2012**, *8*, 298.

(68) Haliloğlu, T.; Bahar, I.; Erman, B.; Mattice, W. L. *Macromolecules* **1996**, *29*, 4764.

(69) Halperin, A.; Alexander, S. *Macromolecules* **1989**, *22*, 2403.

(70) Dormidontova, E. E. *Macromolecules* **1999**, *32*, 7630.

(71) Denkova, A. G.; Mendes, E.; Coppens, M.-O. *Soft Matter* **2010**, *6*, 2351.

(72) Hayward, R. C.; Pochan, D. J. *Macromolecules* **2010**, *43*, 3577.

(73) Leibler, L. *Macromolecules* **1980**, *13*, 1602.

(74) Hiorns, R. *Polym. Int.* **2000**, *49*, 807.

(75) Stefik, M.; Mahajan, S.; Sai, H.; Epps, T. H.; Bates, F. S.; Gruner, S. M.; DiSalvo, F. J.; Wiesner, U. *Chem. Mater.* **2009**, *21*, 5466.

(76) Baklanov, M. R.; Mogilnikov, K. P.; Polovinkin, V. G.; Dultsev, F. N. *J. Vac. Sci. Technol., B* **2000**, *18*, 1385.

(77) Bourgeois, A.; Turcant, Y.; Walsh, C.; Defranoux, C. *Appl. Surf. Sci.* **2009**, *256*, S26.

(78) Boissiere, C.; Grosso, D.; Lepoutre, S.; Nicole, L.; Bruneau, A. B.; Sanchez, C. *Langmuir* **2005**, *21*, 12362.

(79) Simon, P. F. W.; Ulrich, R.; Spiess, H. W.; Wiesner, U. *Chem. Mater.* **2001**, *13*, 3464.

(80) Stefik, M.; Song, J.; Sai, H.; Guldin, S.; Boldrighini, P.; Orilall, M. C.; Steiner, U.; Gruner, S. M.; Wiesner, U. *J. Mater. Chem.A* **2015**, *3*, 11478.

(81) Kelley, E. G.; Murphy, R. P.; Seppala, J. E.; Smart, T. P.; Hann, S. D.; Sullivan, M. O.; Epps, T. H. *Nat. Commun.* **2014**, *5*.

(82) Kelley, E. G.; Smart, T. P.; Jackson, A. J.; Sullivan, M. O.; Epps, T. H. *Soft Matter* **2011**, *7*, 7094.

(83) Luo, L.; Eisenberg, A. *Langmuir* **2001**, *17*, 6804.

(84) Horn, M.; Matyjaszewski, K. *Macromolecules* **2013**, *46*, 3350.

(85) Creutz, S.; van Stam, J.; Antoun, S.; De Schryver, F. C.; Jérôme, R. *Macromolecules*

1997, *30*, 4078.

(86) Creutz, S.; van Stam, J.; De Schryver, F. C.; Jérôme, R. *Macromolecules* **1998**, *31*, 681.

(87) Mori, K.; Hasegawa, H.; Hashimoto, T. *Polym. J.* **1985**, *17*, 799.

(88) Sinturel, C.; Bates, F. S.; Hillmyer, M. A. *ACS Macro Lett.* **2015**, *4*, 1044.

(89) Connell, J. G.; Richards, R. W. *Macromolecules* **1990**, *23*, 1766.

(90) Kim, J. K.; Kimishima, K.; Hashimoto, T. *Macromolecules* **1993**, *26*, 125.

(91) Cochran, E. W.; Morse, D. C.; Bates, F. S. *Macromolecules* **2003**, *36*, 782.

(92) Floudas, G.; Ulrich, R.; Wiesner, U. *The J. Chem.Phys.* **1999**, *110*, 652.

(93) Bates, F. S.; Fredrickson, G. H. *Annu. Rev. Phys. Chem.* **1990**, *41*, 525.

(94) Bates, F. S.; Schulz, M. F.; Khandpur, A. K.; Forster, S.; Rosedale, J. H.; Almdal, K.; Mortensen, K. *Faraday Discuss.* **1994**, *98*, 7.

(95) Hamley, I. W.; Castelletto, V.; Yang, Z.; Price, C.; Booth, C. *Macromolecules* **2001**, *34*, 4079.

(96) Choi, S.-H.; Lodge, T. P.; Bates, F. S. *Phys. Rev. Lett.* **2010**, *104*, 047802.

(97) Won, Y.-Y.; Davis, H. T.; Bates, F. S. *Macromolecules* **2003**, *36*, 953.

(98) Steunou, N.; Forster, S.; Florian, P.; Sanchez, C.; Antonietti, M. *J. Mater. Chem.* **2002**, *12*, 3426.

(99) Murphy, R. P.; Kelley, E. G.; Rogers, S. A.; Sullivan, M. O.; Epps, T. H. *ACS Macro Lett.* **2014**, *3*, 1106.

(100) Stefik, M.; Sai, H.; Sauer, K.; Gruner, S. M.; DiSalvo, F. J.; Wiesner, U. *Macromolecules* **2009**, *42*, 6682.

(101) Guldin, S.; Stefik, M.; Sai, H.; Wiesner, U.; Steiner, U. *RSC Adv.* **2015**, *5*, 22499.

(102) Yang, P.; Zhao, D.; Margolese, D. I.; Chmelka, B. F.; Stucky, G. D. *Nature* **1998**, *396*, 152.

(103) Choi, S. Y.; Mamak, M.; Coombs, N.; Chopra, N.; Ozin, G. A. *Adv. Funct. Mater.* **2004**, *14*, 335.

(104) Ruland, W.; Smarsly, B. M. *J. Appl. Crystallogr.* **2007**, *40*, 409.

(105) Soler-Illia, G. J. d. A. A.; Sanchez, C. *New J. Chem.* **2000**, *24*, 493.

(106) Toombes, G. E. S.; Finnefrock, A. C.; Tate, M. W.; Ulrich, R.; Wiesner, U.; Gruner, S. M. *Macromolecules* **2007**, *40*, 8974.

(107) Schuster, J.; Köhn, R.; Keilbach, A.; Döblinger, M.; Amenitsch, H.; Bein, T. *Chem. Mater.* **2009**, *21*, 5754.

(108) Hexemer, A.; Müller-Buschbaum, P. *IUCrJ* **2015**, *2*, 106.

(109) Paul, N.; Brumbarov, J.; Paul, A.; Chen, Y.; Moulin, J.-F.; Muller-Buschbaum, P.; Kunze-Liebhauser, J.; Gilles, R. *J. Appl. Crystallogr.* **2015**, *48*, 444.

(110) Smarsly, B.; Antonietti, M. *Eur. J. Inorg. Chem.* **2006**, *2006*, 1111.

(111) Wang, X.; Dormidontova, E. E.; Lodge, T. P. *Macromolecules* **2002**, *35*, 9687.

(112) Dutta, S.; Wu, K. C. W.; Kimura, T. *Chem. Mater.* **2015**, *27*, 6918.

(113) Kimura, T.; Yamauchi, Y.; Miyamoto, N. *Chem. Eur. J.* **2010**, *16*, 12069.

(114) Sing, K. S. W.; Everett, D. H.; Haul, R. A. W.; Moscou, L.; Pierotti, R. A.; Rouquerol, J.; Siemieniewska, T. In *Handbook of Heterogeneous Catalysis*; Wiley-VCH Verlag GmbH & Co. KGaA: 2008.

(115) Zhulina, E. B.; Adam, M.; LaRue, I.; Sheiko, S. S.; Rubinstein, M. *Macromolecules* **2005**, *38*, 5330.

(116) Lund, R.; Willner, L.; Richter, D. In *Controlled Polymerization and Polymeric Structures*; Abe, A., Lee, K.-S., Leibler, L., Kobayashi, S., Eds.; Springer International Publishing: 2013; Vol. 259, p 51.

CHAPTER 3

SONICATION-ENABLED RAPID AND TUNABLE EVOLUTION OF HIGH- χN MICELLES AS TEMPLATES FOR ORDERED MESOPOROUS OXIDES[2]

[2] Hasala N. Lokupitiya, Morgan Stefik. *Nanoscale*, 2017, 4, 1393-1397. Reprinted with permission from The Royal Society of Chemistry.

3.1 Abstract

The kinetic-entrapment of block copolymer micelles enables size-persistence, however tuning micelle sizes under such conditions remains challenging. Agitation-induced chain exchange via vortexing is limited by the production of solution-air interfaces. Here, we use ultrasonic cavitation for rapid interface production that accelerates micelle growth by an order of magnitude over vortexing.

3.2 Introduction

Selective solvents drive the aggregation of block copolymers to self-assemble into micelles that partition the solvophobic block into the core of the micelle. Micelles have been widely employed for emulsions, drug delivery, nanoreactors, and soft-templates for inorganic nanoparticles. [1-10] In all these examples, the size of the micelle largely influences the performance. Micelles of diverse dimension are needed for different applications. For drug delivery, the micelles size determines both the loading capacity[11,12] as well as the capability to cross cell membranes. [13-15] For micelle templated bioelectrodes, the pore size must balance the need for surface area enhancement against the need for large enough pores to accommodate biological photoactive species. [4] In this later example, high molar mass block copolymer micelles generated ~80 nm macropores in antimony-doped tin oxide electrodes. With micelle size playing a key role for numerous applications, the capability to kinetically trap a desired persistent micelle size opens up unique opportunities. For example, persistent micelle templating (PMT) uses kinetically trapped micelles for the fabrication of highly tunable porous materials with independent control over both the pore size and the material wall thickness. [16] The use of kinetic entrapment to prevent micelles from responding to changing solutions conditions is crucial to decouple the resulting pore

size from an adjustable wall thickness. The production of persistent micelles was shown to be predictable from a thermodynamic perspective of the solution conditions. [16]

Block copolymer micelles generally evolve through single-chain exchange, micelle fusion/fission or combination of these processes. [17-20] The rate of exchange varies strongly with the thermodynamic barrier for rearrangement. For single-chain exchange, there is a double exponential rate dependence on χN, where χ is between the solvent and the solvophobic block and N is the solvophobic block length. [21-25] For example, a study by Bates *et al* found that a high-χN system of poly(ethylene oxide-*b*-butadiene) in water exhibited negligible chain exchange after 8 days. [25] A recent study by Epps *et al* with the same high-χN system showed that stirring over many days activated a novel exchange process that resulted in a bimodal distribution of micelles. [26] Epps *et al* subsequently identified that agitation-induced chain exchange (AICE) by vortexing was observable over <15 min periods. [27] Here we note that chain exchange is a much faster processes than micelle size equilibration. [20,28] A key finding in this study was that AICE was surface-limited and scaled with the rate of turn-over of the solution-air interface. [25-27] The strong dependence of exchange rate on agitation was recently shown to be a novel method to tune micelle size distributions and then kinetically trap persistent micelles under high-χN conditions. [16] The application of ultrasonic waves to solutions induces continuous cavitation events to form <200 μm diameter bubbles (varies with sonic power and solution) that collapse on the microsecond timescale and can produce ephemeral conditions with pressures of several hundred atmospheres and temperatures up to 5,500 ^{o}C. [29-32] For example, the pistol shrimp uses the disruptive power of cavitation to attack prey. [32] For micelle solutions, the rapid turn-over of solution-air interfaces during sonication should

lead to faster chain exchange and faster changes of micelle size populations. Thus sonication is expected to accelerate surface-limited exchange processes such as AICE (Figure 3.1). Here, we demonstrate that compared to vortexing, sonication enables more than an order of magnitude acceleration of block copolymer micelle growth under high-χN solution conditions.

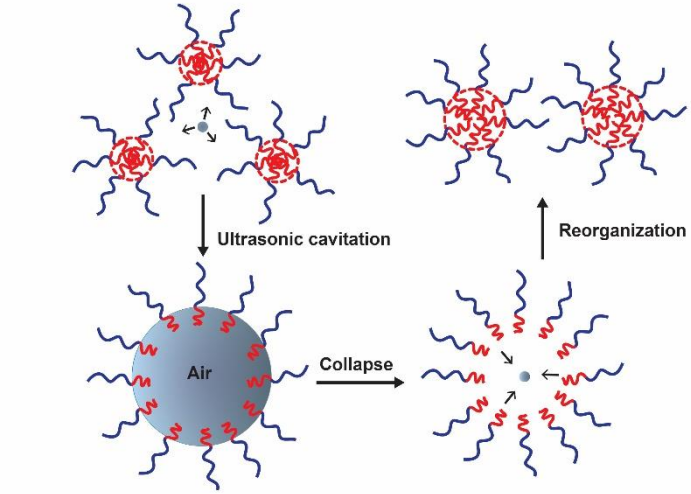

Figure 3.1 Ultrasonic cavitation rapidly creates and eliminates solution-gas interfaces to accelerate agitation-induced chain exchange between block copolymer micelles under high-χN solution conditions.

3.3 Experimental section

This study used poly(ethylene oxide-*b*-hexyl acrylate) (PEO-*b*-PHA) with PEO and PHA molar masses of 20 kg mol^{-1} and 43.5 kg mol^{-1}, respectively, and a molar mass dispersity of $Đ$ = 1.16. The polymer blocks alone have a high effective interaction parameter $\chi_{PEO/PHA}$ = 0.34 at room temperature. [16] The polymer (22.4 mg) was dissolved in 2 mL of anhydrous THF (>99.9%, Aldrich) and 100 µL of 37 wt% HCl(aq) (ACS grade, VWR) was added slowly to introduce 2.7 vol% of water. During this process, kinetically trapped micelles are expected to form before the HCl addition is completed. The HCl(aq) was selected as the water source since the micelle solutions were intended to stabilize metal

oxide nanoparticles at a later point. The resulting micelle solutions were either non-agitated, vortexed for 5 min, vortexed for 60 min, or sonicated for 5 min. Agitation was accomplished with a Fisher digital vortex mixer (Cat. No. 0215370) at 2,000 rpm or a Fisher ultrasonic bath (Cat. No. FS-28) operated continuously at full power (225 W) for 5 minutes (Figure B.1 a). Both processes were started at room temperature. Sonication was visually observed to induce cavitation in sample solutions (Figure B.1 b). The non-agitated solution was inverted three times after adding HCl(aq). Next, 0.051 mL volume of niobium ethoxide (99.9%, Fisher) was added to each sample followed by mild shaking for 1 h before films were dip-coated onto silicon wafers at 4.4 mm s^{-1} under 20-25 % RH as previously described. [16]

3.4 Results and Discussion

The films were calcined at 600 ^{o}C and the resulting porous niobia films were observed by scanning electron microscopy (SEM). Top view images were acquired to determine the in-plane pore diameter statistics using ImageJ. Here, the in-plane pore diameter distribution was used as a proxy for the population of micelle hydrophobic core dimensions. We note that the films were largely crack-free, indicating that in-plane periodicity was not distorted as a result of calcination. Thus, SEM pore size measurements may reasonably be used as a high resolution and monotonic proxy for average micelle core size. Dynamic light scattering (DLS) was also measured where the micelle hydrodynamic radius increased with time of agitation (Figure B.2). In contrast to DLS, SEM enables the production of high-resolution histograms corresponding to the micelle core dimension alone. SEM images of each sample are shown in Figure 2.1 and measurement statistics are tabulated in Table 2.1. Block copolymer micelles are generally reported from ~3-100 nm

where the combination of χ and N used here reasonably result in ~30 nm micelle cores under equilibrium. [15,33-39] The average pore diameter of sample non-agitated was 23.2±0.2 nm while the average pore diameter increased from 24.1±0.2 to 25.8±0.2 nm for samples vortex-5min and vortex-60min, respectively.

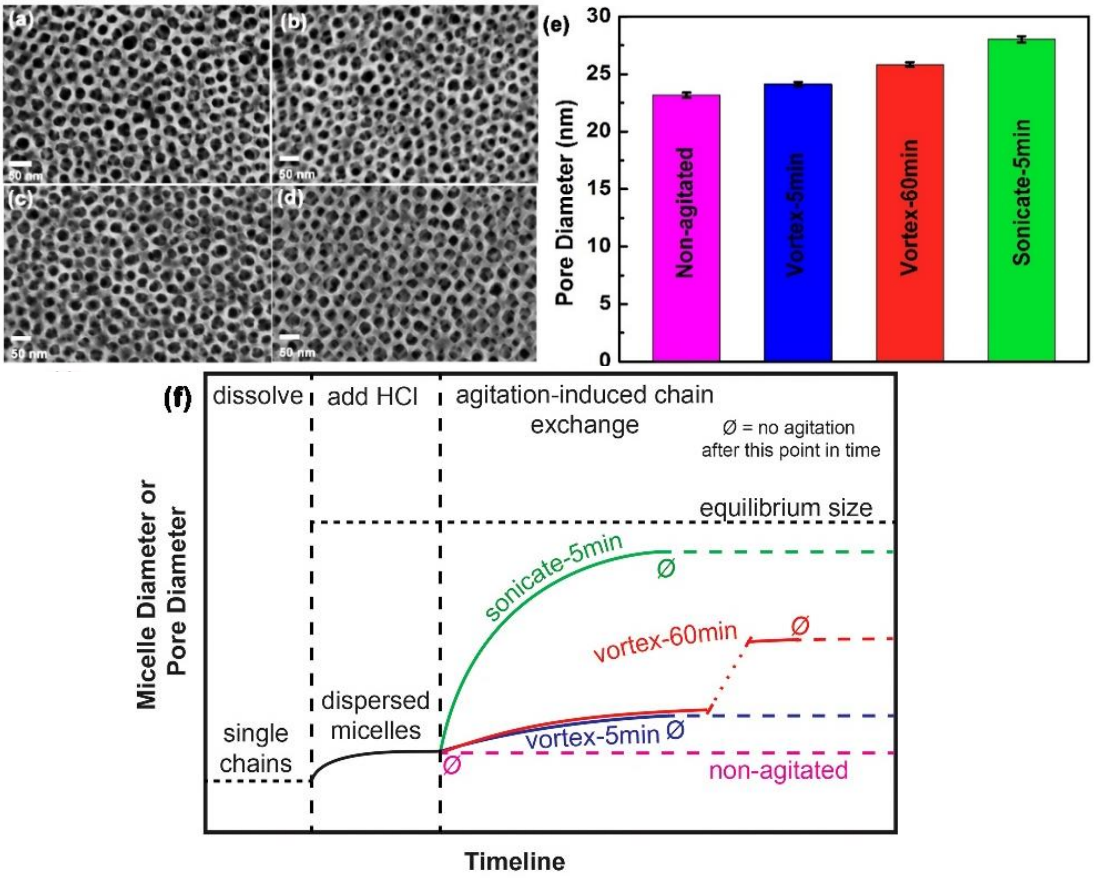

Figure 3.2 SEM images of porous Nb_2O_5 films templated from micelles with different agitation conditions: non-agitated (a) vortex-5min (b), vortex-6min (c), sonicate-5min (d). The average pore diameters and error-of-the-mean varied with agitation method and time (e). The timeline for solution processing predicts a starting point of persistent micelles below the equilibrium size (f). The type of agitation determines the rate of change whereas the agitation time determines the extent of change.

In contrast, sample sonicate-5min resulted in significant 28.0±0.3 nm larger pores, even compared to the 12 times longer agitation used for sample vortex-60min (Figure 2.1, Table 1). Histograms of pore size from several hundred data points for each sample were

well-fit with single Gaussians (Figure 3.3). Considering the previously observed bimodal pathway for micelle evolution, we note that the statistical width may obscure two convolved distributions that are narrowly separated. The observed micelle growth trends were consistent with exchange towards a larger equilibrium size (Figure 3.2e). This is expected considering that the micelles become kinetically trapped part way through the initial HCl(aq) addition. The further increase in water content increases the effective interaction parameter $\chi_{PHA/solution}$, between PHA and the solvent corresponding increase in surface tension shifts the balance of surface energy (enthalpy) to chain stretching (entropy) to favor an increased nominal micelle size. [36]

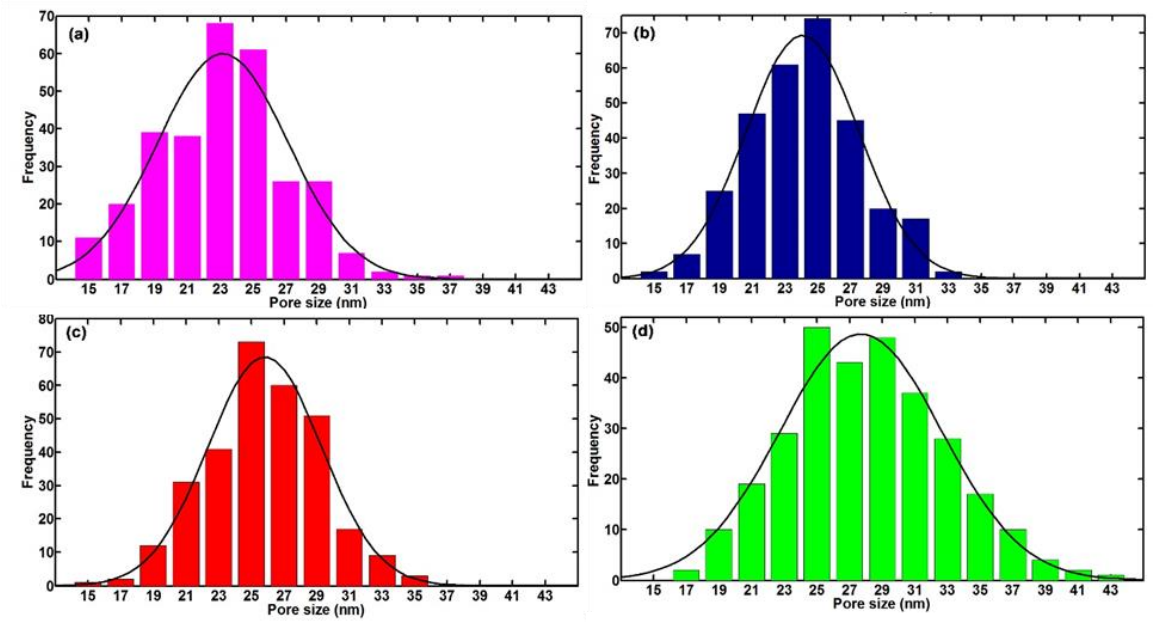

Figure 3.3 Pore sizes in templated films serve as a proxy for the micelle core diameter. Histograms were prepared from analysis of SEM images. The results varied with the type and duration of agitation: non-agitated (a) vortex-5min (b), vortex-6min (c), sonicate-5min (d). Data were fitted with Gaussian distributions.

The use of high-χN conditions, however, inhibits quiescent micelles from undergoing chain exchange towards the new equilibrium (Figure 3.2e). In the context of AICE, an enhancement of the surface turn-over rate is expected to promote faster chain

exchange (Figure 3.2). These results are consistent with faster chain exchange that evolves micelles towards a larger equilibrium size (Figure 3.2e).

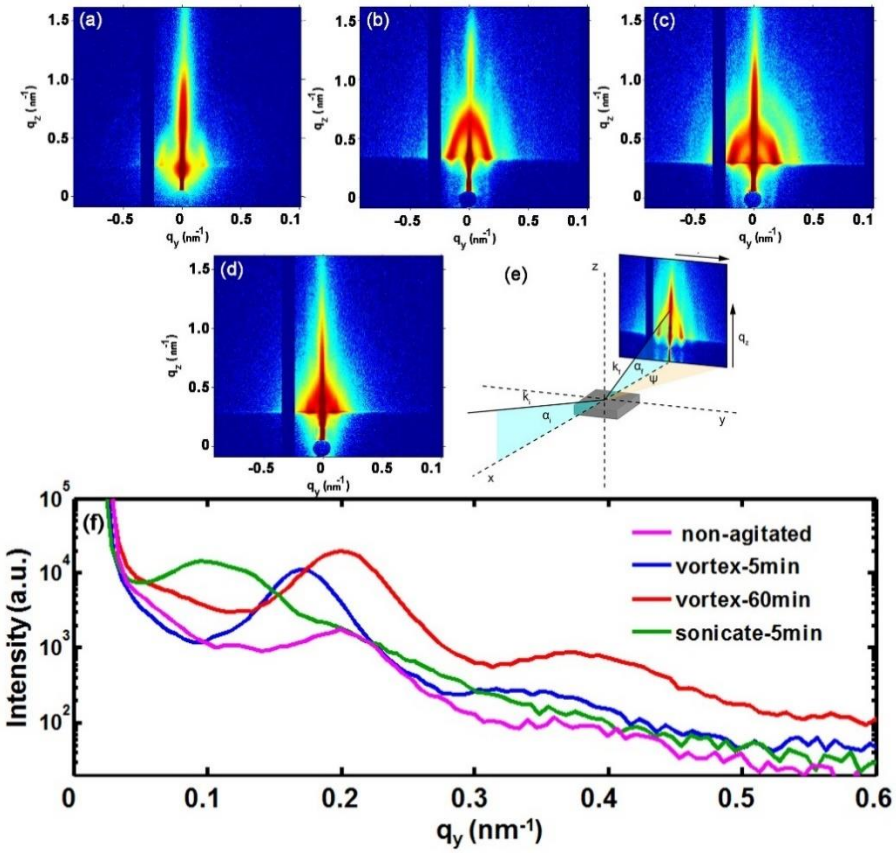

Figure 3.4 GISAXS measurements of PEO-*b*-PHA/Nb_2O_5 thin films at an incidence angle of α_i= 0.22^o for samples non-agitated (a) vortex-5min (b), vortex-6min (c), sonicate-5min (d). A schematic of the sample measurement geometry (e). In-plane line cuts of scattering intensity were compared for each sample (f). All color scales correspond to the log of the X-ray intensity.

Following this model, higher sonication powers are expected to produce surface area faster and thus promote further chain exchange. We note that these results are also consistent with the formation of a new micelle size distribution as a result of kinetic-limited processes during rapid surface collapse. In both cases, the extent of surface turnover decreases the fraction of the starting micelle size distribution and increases the relative

amount of the new population. Regardless, the use of sonication enables rapid modification of nominal micelle size.

Table 3.1 Quantitative measurements of samples by SEM and GISAXS.

Sample Name	SEM Measurements		GISAXS Measurements
	Average Pore Diameter (nm)*	Standard Deviation (nm)	First Peak Position q_y (nm^{-1})
Non-agitated	23.2±0.2	4.0	0.200
Vortex-5min	24.1 ± 0.2	3.4	0.171
Vortex-60min	25.8 ± 0.2	3.5	0.200
Sonicate-5min	28.0± 0.3	4.9	0.103

*Mean ± Error of the Mean

Grazing-incidence small-angle X-ray scattering (GISAXS) was used as an ensemble measurement to further quantify changes to film morphologies. Line cuts of in-plane scattering intensity were extracted from each 2D image to quantify in-plane periodicity (Figure 3.4f). Compared to sample non-agitated, both sample sonicate-5min and vortex-5min exhibited first peaks shifted to lower-q, monotonically corresponding to the increase in feature sizes observed by SEM (Table 1). The 2D data were similar for both vortexed samples and indicated significant long-range order with multiple in-plane correlations as well as out-of-plane correlations (Figure 3.4 b-c). In contrast, the 2D data from samples non-agitated and sonicate-5min predominantly exhibited in-plane correlations (Figure 3.4a, d). The decreased long-range order for samples non-agitated and sonicate-5min may be due to the larger relative micelle size distributions (σ/μ) that inhibit the packing of highly ordered lattices. We note that sample vortex-60min curiously exhibited a decreased apparent lattice constant by GISAXS and an increased pore size by

SEM. This unexpected lattice contraction with larger micelle populations may be associated with the varying relative standard deviation changing the resulting packing density. For all samples, the strong in-plane scattering observed by GISAXS indicates changes to well-defined morphologies.

The inorganic crystal structure and crystallite sizes were examined by wide-angle diffraction after calcination (Figure B.1). The observed reflections were consistent with orthorhombic Nb_2O_5 (PDF no. 27-1003) with a nominal grain size of 12-15 nm (Table B.1). The demonstrated micelle tuning is generalizable to different inorganic systems since the micelle size tuning is performed before the addition of inorganic. The micelle templating of WO_3 after AICE demonstrated the control of multiple inorganic materials (Figure B.4).

3.5 Conclusions

To the best of our knowledge, this is the first example of ultrasonic cavitation promoting the rapid growth of block copolymer micelles under high-χN solution conditions. The results here demonstrate rapid micelle growth by sonication under kinetically challenging high-χN solution conditions. In the absence of agitation, such persistent micelles offer numerous benefits where a desired micelle size may be tuned first with AICE and then maintained constant despite changing solution conditions. Compared to vortexing, the rapid micelle growth with sonication was attributed to an enhancement of the solution-air interface turn-over rate. These findings demonstrate more than an order of magnitude faster micelle growth by sonication as compared to vortexing alone.

3.6 References

(1) Blanazs, A.; Armes, S. P.; Ryan, A. J. *Macromol. Rapid Commun.* **2009**, *30*, 267.

(2) Kelley, E. G.; Albert, J. N. L.; Sullivan, M. O.; Epps, I. I. I. T. H. *Chem. Soc. Rev.* **2013**, *42*, 7057.

(3) Alexandridis, P.; Lindman, B. *Amphiphilic block copolymers: self-assembly and applications*; Elsevier, 2000.

(4) Peters, K.; Lokupitiya, H. N.; Sarauli, D.; Labs, M.; Pribil, M.; Rathouský, J.; Kuhn, A.; Leister, D.; Stefik, M.; Fattakhova-Rohlfing, D. *Adv. Funct. Mater.* **2016**.

(5) Wang, S.; Tangvijitsakul, P.; Qiang, Z.; Bhaway, S. M.; Lin, K.; Cavicchi, K. A.; Soucek, M. D.; Vogt, B. D. *Langmuir* **2016**, *32*, 4077.

(6) Patterson, J. P.; Cotanda, P.; Kelley, E. G.; Moughton, A. O.; Lu, A.; Epps III, T. H.; O'Reilly, R. K. *Polym. Chem.* **2013**, *4*, 2033.

(7) Rauda, I. E.; Buonsanti, R.; Saldarriaga-Lopez, L. C.; Benjauthrit, K.; Schelhas, L. T.; Stefik, M.; Augustyn, V.; Ko, J.; Dunn, B.; Wiesner, U.; Milliron, D. J.; Tolbert, S. H. *ACS Nano* **2012**, *6*, 6386.

(8) Jiang, B.; Li, C.; Tang, J.; Takei, T.; Kim, J. H.; Ide, Y.; Henzie, J.; Tominaka, S.; Yamauchi, Y. *Angew. Chem., Int. Ed.* **2016**, *55*, 10037.

(9) Tang, J.; Liu, J.; Li, C.; Li, Y.; Tade, M. O.; Dai, S.; Yamauchi, Y. *Angew. Chem., Int. Ed.* **2015**, *54*, 588.

(10) Bastakoti, B. P.; Li, Y.; Kimura, T.; Yamauchi, Y. *Small* **2015**, *11*, 1992.

(11) Maysinger, D.; Lovrić, J.; Eisenberg, A.; Savić, R. *Eur. J. Pharm. Biopharm.* **2007**, *65*, 270.

(12) Kabanov, A. V.; Batrakova, E. V.; Alakhov, V. Y. *J. Controlled Release* **2002**, *82*, 189.

(13) Kakizawa, Y.; Kataoka, K. *Adv. Drug Delivery Rev.* **2002**, *54*, 203.

(14) Kataoka, K.; Harada, A.; Nagasaki, Y. *Adv. Drug Delivery Rev.* **2001**, *47*, 113.

(15) Cabral, H.; Matsumoto, Y.; Mizuno, K.; Chen, Q.; Murakami, M.; Kimura, M.; Terada, Y.; Kano, M.; Miyazono, K.; Uesaka, M. *Nat. Nanotechnol.* **2011**, *6*, 815.

(16) Lokupitiya, H. N.; Jones, A.; Reid, B.; Guldin, S.; Stefik, M. *Chem. Mater.* **2016**, *28*, 1653.

(17) Hayward, R. C.; Pochan, D. J. *Macromolecules* **2010**, *43*, 3577.

(18) Denkova, A. G.; Mendes, E.; Coppens, M.-O. *Soft Matter* **2010**, *6*, 2351.

(19) Rharbi, Y.; Li, M.; Winnik, M. A.; Hahn, K. G. *J. Am. Chem. Soc.* **2000**, *122*, 6242.

(20) Halperin, A.; Alexander, S. *Macromolecules* **1989**, *22*, 2403.

(21) Lu, J.; Bates, F. S.; Lodge, T. P. *Macromolecules* **2015**, *48*, 2667.

(22) Lu, J.; Bates, F.; Lodge, T. *ACS Macro Lett.* **2013**, *2*, 451.

(23) Lu, J.; Bates, F.; Lodge, T. *Macromolecules* **2016**, *49*, 1405.

(24) Choi, S.-H.; Lodge, T. P.; Bates, F. S. *Phys. Rev. Lett.* **2010**, *104*, 047802.

(25) Won, Y.-Y.; Davis, H. T.; Bates, F. S. *Macromolecules* **2003**, *36*, 953.

(26) Kelley, E. G.; Murphy, R. P.; Seppala, J. E.; Smart, T. P.; Hann, S. D.; Sullivan, M. O.; Epps, T. H. *Nat. Commun.* **2014**, *5*.

(27) Murphy, R. P.; Kelley, E. G.; Rogers, S. A.; Sullivan, M. O.; Epps III, T. H. *ACS Macro Lett.* **2014**, *3*, 1106.

(28) Aniansson, E. G.; Wall, S. *The J. Phys. Chem.* **1975**, *79*, 857.

(29) Suslick, K. S. *Sci. Am.* **1989**, *260*, 80.

(30) Suslick, K. S.; Flannigan, D. J. *Annu. Rev. Phys. Chem.* **2008**, *59*, 659.

(31) Suslick, K. S. *Kirk-othmer encyclopedia of chemical technology* **1998**.

(32) M. Webster, (Producer), A. McEwen, (Producer). May 09, 2016. *Bigger Than Bacon*

[Audio podcast] Retrieved from http://www.radiolab.org/story/bigger-bacon/.

(33) Ma, Y.; Lodge, T. P. *Macromolecules* **2016**.

(34) Choi, S.-H.; Bates, F. S.; Lodge, T. P. *Macromolecules* **2014**, *47*, 7978.

(35) Guerrero-Sanchez, C.; Wouters, D.; Fustin, C.-A.; Gohy, J.-F.; Lohmeijer, B. G. G.; Schubert, U. S. *Macromolecules* **2005**, *38*, 10185.

(36) Mai, Y.; Eisenberg, A. *Chem. Soc. Rev.* **2012**, *41*, 5969.

(37) Esselink, F.; Dormidontova, E.; Hadziioannou, G. *Macromolecules* **1998**, *31*, 4873.

(38) Kelley, E. G.; Smart, T. P.; Jackson, A. J.; Sullivan, M. O.; Epps, T. H. *Soft Matter* **2011**, *7*, 7094.

(39) Lund, R.; Willner, L.; Richter, D. In *Adv. Polym. Sci.* **2013**, *259*, 51-158.

CHAPTER 4

ELECTROCHEMICAL CHARGE STORAGE PERFORMANCE OF MACROPOROUS *T*-NB_2O_5 DERIVED FROM PERSISTENT MICELLAR TEMPLATING.

4.1 Abstract

Thorough understanding on the operative mechanism of energy storage systems provides vital knowledge about ion storage and transport mechanisms that determine the device performance. Recently, much research has been done to understand the fundamentals of electrochemical energy storage mechanism of niobia which is a well-known intrinsic pseudocapacitive material. Niobia shows capacitive charge storage characteristics for a wide range of particle sizes and morphologies. However, a systematic study has not been done to address the major factors that govern in pseudocapacitive charge storage behavior in *T*-Nb_2O_5. The charge storage behaviour of *T*-Nb_2O_5 is governed by (1) ion transportation through the electrolyte-pore system, (2) Li^+ intercalation through solid oxide matrix and (3) the transportation of electrons through solid oxide. Careful investigation of these parameters requires appropriate model systems. In this study, Li^+ diffusion limits inside the *T*-Nb_2O_5 have been systematically studied using tunable isomorphic metal oxide architectures derived from persistent micelle templating (PMT) that has constant diameter pores but different wall thicknesses. The Li^+ intercalation in the length scale of about 12-22 nm was studied using the power law analysis to understand the length dependence of charge storage mechanism in *T*-Nb_2O_5. The results showed an early transition of capacitive charge storage to diffusion limited charge storage for porous films with thickener walls compared to thinner walled films. This demonstrates the unique capability of PMT derived isomorphic architectures as model systems to identify the optimal length scales for future generation nano-optimized charge storage and conversion devices.

4.2 Introduction

Pseudocapacitive behavior is a fairly new phenomenon that is observed in many transition metal oxides and has gained much attention due to its ability to combine high energy density and high power density into one material.[1] Pseudocapacitance arises from the reversible redox reactions that occur at or near the surface of an electrode material and these reactions are not limited by solid-state ion diffusion.[1, 2] Also, these reactions are very fast and occur on the order of seconds and minutes making them really interesting materials in electric vehicles, fast charging portable electronics and grid storage applications.[1-3] Transition metal oxides such as RuO_2, MnO_2, V_2O_5 and orthorhombic niobia (*T*-Nb_2O_5) have been identified as pseudocapacitive materials.[1] The electrochemical energy storage capability of Nb_2O_5 has been known for decades[4] but the excellent pseudocapacitive behaviour of *T*-Nb_2O_5 has been identified recently.[2, 5, 6]

Out of many crystalline phases of niobia, *T*-Nb_2O_5 has been identified as the best pseudocapacitive material by Dunn and *et.al*.[2, 5-7] According to their studies, *T*-Nb_2O_5 shows intercalation pseudocapacitance by the insertion of Li^+ into nanocrystal films of *T*-Nb_2O_5 through two-dimensional transport pathways in crystalline network without significant volume expansion.[2] This understanding of Li^+ intercalation helps to explain fast charge storage behavior of *T*-Nb_2O_5 that results due to the absence of limitations from solid-state ion diffusion. Moreover, theoretical study by Ganesh *et.al*. concluded that the high rate performance in Nb_2O_5 is due to the effective charge transfer through open channels between NbO_x sheets that reduce the energy barrier.[8] Even though, charge storage of Nb_2O_5 is not limited by semi-infinite diffusion, it displayed large charge transfer resistance during ion insertion probably due to its low conductivity (~ 10^{-6} S/cm).[9, 10]

In literature, many ways of assembling of niobium pentoxide have been reported for the aspect of studying its charge storage behavior. To overcome the large charge transfer resistance due to low conductivity, many studies were performed by combining carbon with the Nb_2O_5 to improve the conductivity during the nanostructure fabrication process. Fabrication of Nb_2O_5/graphene,[11] Nb_2O_5/CNT,[12] Nb_2O_5/carbon/niobium carbide,[7] holey-graphene/Nb_2O_5[13] and Nb_2O_5/carbon core-shell[14, 15] composites usually required multiple synthesis steps and yielded relatively small energy densities due to the dead mass introduced by the conductive material.

Another way to fabricate nanostructured Nb_2O_5 is to use block copolymers as templates. This method provides many advantages such as less number of synthesis and processing steps, ability to incorporate carbon residues by simply changing the calcination conditions and the flexibility of tuning the nanoscale properties such as pore diameter and material wall thickness with high degree of predictability. Brezesinski *et. al* fabricated highly ordered mesoporous *T*-Nb_2O_5 thin films with iso-oriented layered nanocrystalline domains by coassembly of inorganic sol-gel reagents with a poly(ethylene-co-butylene)-*b*-poly(ethylene oxide) diblock copolymer.[5] According to their study, these films showed high levels of pseudocapacitive charge storage and much higher capacities than mesoporous amorphous films due to the high surface area of Nb_2O_5 that arise from nanoscale porosity, the iso-orientation of the layered nanocrystalline pore walls, and the mechanical flexibility of periodic porous material.[5] Jinwoo Lee *et. al* fabricated mesoporous Nb_2O_5/carbon nanocomposite using poly(ethylene oxide-*b*-styrene) as an anode for hybrid supercapacitors.[16] Although these studies demonstrated the ability of block copolymers to fabricate nanostructured Nb_2O_5 via less complicated synthesis and

high charge storage properties, there is no systematic evaluation carried out to investigate the effect on charge storage properties when changing the nanostructured properties such as wall thickness and pore diameter that play major roles in nanostructured device performance.

In this chapter, PMT derived tunable isomorphic nanomaterials were used as model systems to study the charge storage mechanism at different length scales. The PMT is a unique technique which forms kinetically entrapped block copolymer micelles that do not undergo size or morphology change when inorganic materials are introduce into the solvent mixture. This gives the ability to decouple the template diameter from changing material wall-thickness.[17, 18] This degree of wall thickness tunability paves the path to fabricate tunable nanostructured model systems to study the chare storage properties at different length scales. Moreover macroporous (> 50 nm) materials were targeted and synthesized with the hope of using these optimized architectures for future generation 3D batteries.

4.3 Experimental Section

Synthesis of mesoporous Nb_2O_5 having different wall thicknesses

Synthesis of the mesoporous Nb_2O_5 via evaporation induced self-assembly is discussed in greater detail elsewhere.[17] Briefly, 50 mg of PEO-*b*-PHA (PEO = 20,000 g/mol, PHA = 95,000 g/mol) block copolymer was dissolved in anhydrous inhibitor-free THF and 37% w/w HCl was added very slowly to the polymer solution followed by 5 min vortexing. Then, different volumes of niobium ethoxide were added to achieve respective M:T ratios (1.2, 1.8, 2.4 and 3.0). Films were made on Si wafer filmetric studies and on FTO to study the electrochemical charge storage behavior.

Electrode preparation and electrochemical characterization of mesoporous Nb_2O_5

For electrochemical studies, films were spin coated on FTO glass substrates. Prior deposition, 3 cm x 3 cm substrates washed with soap, sonicated for 30 min in ethanol and dried under air. Then the substrates were plasma cleaned for 15 min before spin coating. Spin coating was carried out under different spin rates for different M:T ratios as shown in Table C.3 After spin coating, edges of the substrates were cut off to eliminate the edge effect. The resultant dimensions of the substrates were 2 cm x 1 cm with a 1 cm x 1 cm niobia coverage and 1 cmx 1cm electrical contact area. The humidity inside the chamber was maintained below 23% during the spin coating. The as-made films were aged at 70 ^{o}C for 2 h and then at 100 ^{o}C for overnight. The films were calcined at 600 ^{o}C for 1 min under air inside a tube furnace before using them as working electrodes.

The charge storage properties were investigated with 3-electrode cells using lithium pieces as the counter and reference electrodes as shown in Figure C.1. A solution of 1 *M* $LiClO_4$ in propylene carbonate was used as the electrolyte. Before making the electrolyte, $LiClO_4$ was dried under vacuum for overnight at 180 ^{0}C and the propylene carbonate was dried with 50% w/w 3Å molecular seives.[19] Before the CV measurements, the electrodes were held at 1.2 V for 2 h and cycled at 10 mV/s for 20 cycles to remove any residual adsorbed water as the pre-cleaning steps for every film. Then the CV was performed with varying sweep rates from 0.2 to 300 mVs^{-1} in the range of 1.2 to 3.0 V vs (Li/Li^{+}) to investigate the capacitive behaviour of Nb_2O_5 mesoporous thin films. In each sweep rate, the experiement was repeated for twice and the 2nd cycle was used for the analysis. Three trials were conducted for each M:T ratio and averaged current values were used for further studies. All the tests were performed in an argon filled glove box with oxygen and water levels of less that 1ppm.

GIWAXS

The scattering experiments were conducted using a SAXSLab Ganesha at the South Carolina SAXS Collaborative. Further information about the instrumental setup is discussed in great details elsewhere.[17] GIWAXS was conducted with an incident angle of 8° to minimize the data smearing and sample-to-detector distance was kept at 104.5 mm. The instrumental broadening factor was measured using NIST reference material 640c. This broadening was considered when fitting the observed niobia peak as a Gaussian with a Gaussian point spread function arising from the measured instrumental broadening factor for the grain size calculation via Scherer analysis.

4.4 Results and Discussion

Constant film thickness for each M:T ratio with spin coating

Fabrication of thin films with different M:T ratios was achieved by introducing different volumes of niobium ethoxide into the micelle solution which resulted in a series of solutions with various densities and viscosities. These variations resulted in different total film thicknesses for each M:T ratio when spun at same spin rate. Construction of thin films with similar total film thickness is important because the total film thickness of active material determines the electrons diffusion length inside the film during the charge storage process. To avoid the complexity that could be introduced due to different electron diffusion lengths among the samples, the total thickness for all the films derived from different M:T ratios was kept approximately the same by controlling the spin rate. The exact thickness of a film fabricated by spin coating depends on the material concentration and solvent evaporation rate. The solvent evaporation rate is highly influenced by the viscosity of the solvent, humidity, vapor pressure and the temperature. For this reason, spin

thickness curves for three different M:T ratios were determined experimentally to construct a calibration curve to obtain a relationship between M:T ratio and the spin rate. A series of thin films were made on Si wafer at different spin rates (750, 1000, 1500, 2000 and 3000 rpm) for each M:T (1.2, 2.4 and 3.0) ratios. The total thickness of the films was measured using Filmetrics after calcination (Table C.1). The spin-thickness curves for those M:T ratio were developed and fitted against $t = C\, w^{-m-0.5}$ where t is the total thickness, C is a constant and w is the spin rate (Figure 4.1, a, b, c). The equations for best fits were extracted and tabulated in Table C.2 These best fits were used to calculate spin rates for each M:T ratio to achieve a targeted total thickness (180 nm). A calibration curve for spin rate *vs.* M:T ratio (Figure 2.4.1, d) was constructed to target 180 nm thick films. This calibration curve was used to extract spin rates that correspond to any interested M:T ratio to fabricate 180 nm thick film as shown in Table C.3 The total thickness of resultant films was validated with Filmetrics and the obtained values were fairly in good agreement with the expected total thickness values as tabulated in Table C.3 Using this process thin films with fixed total film thickness were made to keep the same electron diffusion lengths for all the M:T ratios.

PMT is a technique that use high χ block copolymers and suitable solution conditions to deliberately impede micelle equilibration to produce persistent micelles. These micelles can be used as templates to achieve porous materials with different wall thicknesses. In this study, a block copolymer (PEO-*b*-PHA) with a high effective interaction parameter $\chi_{PEO/PHA}$ = 0.34 was used as the template. Tunability of the wall thickness was achieved by adding different amount of inorganic precursor as reported elsewhere.[17] Resultant films were calcined and the pore size and the wall thickness

measurements were calculated from SEM images using ImageJ software as shown in Figure 4.2.

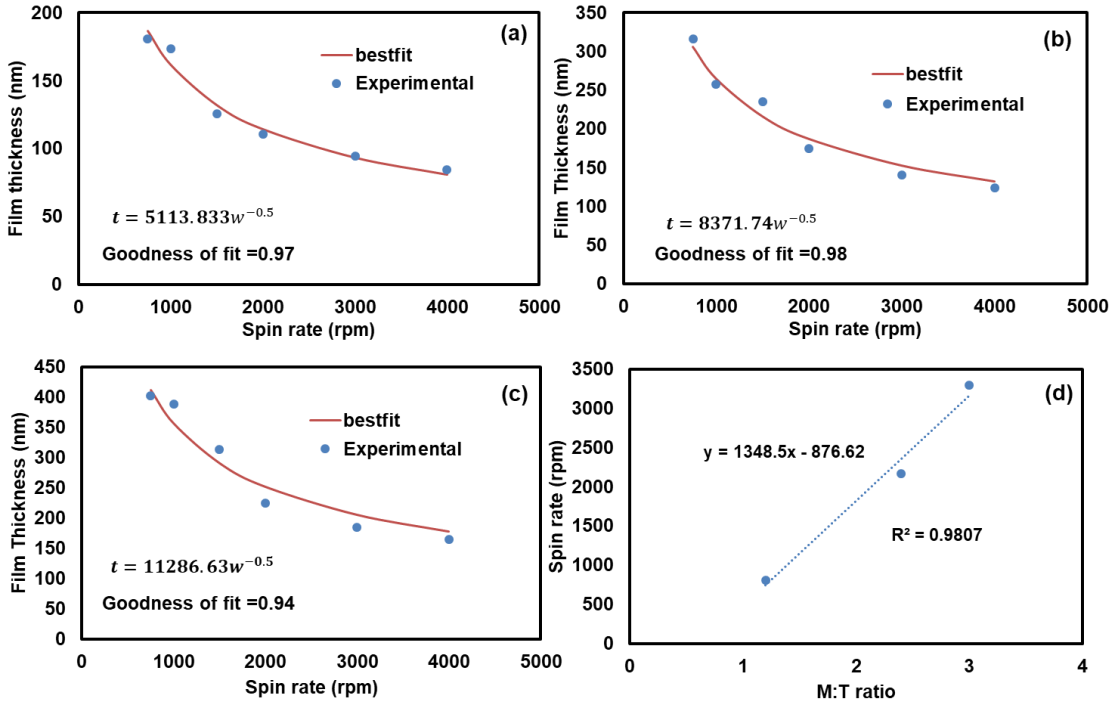

Figure 4.1 Thickness *vs.* spin rate curves for each M:T ratio (a) 1.2, (b) 2.4 and (c) 3.0 were constructed and fitted against $\boldsymbol{t = C\, w^{-m-0.5}}$ where $\boldsymbol{t}$ is total thickness, $\boldsymbol{C}$ is a constant and $\boldsymbol{w}$ is the spin rate. (d) Thickness *vs.* M:T ratio calibration curve constructed to achieve 180 nm thick films.

The pore diameter values obtained for all four M:T ratios were very similar to each other indicating the constant pore diameter of the resultant films as tabulated in Table 4.1. Interestingly the obtained films were macroporous (>50 nm) as we expected even though it is a difficult target to achieve by using conventional block copolymers as templates.[17, 20] The obtained pore wall thickness change from 12.13 nm to 22.44 nm where it gives approximately the twice of the length scale to study the charge storage properties.

Table 4.1 Average pore diameter and wall-thickness of calcined Nb_2O_5 thin films with different M:T ratio.

Sample name	Average pore diameter from SEM (nm)	Average wall thickness from SEM (nm)
M:T-1.2-Nb_2O_5	52.04±1.09	12.13±0.20
M:T-1.8-Nb_2O_5	52.55±0.77	15.22±0.26
M:T-2.4-Nb_2O_5	52.81±0.89	19.40±0.60
M:T-3.0-Nb_2O_5	52.60±0.79	22.44±0.61

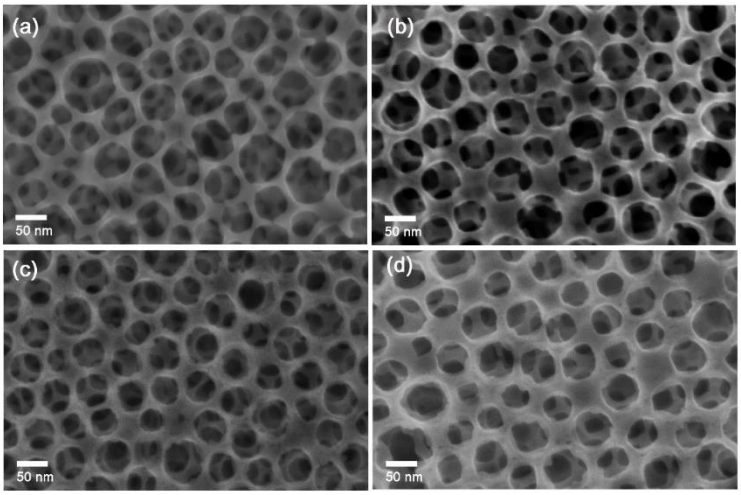

Figure 4.2 SEM images of calcined Nb_2O_5 thin films made on FTO substrate with different M:T ratios (a) 1.2 (b) 1.8 (c) 2.4 and (d) 3.0.

The type of crystallographic structure of the active material have significant effect on capacitive storage behavior as reported for many transition metal oxide systems.[6, 21] Out of many crystalline states orthorhombic Nb_2O_5 possess high specific capacitance at high rates as demonstrated by Dunn *et. al* for Nb_2O_5 nanoparticles.[6] In this study, films were calcined at 600^oC for 1 minute under air to induced the crystallization of Nb_2O_5. This heat treatment

resulted in *T*-Nb_2O_5 for all the samples as confirmed by the appearance of characteristic (2100) diffraction peaks in 1D-WAXS pattern (Figure 4.2 a). The obtained 2D-WAXS data showed interesting anisotropic diffraction patterns for all the M:T ratios as shown in Figure 4.2 b-e. This is an indication of preferred orientation of the nanocrystals relative to the substrate. This same sort of crystallographic orientation was observed by Brezesinski *et. al.* for polymer templated transition metal oxides which was described as "soft epitaxy".[5] The (001) and (180) diffraction rings showed clear brightness variation along the rings in 2D-WAXS pattern. The averaged intensity data for (001) and (180) diffractions rings were plotted against azimuthal angle to further study the variation of crystallographic anisotropy in between different M:T ratios as shown in Figure 4.2 f and g. Scattering intensity data as a function of azimuthal angle could be fitted with a Gaussian curve to calculate the degree of orientation.[22] The obtained results showed some degree of anisotropy and a large degree of isotropic contribution in each M:T ratio. This indicates the porous material is composed with large portion of randomly oriented crystals along with some degree of oriented crystals. The values obtained for degree of orientation from peak (180) increased gradually form 1.24% to 8.90% when increasing the M:T ratio form 1.2 to 3.0. It is very interesting to observe the degree of anisotropy varies with M:T ratio and will need further characterization to understand the distribution of oriented crystals along the pore wall.

The Scherrer analysis was conducted on (001) diffraction peak to obtained the grain size for each sample as shown in Table 4.2. The resulted grain sizes showed monotonic increase with increasing the M:T ratio. The obtained grain sizes are compatible with the walls thicknesses calculated from the SEM images.

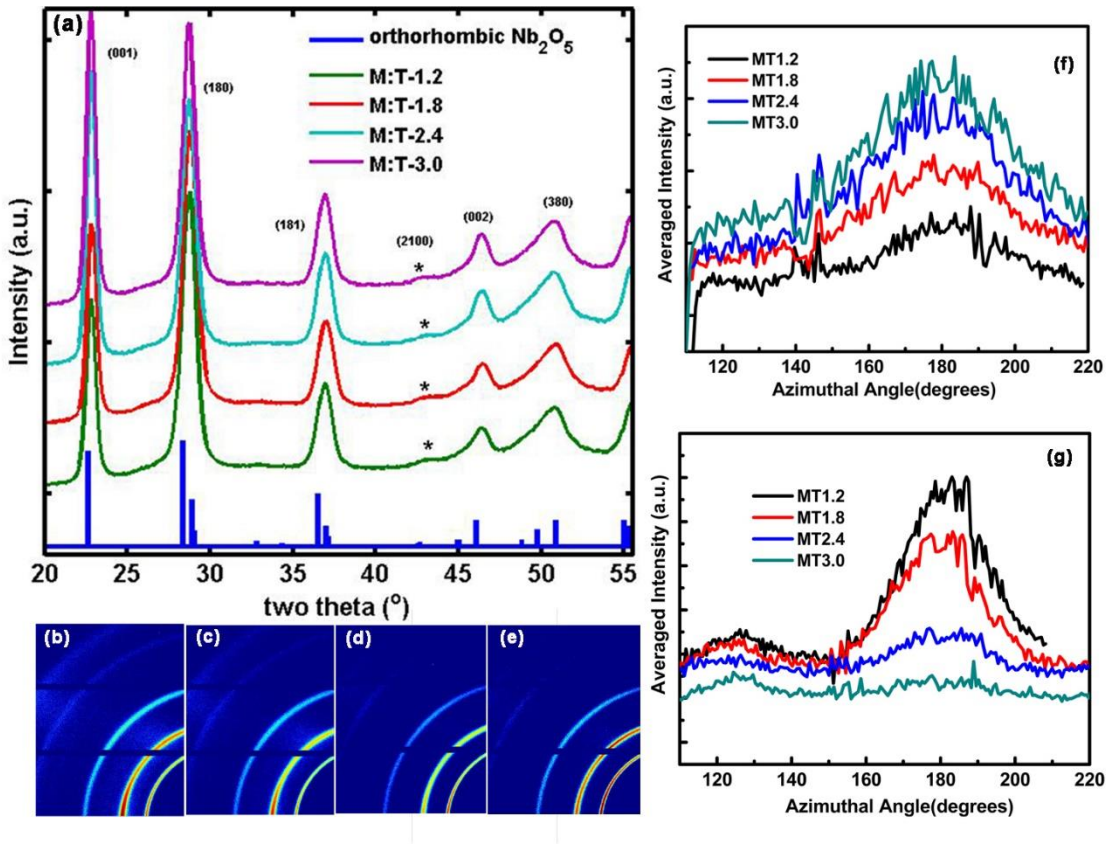

Figure 4.3 GIWAXS was measured for all reported samples after calcination (a). The obtained 1-D WAXS patterns were all consistent with *T*-Nb_2O_5 (PDF #27-1003). The characteristic peaks for *T*-Nb_2O_5 were marked using asterisks. The corresponding 2D-WAXS data for (b) M:T-1.2, (c) M:T-1.8, (d) M:T-2.4 and (e) M:T-3.0 showed anisotropic rings. The 2D color scale corresponds to the log of the X-ray intensity. The averaged intensity *vs.* averaged azimuthal angle plots for (f) (001) and (g) (180) diffractions after smoothed out with adjacent averaging.

The charge storage properties of the resultant films were studied by using a home-made 3-electrode cell using lithium as the counter and the reference electrodes (Figure C.1) With the presence of lithium electrolyte, Nb_2O_5 stores charge through the insertion of lithium ions into solid niobia followed by reduction of Nb^{5+} to Nb^{4+} with

Table 4.2 Nb_2O_5 grain sizes calculated from the (001) peak of *T*-Nb_2O_5 using the Scherer formula.

Sample Name	Grain Size (nm)
MT-1.2	12.2
MT-1.8	12.8
MT-2.4	13.0
MT-3.0	13.1

maximum theoretical capacity of 726 C g^{-1} (when x = 2) as shown in equation 1.[23]

$$Nb_2O_5 + xLi^+ + xe^- \longleftrightarrow Li_xNb_2O_5 \quad (1)$$

To investigate the capacitive properties at different length scales, sweep rates were varied from 0.2 mV s^{-1} to 300 mV s^{-1}. The recorded CV plots are illustrated in Figure 4.4 (a) and all the M:T ratios indicated broad anodic (at 1.8 V *vs* Li/Li^+) and cathodic (at 1.8 and 1.5 V *vs* Li/Li^+) peaks at particularly in low sweep rates. These characteristic redox peaks were visible due to the additional intercalation sites that are accessible in nanostructured materials which have not been observed in bulk films.[24] The intercalation and deintercalation of Li^+ at low sweep rate into *T*-Nb_2O_5 showed high reversibility for all the M:T ratios due to the appearance of cathodic and anodic peaks at the same 1.8 V value at lower sweep rates as shown in Figure 4.4 (a). Also, it is interesting to point out that all the films showed characteristic blue color during lithiation, indicating the well-known electrochromic property of crystalline Nb_2O_5.[24]

The charge storage kinetics for different length scales were analyzed by cyclic voltammetry data collected at various sweep rates according to the power law relationship,

$$i = av^b \quad (2)$$

where the measured current (*i)* varies with the sweep rate (*v*). Both *a* and *b* are adjustable parameters, with *b*-values are determined from the slop of the plot of log(i) *vs* log(sweep rate) as shown in Figure 4.4 (b).[1, 25] When the *b*-value is close to 0.5 indicates the current is controlled by semi-infinite linear diffusion or the current comes primarily from the Li^+ intercalation into solid Nb_2O_5.[25, 26] A *b*-value close to 1 indicates the current is governing by surface-controlled processes which is predominantly capacitive. As shown in Figure 4.4 (b), there are 2 separate regions depending on the *b*-values for entire sweep rate range. Region 1, which is the slow sweep rate range has a *b*-value very close to 1 indicating the current generated at that regime is mainly due to the capacitive storage for all the M:T ratios. In another words, solid state Li^+ diffusion is not the rate-limiting step for charge storage here. The region 2 corresponds to higher sweep rates above 80 mV s^{-1} where the *b*-value is < 0.89 which is an indication of the diffusion controlled charge storage mechanisms for all the length scales. Derivative of the Figure 4.4 (b) graph was plotted to get more insights to the charge storage mechanism for each M:T ratio as shown in Figure 4.4 (c). In that graphs, 3 distinct regions can be clearly identified depending on the change of the *b*-value.

Interestingly, there is a clear change in storage mechanism when increasing the M:T ratios. Higher M:T ratios (M:T-2.4 and M:T-3.0) showed early transition into diffusion-controlled charge storage mechanism (above 80 mV s^{-1}) from capacitive charge storage mechanism where lower M:T ratios (M:T-1.2 and M:T-1.8) showed this transition well above sweep rate 120 mV s^{-1}. This indicates higher M:T ratios experience diffusion limitations at slow sweep rates than the lower M:T ratios. Therefore, porous thin films with

thicker walls tend to show diffusion constraints on Li^+ intercalation rates earlier than the porous thin films with thinner walls.

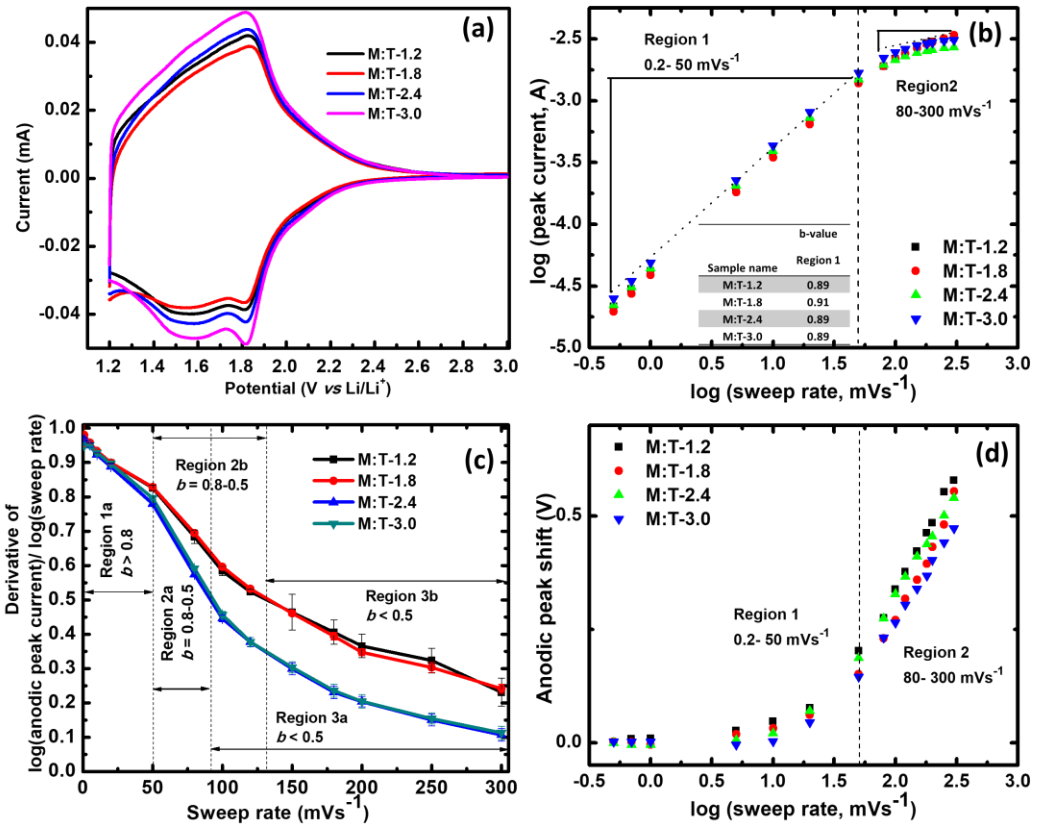

Figure 4.4 (a) CV at 1 mV s^{-1} for all the M:T ratios (b) *b*-value determination for the anodic peak current for the entire sweep rate range 0.2 mV s^{-1} - 300 mV s^{-1} (c) derivative of log(anodic peak current)/log(sweep rate) plot to clearly visualize the *b*-value change through the entire sweep rate range (d) The anodic peak shift with sweep rate.

This interesting finding could be due to the shorter length scale that resulted from lower M:T ratio that tend to intercalate Li^+ faster with short traveling distances while thicker walls showed more material resistance towards Li^+ intercalation into solid niobia. Moreover, region 3 is responsible for very high sweep rates and has *b*-values lower than 0.5. This ambiguous *b*-values could be due to the combination of diffusion limitations and polarization of electrode due to high sweep rates. Specially this effect is prominent at very

higher sweep rate due to the absence of any carbon additives added to increase the electron conductivity. The exact sweep rate where the capacitive- controlled capacity switch to diffusion-controlled capacity could be extracted to each M:T ratio by plotting the obtained capacity values with (sweep rate)$^{-1/2}$. The CV experiments were repeated 3 times with a new film every time to increase the reliability of the data. The obtained capacity values for each trial within a particular M:T ratio showed significant disagreement as shown in Figure C.2. The observed scattered data should be resolved by carefully planned trouble shooting experiments. Possible reason for these disagreements within a batch could be due to the variability of the active mass within a sample due to uneven total thickness across the electroactive area that could arise form spin coating.

The variation of the anodic peak voltage with the sweep rate showed two regions with small peak separation followed by increased separation after 50 mV s^{-1}. This characteristic observation strengthens this system indicating facile intercalation kinetics throughout the entire sweep rate range.

4.5 Conclusions

PMT was presented as a unique technique that enables independent control over wall thickness with constant pore diameter to fabricate model systems in order to study electrochemical energy storage. These PMT derived isomorphic architectures were used to explore Li^+ intercalation kinetics at 12-22 nm length scale. Interestingly, initial studies showed two different charge storage kinetics from power law analysis for thicker *vs* thinner walls demonstrating the ability to systematically study the length dependency of charge storage in nanometer scale. The mass normalization of the resultant capacity values will be conducted in the future with the porosity and accurate thickness data provided by the

ellipsometry porosimetry. Further analysis such as infinite sweep rate capacity is needed to identify the components of capacitive charge storage, diffusion limited charge storage and polarization regime for each length scale to get a better understanding of this system. Also sample preparation step needs more optimizations to deposit films with uniform total thickness across the electroactive area which could eliminate the observed dispersity in capacity values in-between trails.

4.6 References

(1) Augustyn, V.; Simon, P.; Dunn, B. *Energy Environ. Sci.* **2014,** 7, (5), 1597-1614.

(2) Augustyn, V.; Come, J.; Lowe, M. A.; Kim, J. W.; Taberna, P.-L.; Tolbert, S. H.; Abruña, H. D.; Simon, P.; Dunn, B. *Nat Mater* **2013,** 12, (6), 518-522.

(3) Simon, P.; Gogotsi, Y.; Dunn, B. *Science* **2014,** 343, (6176), 1210-1211.

(4) Reichman, B.; Bard, A. J. *J. Electrochem. Soc.* **1981,** 128, (2), 344-346.

(5) Brezesinski, K.; Wang, J.; Haetge, J.; Reitz, C.; Steinmueller, S. O.; Tolbert, S. H.; Smarsly, B. M.; Dunn, B.; Brezesinski, T. *J. Am. Chem. Soc.* **2010,** 132, (20), 6982-6990.

(6) Kim, J. W.; Augustyn, V.; Dunn, B. *Adv. Energy Mater.* **2012,** 2, (1), 141-148.

(7) Zhang, C.; Maloney, R.; Lukatskaya, M. R.; Beidaghi, M.; Dyatkin, B.; Perre, E.; Long, D.; Qiao, W.; Dunn, B.; Gogotsi, Y. *J. Power Sources* **2015,** 274, 121-129.

(8) Lubimtsev, A. A.; Kent, P. R. C.; Sumpter, B. G.; Ganesh, P. *J. Mater. Chem.A* **2013,** 1, (47), 14951-14956.

(9) Viet, A. L.; Reddy, M. V.; Jose, R.; Chowdari, B. V. R.; Ramakrishna, S. *J. Phys. Chem. C* **2010,** 114, (1), 664-671.

(10) Zhang, C.; Beidaghi, M.; Naguib, M.; Lukatskaya, M. R.; Zhao, M.-Q.; Dyatkin, B.; Cook, K. M.; Kim, S. J.; Eng, B.; Xiao, X.; Long, D.; Qiao, W.; Dunn, B.; Gogotsi, Y. *Chem. Mater.* **2016,** 28, (11), 3937-3943.

(11) Kong, L.; Zhang, C.; Zhang, S.; Wang, J.; Cai, R.; Lv, C.; Qiao, W.; Ling, L.; Long, D. *J. Mater. Chem.A* **2014,** 2, (42), 17962-17970.

(12) Wang, X.; Li, G.; Chen, Z.; Augustyn, V.; Ma, X.; Wang, G.; Dunn, B.; Lu, Y. *Adv. Energy Mater.* **2011,** 1, (6), 1089-1093.

(13) Sun, H.; Mei, L.; Liang, J.; Zhao, Z.; Lee, C.; Fei, H.; Ding, M.; Lau, J.; Li, M.; Wang, C.; Xu, X.; Hao, G.; Papandrea, B.; Shakir, I.; Dunn, B.; Huang, Y.; Duan, X. *Science* **2017,** 356, (6338), 599-604.

(14) Kong, L.; Zhang, C.; Wang, J.; Qiao, W.; Ling, L.; Long, D. **2016,** 6, 21177.

(15) Li, G.; Wang, X.; Ma, X. *J. Energy Chem.* **2013,** 22, (3), 357-362.

(16) Lim, E.; Kim, H.; Jo, C.; Chun, J.; Ku, K.; Kim, S.; Lee, H. I.; Nam, I.-S.; Yoon, S.; Kang, K. *ACS Nano* **2014,** 8, (9), 8968-8978.

(17) Lokupitiya, H. N.; Jones, A.; Reid, B.; Guldin, S.; Stefik, M. *Chem. Mater.* **2016,** 28, (6), 1653-1667.

(18) Sarkar, A.; Stefik, M. *J. Mater. Chem.A* **2017,** 5, (23), 11840-11853.

(19) Lindström, H.; Södergren, S.; Solbrand, A.; Rensmo, H.; Hjelm, J.; Hagfeldt, A.; Lindquist, S.-E. *J.Phys. Chem. B* **1997,** 101, (39), 7717-7722.

(20) Peters, K.; Lokupitiya, H. N.; Sarauli, D.; Labs, M.; Pribil, M.; Rathouský, J.; Kuhn, A.; Leister, D.; Stefik, M.; Fattakhova-Rohlfing, D. *Adv. Funct. Mater.* **2016,** 26, (37), 6682-6692.

(21) Ghodbane, O.; Pascal, J.-L.; Favier, F. *ACS Appl. Mater. Interfaces* **2009,** 1, (5), 1130-1139.

(22) Troisi, E. M.; van Drongelen, M.; Caelers, H. J. M.; Portale, G.; Peters, G. W. M. *Eur. Polym. J.* **2016,** 74, 190-208.

(23) Ohzuku, T.; Sawai, K.; Hirai, T. *J. Power Sources* **1987,** 19, (4), 287-299.

(24) Rosario, A. V.; Pereira, E. C. *J. Solid State Electrochem.* **2005,** 9, (10), 665-673.

(25) Wang, J.; Polleux, J.; Lim, J.; Dunn, B. *The Journal of Physical Chemistry C* **2007,** 111, (40), 14925-14931.

(26) Brezesinski, T.; Wang, J.; Polleux, J.; Dunn, B.; Tolbert, S. H. *J. Am. Chem. Soc.* **2009,** 131, (5), 1802-1809.

CHAPTER 5

SUMMARY AND OUTLOOK

In this dissertation work, development of a new nanofabrication tool using kinetically controlled block copolymer micelles is presented in detail and later used to demonstrate its versality in nano-based energy storage device optimization. It is crucial to control the dimensions (wall thickness and pore diameter) of porous nanomaterials when utilizing them in energy storage and energy conversion applications. The major challenge is to achieve independent control over pore and wall dimensions during the fabrication of model systems using block copolymers. This is difficult because the block copolymer templates typically undergo morphological changes during self-assembly to form equilibrated structures making the individual control over pore and wall dimensions of the porous structures hindered. Toward this end, independent control over pore wall thickness was achieved by developing a tool named as persistent micellar templating (PMT) that use kinetically frozen block copolymer micelles. First, PEO-*b*-PHA a new block copolymer system was designed and synthesized. This polymer was designed in a way to have high Flory-Huggins effective interaction parameter between two blocks to increase the thermodynamic barrier to hamper micelles equilibration. These resultant frozen micelles were used as templates by adding an inorganic precursor to form isomorphic architectures with various wall thicknesses. Second, size tuning of kinetically trapped micelles was

demonstrated with ultrasonic cavitation as a rapid and versatile technique to obtained different pore sizes using a single polymer composition. As reported in literature, chain exchange via agitation is limited by the production of solution-air interfaces. In this study, ultrasonic cavitation was used to rapidly equilibrate kinetically trapped polymer micelles. Results showed rapid interface production due to ultrasonic cavitation that facilitated micelle growth by an order of magnitude over vortexing. Resultant micelles with different pore diameters were used as templates to make inorganic porous architectures. To the best of our knowledge, this study is the first example of rapid block copolymer micelle growth under high-χN solution conditions via ultrasonic cavitation. Third, the charge storage behavior of the PMT derived isomorphic architecture was demonstrated with porous *T*-Nb_2O_5. The charge storage mechanism at 12- 22 nm length scale was studied and interestingly two different charge storage kinetics were obtained for initial studies from power law analysis for thicker vs thinner walls as the initial studies. This demonstrated the ability of systematically studying the length dependency of charge storage mechanism at nanometer scale. This independent control over dimensions is a highly useful tool to fabricate model systems when fabricating nano-optimized devices.

As future directions, it can be envisioned that the usage of PMT as a fabricating tool to optimize dimensions in energy storage and conversion devices. This extremely simple technique offers precise and independent control over pore dimensions which helps to derive optimized charge storage properties and rate capabilities at nanometer length. These optimized dimensions could be used to fabricate 3D nanometer scale devices such as 3D supercapacitors and 3D Li^+ micro-batteries.[1,2] This way, optimized anode or cathode could later be used as templates to deposit solid electrolyte and the opposite electrode by

various deposition techniques such as atomic layer deposition (ALD)[3,4] and electrodeposition [5] to complete the entire 3D nano-optimized energy conversion or storage device as shown in Figure 5.1.

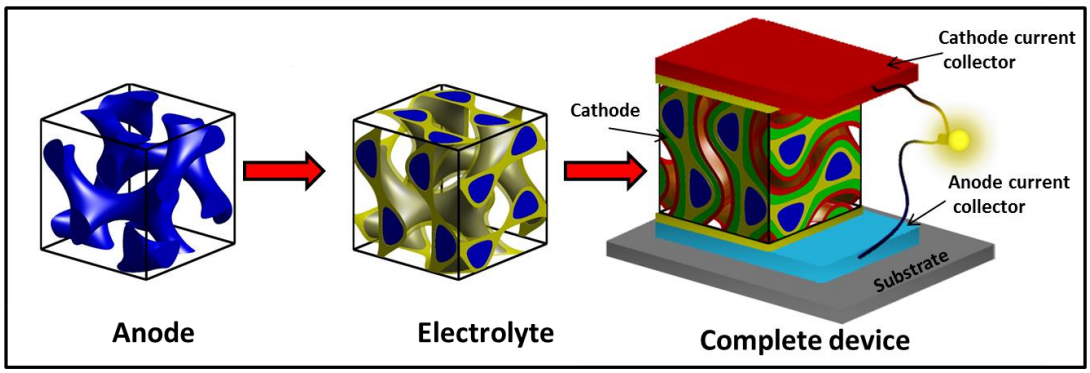

Figure 5.1. Schematic of the process flow for the fabrication of the nano-optimized 3D device

As discussed in Chapter 3, the observed micelle growth with sonication was attributed to an enhancement of the solution-air interface turn-over rate which could be further study with time-resolved small angle neutron scattering to understand the chain exchange mechanism. As discussed in Chapter 4, films resulted from different M:T ratios showed an interesting change in degree of orientation of the crystals within the same crystallographic phase. This will serve as an interesting system to study the effect of crystal orientation on Li^+ intercalation into *T*-Nb_2O_5.

5.1 References

(1) Liu, J.; Banis, M. N.; Li, X.; Lushington, A.; Cai, M.; Li, R.; Sham, T.-K.; Sun, X. *J. Phys. Chem. C* **2013**, *117*, 20260.

(2) Perng, Y.-C.; Cho, J.; Sun, S. Y.; Membreno, D.; Cirigliano, N.; Dunn, B.; Chang, J. P. *J. Mater. Chem.A* **2014**, *2*, 9566.

(3) Meng, X.; Yang, X.-Q.; Sun, X. *Adv. Mater.* **2012**, *24*, 3589.

(4) S. M. George. *Chemical Review*, 110(1):111–131, 2010

(5) J. W. Long, B. Dunn, D. R. Rolison, and H. S. White. *Chemical Reviews*, 104(10):4463–4492, 2004.

APPENDIX A – CHAPTER 2 SUPPORTING INFORMATION

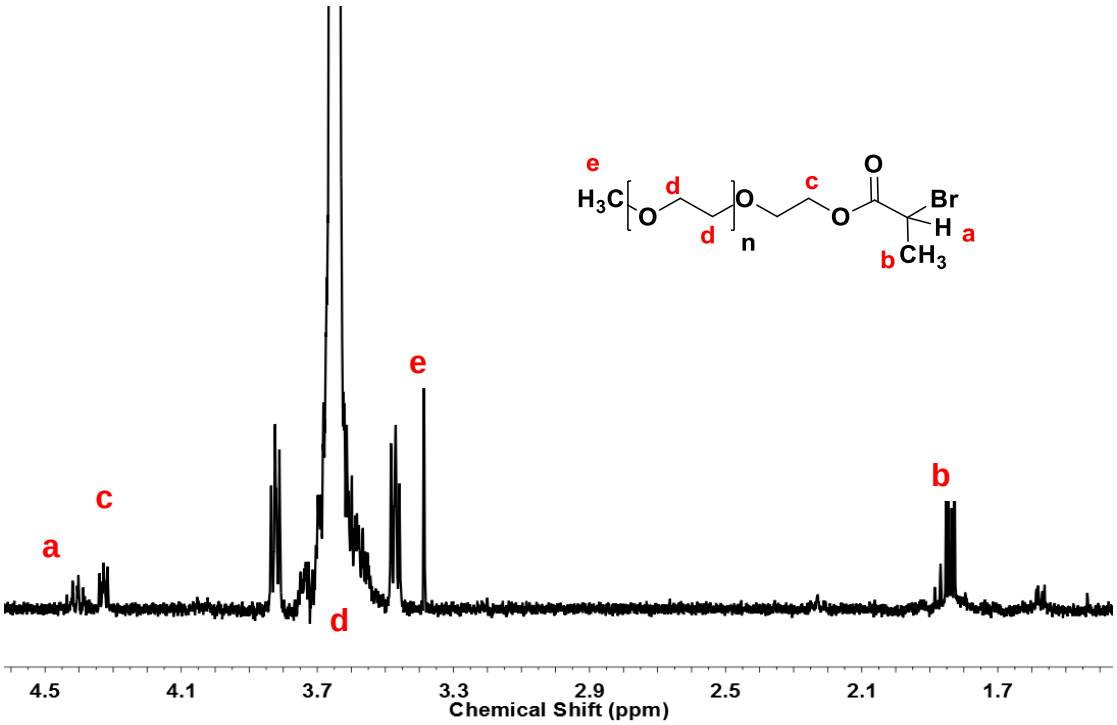

Figure A.1 ^{1}H NMR for PEO(20k)-Br macroinitiator. The quantitative esterification reaction of the hydroxyl group of the poly(ethylene glycol)methyl ether was confirmed by comparing peak **d** to **a**, **b**, and **c**.

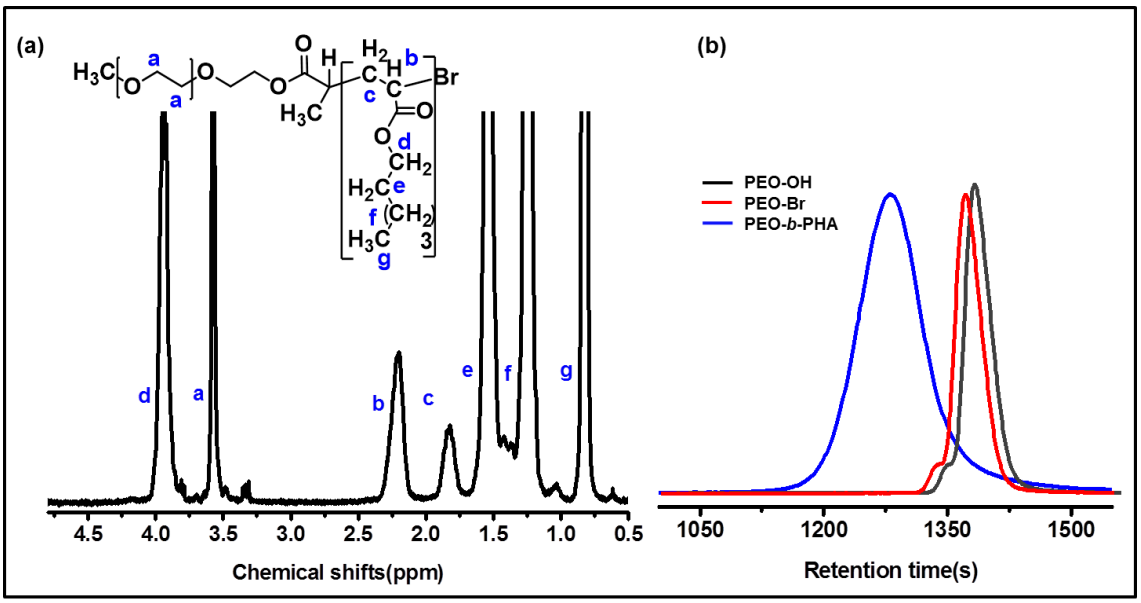

Figure A.2 Controlled growth of PEO-*b*-PHA as confirmed using (a) ^{1}H NMR to calculate block ratios. The multiplet at 1.8 ppm was assigned to protons labeled as **c** in the structure which showed only 25% from the expected integration. However due to tacticity, there are multiple resonances (4) between 1.2-1.9 ppm. These can be seen with both the ^{1}H-^{1}H COSY (S3) and ^{1}H ^{13}C HSQC (S4) spectra. These resonances are mostly overlapped with **e** and **f** in the ^{1}H NMR and are included in the total area calculation used to calculate the molar mass of PHA. (b) GPC traces to check the molar mass dispersity at each synthesis step.

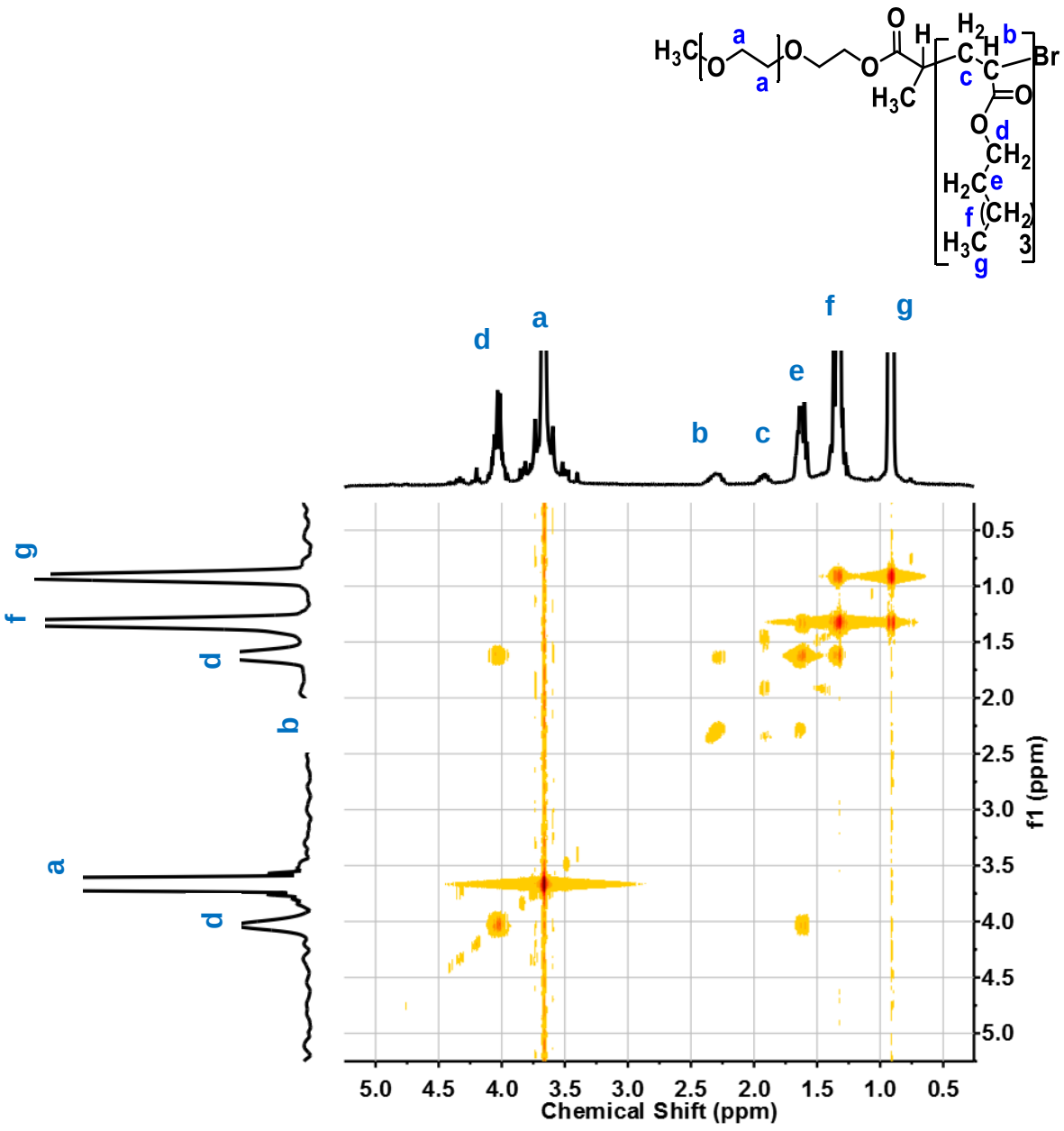

Figure A.3 ^{1}H-^{1}H correlation spectroscopy (COSY).

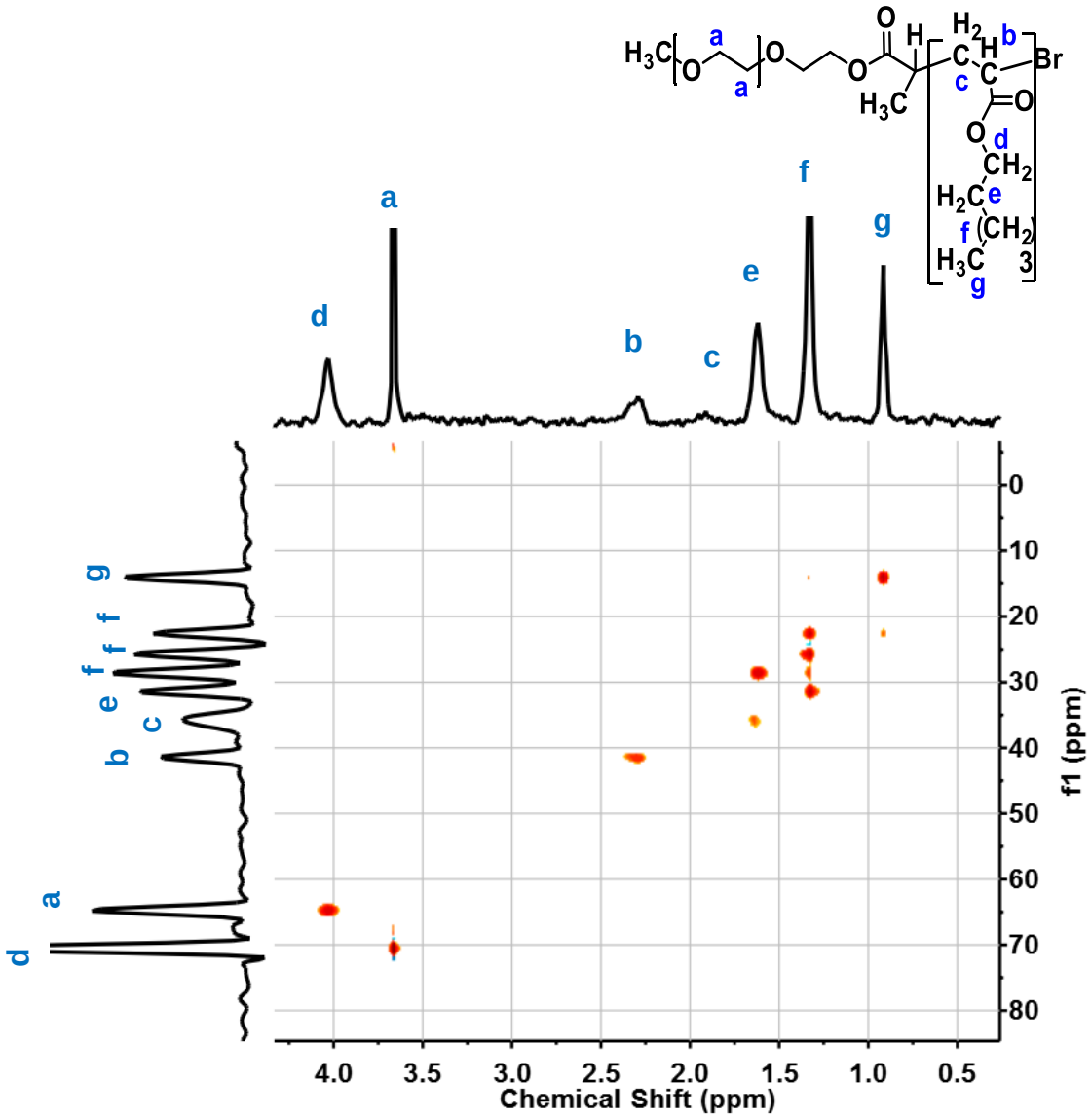

Figure A.4 ^{1}H ^{13}Cheteronuclear single quantum coherence.

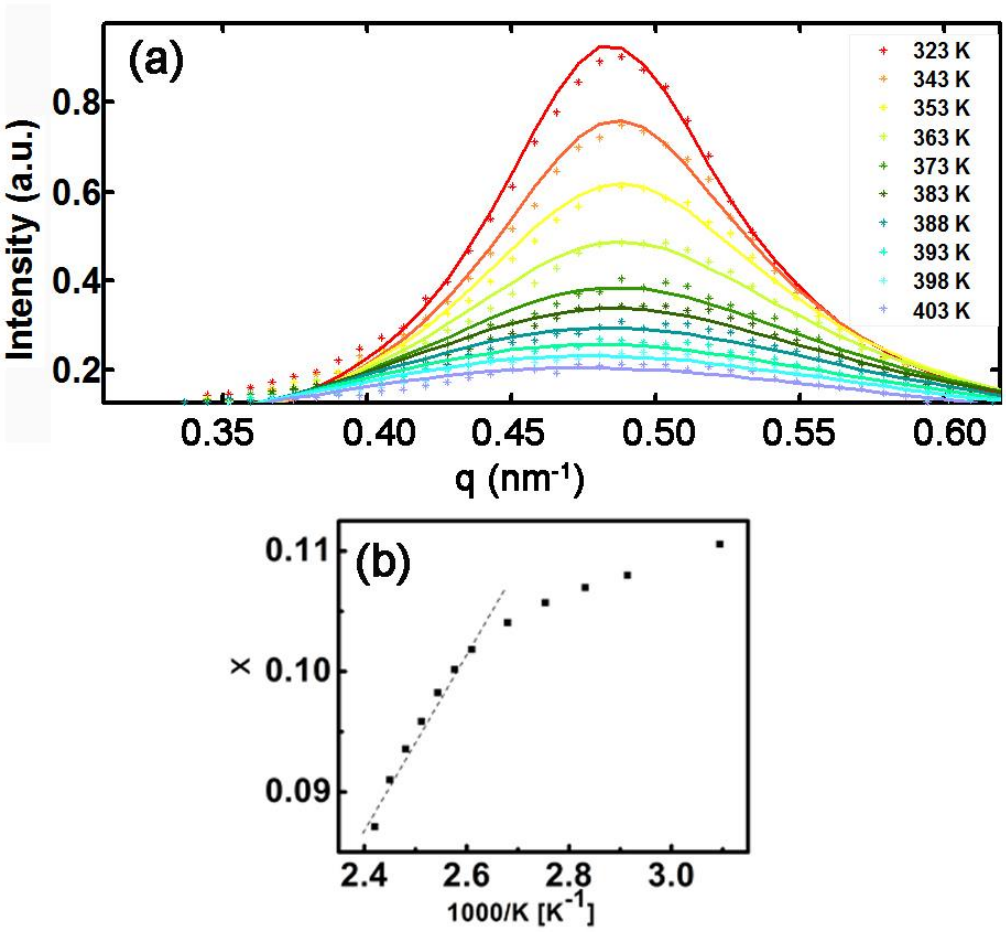

Figure A.5 The SAXS profiles for the **P6** polymer taken in the disordered melt at different temperatures. The solid lines are best-fits to experimental data (*) using the random phase approximation at each temperature. (a) The temperature dependence of the interaction parameter was extracted from the fits. The temperature dependence of χ was found to fit $\chi = 81.7/T - 0.1097$ for **P6** (b).

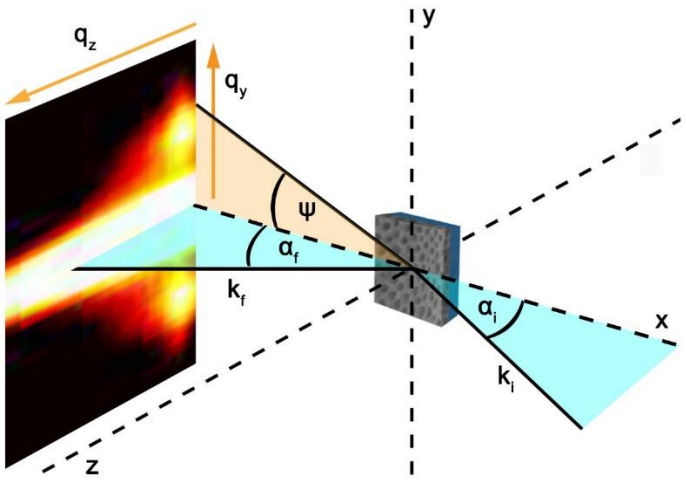

Figure A.6 Sketch of the scattering geometry used in GISAXS and GIWAXS. The sample surface was tilted with respect to the incident beam by an incident angle α_i. The exit angle is denoted as α_f and the in-plane angle is Ψ.

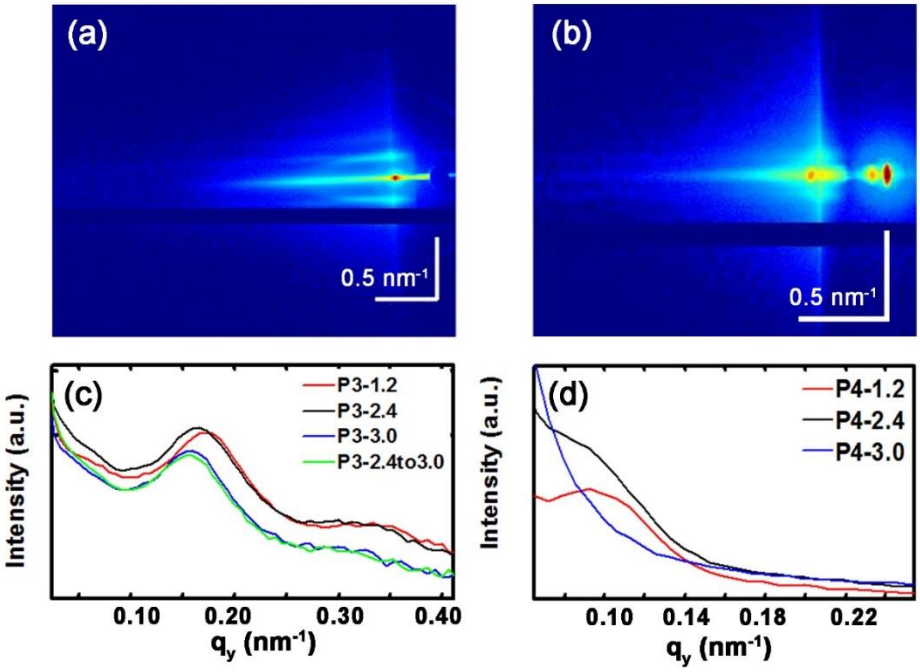

Figure A.7 2D GISAXS measurements after calcination and at an incidence angle of α_i = 0.22º for **P3-1.2-Nb_2O_5** (a) and as-made **P4-1.2-Nb_2O_5** (b). The in-plane cuts of the scattered intensity as a function of *qy* (at constant *qz*) were extracted from the 2D images by integrating over a stripe of 10 pixels along the sample plane *qy* **P3** (c) and **P4** (d). a) and b) color scales correspond to the log of the X-ray intensity.

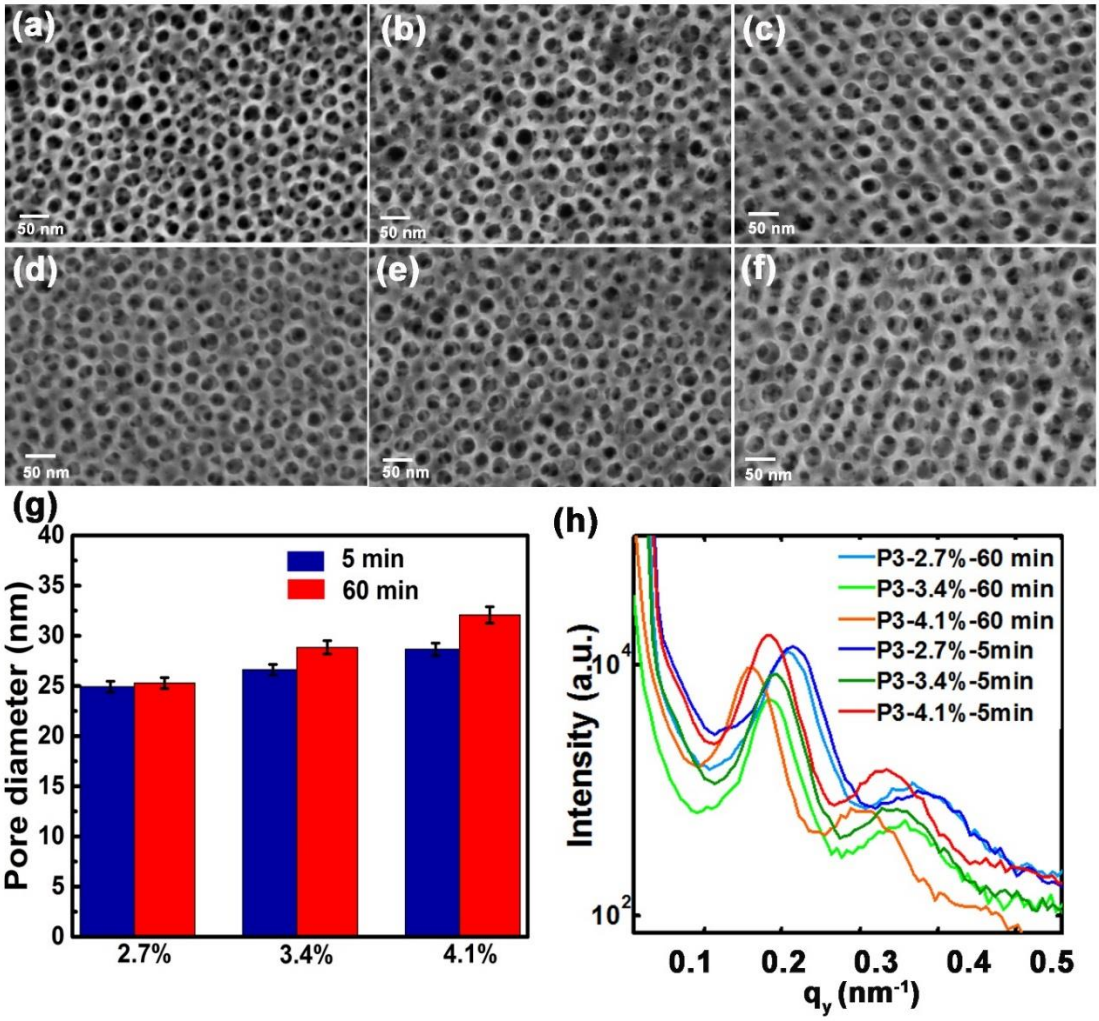

Figure A.8 SEM images of calcined samples with **P3** and I:O=1.2 resulting from different final water content (a),(d) 2.7% (b),(e) 3.4% (c),(f) 4.1% and with different vortexing time (a-c) 5 min and (d-f) 60 min. The average pore diameters are shown for each sample (g). The in-plane cuts of the scattered intensity as a function of *qy* (at constant *qz*) were extracted from the 2D images along the sample plane *qy* (h) and GISAXS data measured at an incidence angle of $\alpha_i = 0.30^o$

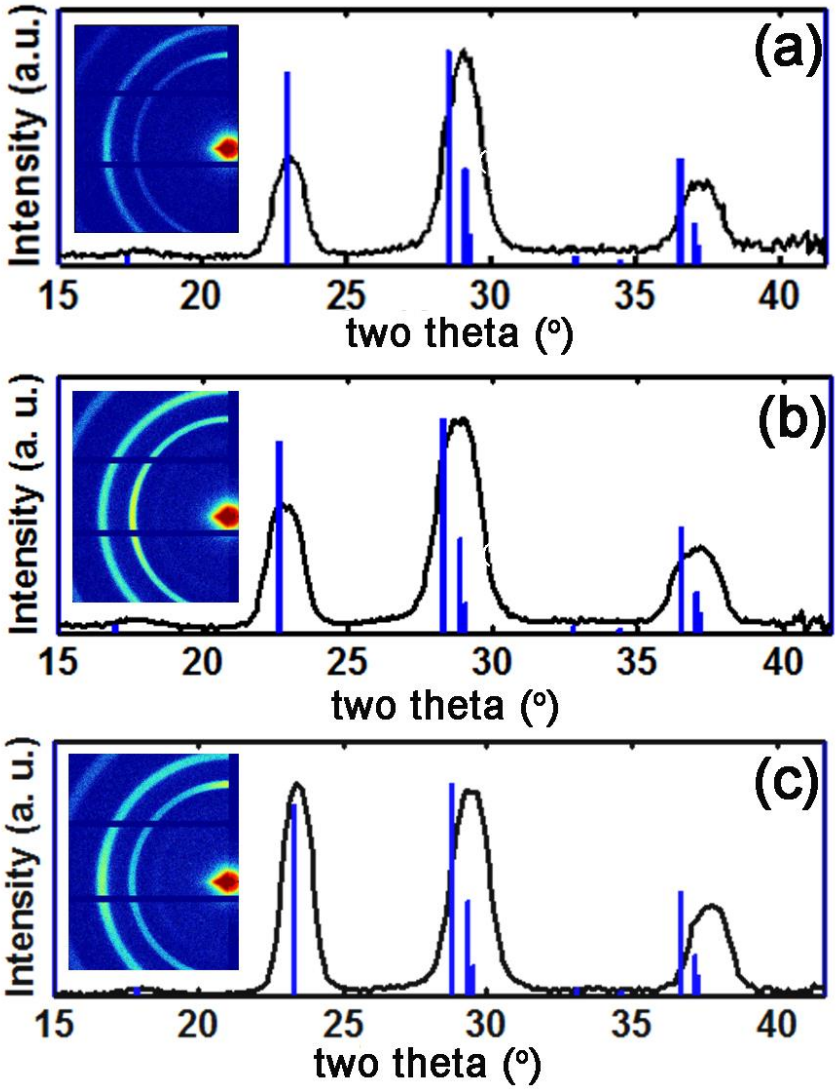

Figure A.9 Azimuthally integrated GIWAXS data for Nb_2O_5 plotted with fit lines for orthorhombic Nb_2O_5 PDF #27-1003 with I:O loadings of (a) 1.2 (c) 2.4 and (e) 3.0. Original 2D data are inset with color scales correspond to the log of the X-ray intensity.

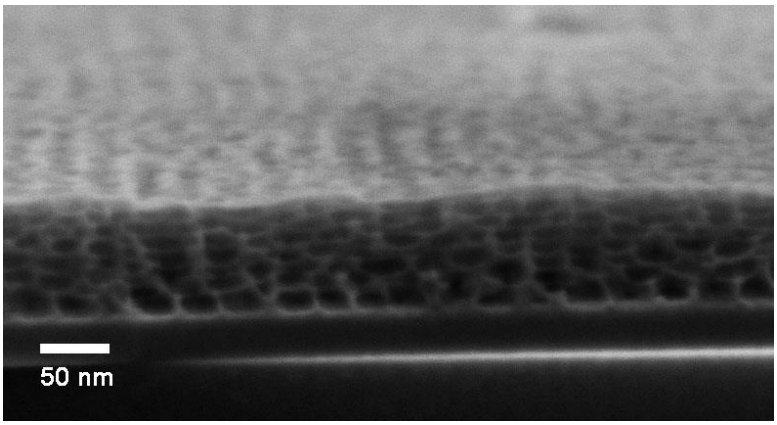

Figure A.10 SEM cross-section of calcined **P3-1.2-Nb_2O_5** film imaged at a 10^0 incident angle.

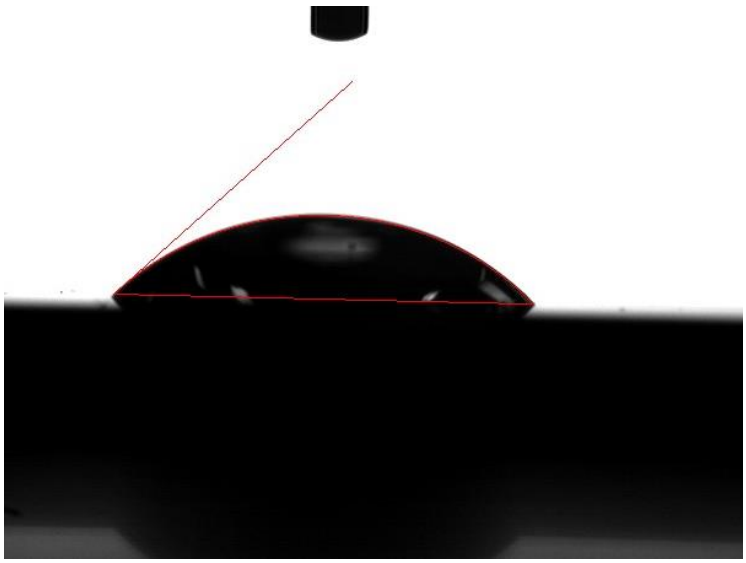

Figure A.11 The contact angle for water was measured on a flat sol-gel derived Nb_2O_5 film after calcination. The average contact angle was determined to be 43°.

APPENDIX B – CHAPTER 3 SUPPORTING INFORMATION

Estimation of Expected Micelle Size

The equilibrium core dimension of a micelle is the result of the free energy contributions of the core and corona blocks as well as their interface. The surface tension at the micelle interfaces drives a reduction of total surface area that favors the formation of larger micelles. This is balanced against the stretching of the core-blocks that causes a loss of conformational entropy. Additional free energy terms include those corresponding to the corona block and the possible presence of any ionic interactions. Various power-type relationships have been derived depending on the particular assumptions and limiting cases considered.[33, 39] In all cases, the equilibrium micelle core radius scales monotonically with N_b, the length of the core chain, and χ, the effective interaction parameter between the core chains and the solvent.

Block copolymers have molar masses ranging from 1 to >1,000 kg/mol and thus form much larger micelles than the few nm ones typical of ~0.2 kg/mol surfactants. In general, all scaling models for block copolymer micelles have the core radius, R_c, scale with the statistical segment length and N_b raised to a power between 0.5 to 0.66:

$$R_c = a\,(N_b)^p$$

Empirically the presence of solvent in the core can expand the power term slightly to e.g. 0.71.[33] The 43.5 kg mol^{-1} poly(hexyl acrylate) used in this study had a degree ofpolymerization of 278. The micelle diameter may be anticipated using the above scaling relationships as limiting cases. A statistical segment length of 0.26 nm was measured for micelles with a poly(butyl methacrylate) core.[33] Using this as an approximation for poly(hexyl acrylate) yields an anticipated micelle core diameter ($D_c=2R_c$) between 8.7 (p=0.5) and 28.3 nm (p=0.71). The longer of the two chain conformation is anticipated based upon the relatively high-χ conditions used in this study.

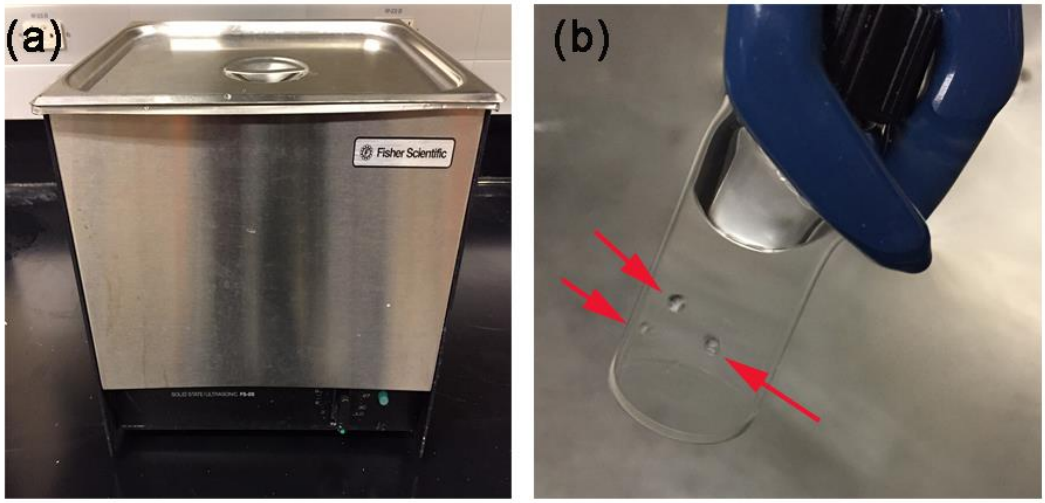

Figure B.1 (a) A photo of the sonicator used in this study and (b) observation of small bubbles continuously formed in the polymer solution during sonication. The bubbles either collapsed or coalesced and then collapsed.

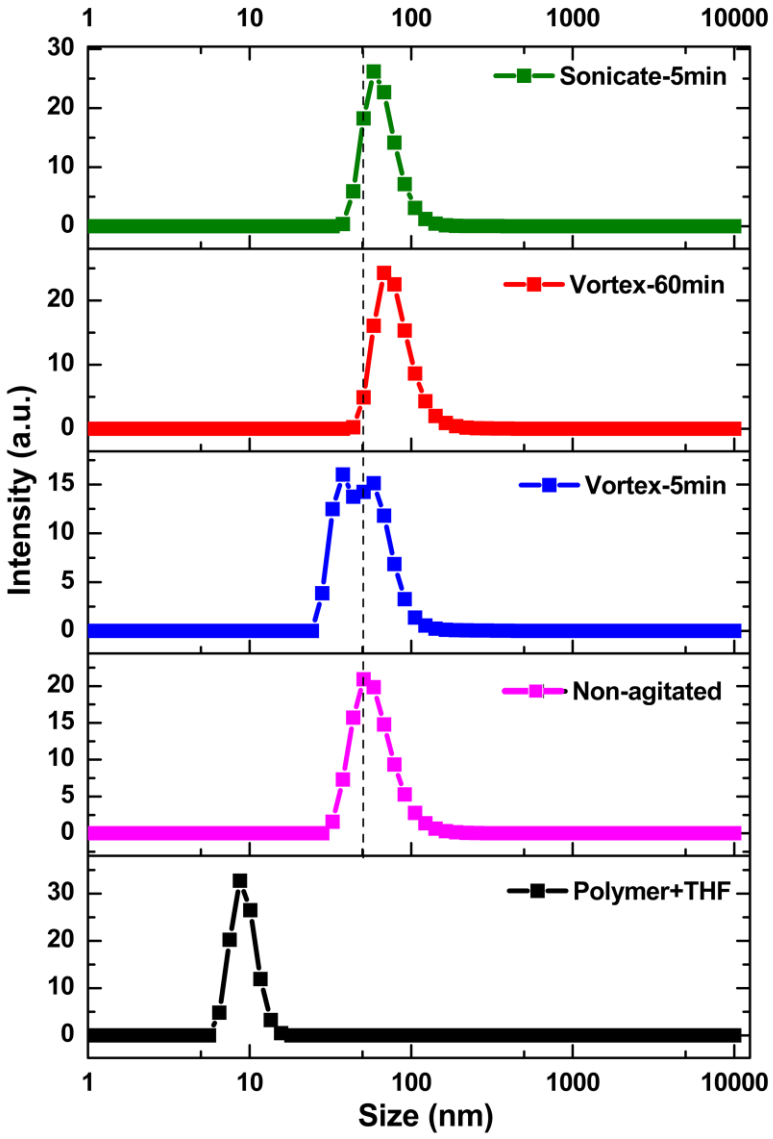

Figure B.2 DLS measurements of polymer solutions from dissolution through micellization and subsequent growth through agitation induced chain exchange. All DLS measurements were made before the addition of inorganic.

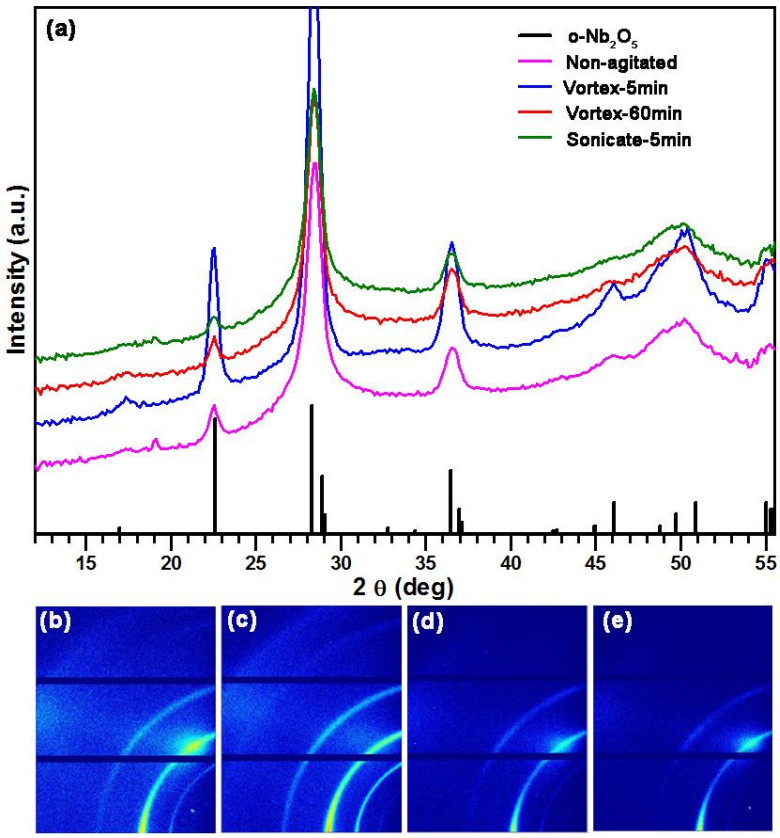

Figure B.3 GIWAXS was measured for all reported samples after calcination (b-e). The 2D patterns were radially integrated (a) and were all consistent with o-Nb_2O_5 (PDF #27-1003). The 2D data correspond to (b) non-agitated, (c) vortex-5min, (d) vortex-60min and (e) sonicate-5min. The 2D color scale corresponds to the log of the X-ray intensity.

The GIWAXS experiments were conducted with an incident angle of 8° to minimize the degree of data smearing. The instrumental broadening factor was measured using NIST reference material 640c. The instrumental broadening factor was taken into account by modeling the observed niobia peak as a Gaussian with a Gaussian point spread function arising from the measured instrumental broadening factor.

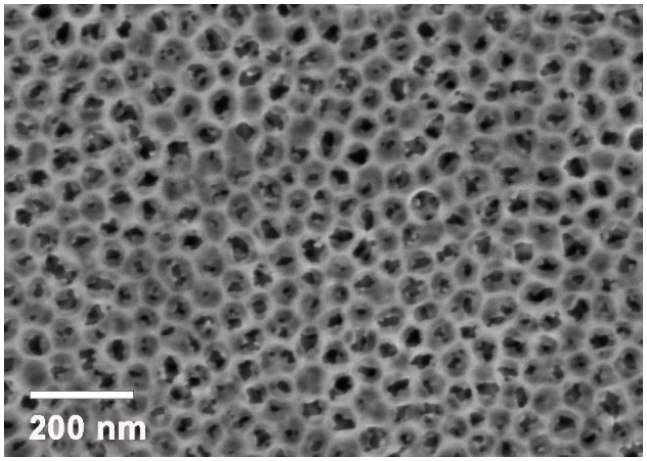

Figure B.4 SEM image of mesoporous WO_3 film prepared with micelle templating. This sample was made using 35 mg of PEO-*b*-PHA (PEO =20 kg mol^{-1} and PHA =58 kg mol^{-1}) dissolved in 2 ml of anhydrous THF and 74 µl of 37%HCl. The solution was vortexed for 5 min at 2000 rpm and transferred into a vial containing 106.5 mg of WCl_6 and stirred for 1 h. The same dipping, aging and calcining procedures described in main text were used here.

Table B.1 Nb_2O_5 grain sizes calculated from the (001) peak o-Nb_2O_5 using the Scherer formula.

Sample Name	Grain Size (nm)
Non-agitated	**12.1**
Vortex-5min	**12.6**
Vortex-60min	**14.8**
Sonicate-5min	**14.6**

APPENDIX C – CHAPTER 4 SUPPORTING INFORMATION

Table C.1 Filmetrics studies of films made on Si wafer to measure the total thickness of each thin film made at different M:T ratio after calcination.

Sample	Spin rate (rpm)	Thickness (nm)			
		Trial 1	Trial 2	Trial 3	Average
M:T-1.2	750	183.1	179.4	180.4	180.97
	1000	177.9	169.8	173.1	173.60
	1500	128.6	122.7	126.3	125.87
	2000	115.3	110.3	106.9	110.83
	3000	92.41	94.67	95.82	94.30
	4000	90.31	82.31	80.48	84.37
M:T-2.4	750	312.3	320.1	316	316.13
	1000	253	259	261	257.67
	1500	228	239	237.8	234.93
	2000	174	172.3	177	174.43
	3000	140	140.6	140.5	140.37
	4000	129.8	128.3	114.5	124.20
M:T-3.0	750	401	416.3	390.2	402.50
	1000	392.2	387.1	386.3	388.53
	1500	301.1	310.2	330.9	314.07
	2000	218.1	229.4	226.5	224.67
	3000	177.6	181.6	193.6	184.27
	4000	167.7	165.3	161.5	164.83

Table C.2 Equations for best fits obtained by fitting the experimentally obtained thickness values for three different M:T ratios.

Sample	Equation for best fit
M:T-1.2	$t = 5113.833w^{-0.5}$
M:T-2.4	$t = 8371.74w^{-0.5}$
M:T-3.0	$t = 11286.63w^{-0.5}$

Table C.3 Average total film thickness values obtained from filmetrics study on calcined films after spun at different spin rates. Spin rates were calculated for each M:T ratio to get total thickness of 180 nm for all the samples. Actual spin values were slightly different since the instrument can spin 50 rpm increments only.

Sample	Average total thickness obtained for calcined films (nm)	Calculated spin rate to achieve 180 nm total thickness (rpm)	Actual spin rate used for film preparation (rpm)
M:T-1.2	203.4±6.7	807	800
M:T-1.8	186.1±2.5	1550	1550
M:T-2.4	195.7±3.7	2163	2150
M:T-3.0	184.7±6.1	3300	3300

Figure C.1 3-electrode setup used for the electrochemical studies. Lithium pieces were used as counter and reference electrodes. Alligator type clips made with Titania were used as electrical contacts to decrease the resistivity that could arise from the contacts.

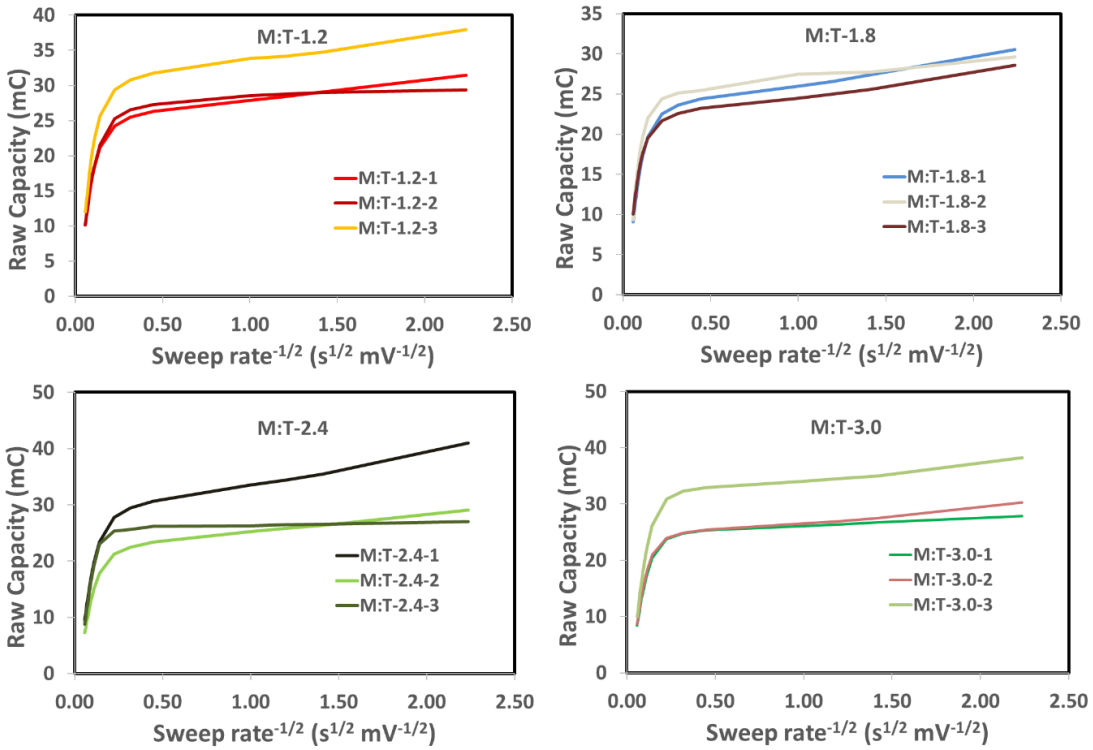

Figure C.2 Capacity versus $v^{-1/2}$ graphs for all the M:T ratios. (a) M:T-1.2 (b) M:T-1.8 (c) M:T-2.4 (d) M:T-3.0. Three trials were conducted in each M:T ratio which resulted scattered raw capacity values.

APPENDIX D – PERMISSION TO REPRINT

Copyright Clearance Center RightsLink®

Home | Create Account | Help

ACS Publications
Most Trusted. Most Cited. Most Read.

Title:	Ordered Mesoporous to Macroporous Oxides with Tunable Isomorphic Architectures: Solution Criteria for Persistent Micelle Templates
Author:	Hasala N. Lokupitiya, Alexis Jones, Barry Reid, et al
Publication:	Chemistry of Materials
Publisher:	American Chemical Society
Date:	Mar 1, 2016

Copyright © 2016, American Chemical Society

LOGIN

If you're a copyright.com user, you can login to RightsLink using your copyright.com credentials. Already a RightsLink user or want to learn more?

PERMISSION/LICENSE IS GRANTED FOR YOUR ORDER AT NO CHARGE

This type of permission/license, instead of the standard Terms & Conditions, is sent to you because no fee is being charged for your order. Please note the following:

- Permission is granted for your request in both print and electronic formats, and translations.
- If figures and/or tables were requested, they may be adapted or used in part.
- Please print this page for your records and send a copy of it to your publisher/graduate school.
- Appropriate credit for the requested material should be given as follows: "Reprinted (adapted) with permission from (COMPLETE REFERENCE CITATION). Copyright (YEAR) American Chemical Society." Insert appropriate information in place of the capitalized words.
- One-time permission is granted only for the use specified in your request. No additional uses are granted (such as derivative works or other editions). For any other uses, please submit a new request.

BACK CLOSE WINDOW

Cavitation-enabled rapid and tunable evolution of high-χN micelles as templates for ordered mesoporous oxides
H. N. Lokupitiya and M. Stefik, *Nanoscale*, 2017, **9**, 1393
DOI: 10.1039/C6NR07313A